



**HAL**  
open science

# Modal Analysis of Structures in Time-Periodic Elastic State

Barend Julius Bentvelsen

► **To cite this version:**

Barend Julius Bentvelsen. Modal Analysis of Structures in Time-Periodic Elastic State. Engineering Sciences [physics]. Sorbonne Universites, UPMC University of Paris 6, 2019. English. NNT: . tel-03461286v1

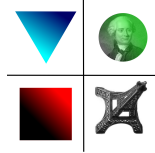
**HAL Id: tel-03461286**

**<https://theses.hal.science/tel-03461286v1>**

Submitted on 30 Jul 2019 (v1), last revised 1 Dec 2021 (v2)

**HAL** is a multi-disciplinary open access archive for the deposit and dissemination of scientific research documents, whether they are published or not. The documents may come from teaching and research institutions in France or abroad, or from public or private research centers.

L'archive ouverte pluridisciplinaire **HAL**, est destinée au dépôt et à la diffusion de documents scientifiques de niveau recherche, publiés ou non, émanant des établissements d'enseignement et de recherche français ou étrangers, des laboratoires publics ou privés.



# MODAL ANALYSIS OF STRUCTURES IN TIME-PERIODIC ELASTIC STATE

Barend Julius Bentvelsen

Thesis defended on 5 October 2018

## Thesis committee

Rapporteur	Fadi DOHNAL	Professor
Rapporteur	Olivier THOMAS	Professor
Examiner	Olivier DOARÉ	Professor
Examiner	Benoît PRABEL	Research Engineer
Examiner	Sebastien NEUKIRCH	Research Director
Thesis director	Corrado MAURINI	Professor
Thesis co-director	Arnaud LAZARUS	Assistant-Professor



# Contents

<b>1</b>	<b>Introduction</b>	<b>3</b>
1.1	Research Field . . . . .	3
1.2	Research goals . . . . .	5
1.3	Reading guide . . . . .	5
<b>2</b>	<b>State of the art</b>	<b>7</b>
2.1	Time-periodic systems . . . . .	7
2.1.1	Relation between nonlinear and time periodic systems . . . . .	8
2.1.2	Time-periodicity in Ordinary Differential Equations . . . . .	9
2.1.3	Time-periodic vibrations in engineering . . . . .	10
2.2	Examples: vibrations of beams in periodic elastic states . . . . .	11
2.2.1	Ziegler column . . . . .	12
2.2.2	Finite element discretization of the cantilever beam with periodic prestress . . . . .	15
2.3	Stability of time-periodic systems . . . . .	17
2.3.1	Floquet theory . . . . .	17
2.3.2	Time domain . . . . .	18
2.3.3	Frequency domain . . . . .	19
2.3.4	Stability types . . . . .	22
2.3.5	Stability analysis of the 2-DoF Ziegler column . . . . .	25
2.4	Classic Modal Analysis . . . . .	27
2.4.1	Modal projection of the cantilever beam with periodic prestress . . . . .	30
2.5	Conclusions . . . . .	34

<b>3</b>	<b>Frequency domain analysis of Floquet forms</b>	<b>37</b>
3.1	Introduction . . . . .	37
3.2	Time-domain method . . . . .	39
3.2.1	STM eigenvectors . . . . .	39
3.3	Hill Matrix . . . . .	41
3.3.1	Complex Hill Matrix Derivation . . . . .	41
3.3.2	Real Hill Matrix Derivation . . . . .	44
3.4	Periodically conservative case ( $\eta = 0$ ) . . . . .	46
3.4.1	Constant elastic state ( $\beta = 0$ ) . . . . .	47
3.4.2	Periodic elastic state ( $\beta \neq 0$ ) . . . . .	48
3.4.3	Asymptotic cases ( $\beta \rightarrow +\infty$ ) and ( $\beta \rightarrow 0$ ) . . . . .	53
3.5	Non-Conservative case ( $\eta = 1$ ) . . . . .	55
3.5.1	Constant elastic state ( $\beta = 0$ ) . . . . .	55
3.5.2	Periodic elastic state ( $\beta \neq 0$ ) . . . . .	56
3.6	Spectral convergence of the stability analysis . . . . .	60
3.7	Discrete dynamical stabilization above buckling load . . . . .	61
3.7.1	Conservative case . . . . .	62
3.7.2	Finding stability zones . . . . .	64
3.7.3	Stability Zone Characteristics . . . . .	65
3.7.4	Nonconservative case . . . . .	68
3.8	Conclusions . . . . .	70
<b>4</b>	<b>Time-periodic modal analysis</b>	<b>73</b>
4.1	Modal-Floquet Transformation . . . . .	74
4.2	Free vibration . . . . .	77

---

4.2.1	Floquet form computation and visualisation . . . . .	77
4.2.2	Projection on Floquet Forms . . . . .	82
4.2.3	Numerical application . . . . .	83
4.3	Forced vibrations of time-periodic systems . . . . .	87
4.3.1	Projecting the force vector . . . . .	87
4.3.2	Example of a harmonic external force . . . . .	88
4.3.3	Frequency Response Spectrum . . . . .	91
4.4	Conclusions . . . . .	92
<b>5</b>	<b>Conclusions</b>	<b>93</b>
	<b>Appendices</b>	<b>95</b>
<b>A</b>	<b>Equation of motion of the Ziegler column</b>	<b>97</b>
<b>B</b>	<b>Hill matrix implementation</b>	<b>99</b>
B.1	Floquet transform . . . . .	99
B.2	Fourier transform . . . . .	100
B.3	Harmonic Balance . . . . .	100
B.4	Hill matrices . . . . .	101
B.5	Numerical implementation . . . . .	103
<b>C</b>	<b>High Frequency Averaging of the statically diverging Ziegler Column in periodic elastic state</b>	<b>107</b>
C.1	Averaged equations of motion . . . . .	108



# Abstract

Time-periodic systems are an important niche in dynamical systems, analysing these systems profoundly opens up new possibilities for engineering. The goal of this thesis is to provide a comprehensive guide on computing Floquet forms and application of modal analysis of structures in time-periodic elastic state. The method is illustrated by fundamental examples.

Modal analysis consists of computing the mode shape and the natural frequency of the equations of motion, this method is limited to linear time-invariant structures. Linear time-periodic systems have attracted attention over the past decades. Floquet theory has been applied to analyse stability. Using the same theory it is possible to compute periodic eigenvectors, known as Floquet forms, which are time-periodically equivalent to modes. Thus allowing the generalisation of modal analysis to linear time-periodic structures.

Floquet forms are computed as eigensolutions of Hill's matrix. The eigenspectrum requires treatment to find linearly independent Floquet forms. By using the archetypical case of a Ziegler column eigenvector sorting is shown to be the most efficient method to sort out Floquet forms.

Projecting the physical equations of motion on Floquet forms results in a system of uncoupled equations with time independent coefficients. Truncating the number of Floquet forms results in a reduced order model. Computing Floquet forms is simplified by first projecting the equations of motion on classic modes. A finite element model of a periodically prestressed beam shows convergence of the solution with increasing number of Floquet forms. Thus proving the concept of time-periodic modal analysis.



# Introduction

---

This work is meant as a comprehensive guide for modal analysis of structures in time-periodic elastic states. The computation and application of time-periodic modes, known as Floquet forms, is analyzed in detail. This gives insight into the efficient computation of Floquet forms. Applying these leads to modal analysis of time-periodic systems, which simplifies calculations and gives deeper insight in dynamic problems.

## 1.1 Research Field

Modal analysis is a key concept in the study of mechanical vibrations that is today commonly used by scientists and engineers in various fields. From molecular chemistry [1], rotating machinery [2] to aerospace industries [3]. It is a spectral numerical method consisting of decomposing the first order perturbation around an equilibrium state of a dynamical system to a linear superposition of harmonic eigenmodes [4]. Those modes allow to reveal intrinsic vibrational properties [5] or the local stability behavior of structures in equilibria [6, 7]. However this is limited to linear time independent (LTI) systems. Modes can also be used as a projection basis to reduce the dimensionality of linear or nonlinear vibrational structural models [8, 9].

When the hypothesis of linear systems is no longer valid, one enters the domain of nonlinear dynamics [10, 11]. Modal analysis for the nonlinear domain has been developed [12, 13]. These nonlinear normal modes are based on the fact that there exist series of periodic solutions that form an invariant manifold for nonlinear dynamical systems around equilibria [14]. The conditions for their existence are no internal resonances and a conservative system [15]. The periodic solutions are of interest to understand stability and gain physical insight in the vibratory response of the system.

There exists an intermediate class of problems between LTI systems and nonlinear ones linear time-periodic problems. In structural dynamics, time-periodic systems include rotating machineries with imperfections [16, 17], examples of this are damaged or geometrically imperfect rotors [18, 19]. Another example of time-periodic problems structures submitted to periodic tensile or compressive axial loading such as slender beams or plates undergoing large vibrations [11].

There are two main kinds of physical problems whose modeling leads to linear time-periodic systems. In the first case, time-periodic systems are periodic solutions of nonlinear problems. By linearizing these solutions, linear time-periodic systems are obtained.

These have been used for numerical continuation of periodic solutions [20, 21, 22] and has been applied in rotor/stator contact problems [23]. In the second case, an otherwise linear problem sees one of its geometric or mechanical properties periodically modulated. For example, a linear pendulum suspended on a high-frequency vibrating base, which makes the pendulum feel its effective gravity modulated. Counter-intuitively, the periodicity can cause the pendulum to stabilize in the upside down position [24, 25, 26]. Whether it is linear or nonlinear, time-periodic systems can be seen as being excited by a system parameter, which is also known as parametric excitation. An example of this is a periodic compression load that is taken into account as a stiffness variation. Parametric excitation leads to the concept of dynamic stability [24, 11, 27], parametric resonance and anti-resonances [28, 29]. These can be used to dampen response [30, 31] or to increase response [32, 33].

Thanks to Floquet theory [34, 35], it should be possible to generalize the linear modal approach to dynamical systems in periodic stationary states, i.e. states whose properties vary periodically with time [24]. Mathematically, a perturbation around a periodic state can be decomposed in a linear superposition of almost periodic eigenfunctions, called Floquet forms (FFs). Like vibrational modes for an equilibrium, Floquet Forms could reveal the intrinsic vibrational properties of a structure in periodic state and determine its local stability. Floquet theory is numerically applied in periodically time-varying linear systems [24] or nonlinear dynamical systems [36, 11] but the spectral computation and physical meaning of Floquet Forms have often been overlooked.

There are two main approaches to Floquet theory: either in time or frequency domain. The first consists of computing the state-transition matrix (STM) to analyze the change of state. This analysis is done by either integrating the system over time and computing Floquet multipliers [37, 38]. It is also possible, once the Floquet multipliers are known, to apply a second time-integration and compute time-periodic eigenvectors [39]. A second technique consists in using the Lyapunov-Floquet transformation to recast a linear time-periodic system in a time-invariant one [40, 41]. This transformation has mostly been used as a step, which coupled with center manifold reduction techniques and normal form theories, enables the study of nonlinear time-periodic systems undergoing bifurcations [42, 43, 44]. Alternatively to Floquet theory, there are perturbative methods to solve periodic problems such as averaging [45, 46], method of multiple scales [47, 48] and normal form theory [15].

Using Floquet theory in the frequency domain is based on computing Hill's matrix [49] and analyzing its spectrum. This should theoretically give direct access to Floquet Forms, but the computational reality is quite different. As upon numerical truncation, the convergence of Hill's matrix is subjected to controversy [50, 51, 52]. In the eigenspectrum are only a few linearly independent eigensolutions which form the basis of Floquet Forms, the spectrum is polluted with many spurious Floquet Forms.

As a consequence, two main approaches have been developed to apply Floquet theory in the frequency domain. The first approach consists in imposing particular fundamental frequencies of Floquet Forms, which are known as Floquet exponents, to maintain self-adjointness of the Hill problem and discard any spurious spectrum. In other words, this method computes parameters of the periodic state associated with a given Floquet mode.

[53, 54, 55]

The second method is modal analysis that seeks Floquet Forms associated with a given state. This could be done by directly computing the truncated spectrum of Hill's matrix for a given periodic state. However the truncated Hill spectrum needs treatment. Which procedure to sort the Floquet Forms has not yet been settled. The two main contenders are sorting methods based on the Hill eigenvalues [56, 57, 58] or eigenvectors [59, 60, 61].

## 1.2 Research goals

The first goal of this thesis is to be a comprehensive guide to computing Floquet forms in the frequency domain, which are used as time-periodic modes. A comparison of time and frequency domain methods are given and advantages and limitations of these methods are shown. By improving the understanding of Floquet Forms and how to compute them, their full potential can be unlocked. So that besides stability analysis, which is well-established, modal analysis of time-periodic systems becomes more accessible.

The second goal of this thesis is to investigate what procedure computes FF efficiently and robustly. For this purpose the sorting of Hill's spectrum is analyzed in depth. Stability analysis of linear time-periodic systems is investigated by comparing several frequency domain methods. The convergence of these methods shows what method is most efficient. Furthermore this closes the debate that the Hill matrix spectrum requires treatment.

The final goal of this thesis is how to use Floquet Forms as periodic modes and what it means to generalize modal analysis from structures in equilibrium to structures in periodic state. Floquet forms are a truly orthogonal basis in time and space for LTP systems. By projecting the equations of motion on these periodic modes, a system of uncoupled LTI equations is obtained. Understanding the derivations and implication of this shows the reader that modal analysis of structures in periodic elastic state is possible and what the challenges are.

## 1.3 Reading guide

The content of this thesis is divided in three chapters which deal with the context, computation and application of time-periodic modes.

Chapter 2 covers the state of the art of structures in periodic elastic state and modal analysis. This chapter starts by introducing the context with respect to nonlinear dynamics. Systems investigated throughout the thesis are introduced. Subsequently, Floquet theory is introduced by analysing stability of time-periodic systems in both the time and frequency domain. Modal analysis of linear time invariant systems is treated as a basis to understand time-periodic modal analysis.

Chapter 3 shows how to compute Floquet forms. This chapter relies on work recently published [59, 62]. Computation of Floquet Forms in the time domain is described. A 2 degree of freedom Ziegler column under periodic compression is used as a benchmark. Floquet form stability in the frequency domain is compared for eigenvalue and eigenvector sorting. The behaviour of Floquet Forms is analyzed for different cases: conservative and non-conservative loads and asymptotic cases. Finally the case of a fundamentally unstable Ziegler column demonstrates the robustness of eigenvector sorting.

In chapter 4 Floquet Forms are applied as an orthogonal basis for the transverse vibrations of a cantilever beam discretized with the finite element method. This beam's stiffness is modulated by a periodic prestress. Classic modes are applied to reduce the finite element problem and keep the Hill matrix handleable. Floquet Forms are substituted in free vibrating equations of motion, which reduces it to a system of uncoupled, time-invariant equations. By applying Floquet Forms in forced equations of motion, the excitation is projected on a Floquet form basis. Both cases are tested for convergence and computation speed.

# State of the art

---

Modal and stability analysis is a well-established tool in structural engineering. It is a method to reveal intricate vibrations in structural dynamics. Modes give vibrational and stability information on the oscillatory patterns of a structure in equilibrium. Furthermore, modal frequencies show when to expect resonance. This in turn can be utilized for assessment or optimization of structures.

An overview of stability analysis of time-periodic systems and classic modal analysis are treated in this chapter. These key concepts are meant as background for readers that are not specialized in time-periodic dynamics. What is introduced are relations between periodic and constant systems, modal and stability analysis.

There have been several methods developed to analyze time-periodic systems for stability. Floquet theory shows these systems have linearly independent almost-periodic solutions, equivalent to modes, called Floquet forms (FFs). However we believe there is a current gap in literature, which consists mostly in a comprehensive guide for computing and using these almost-periodic modes for engineering, namely for helping in the understanding of the oscillations of structures in periodic elastic states.

Starting by specifying the place of time-periodic systems within nonlinear dynamics, classic linear time-invariant system are introduced as a special case of time-periodic systems. Stability of time-periodic systems and Floquet theory is then introduced and Floquet theory is split into time and frequency domain approaches.

## 2.1 Time-periodic systems

In structural dynamics time-periodicity arises from certain processes directly. Rotating machinery with imbalances such as damaged helicopter wings [17] or windturbines with varying atmospheric conditions [63], are a principal domain as a source of interest for time-periodic problems. In maritime engineering, parametric roll is considered as a time-periodic stability problem [64]. Another application is to enhance damping by periodically varying a parameter [30]. Classic textbooks on this subject have been written by Nayfeh [11] and Bolotin [24]. More recently, books have been written by Fidlin [48] and Thomsen [46] on the subject.

### 2.1.1 Relation between nonlinear and time periodic systems

The link between nonlinear, periodic and linear systems is described in this section.

The nonlinear dynamic of structures can usually be described in the  $N$ -dimensional discrete formalism

$$\dot{\mathbf{y}}(t) = \mathbf{f}(t, \mathbf{y}(t)), \quad \mathbf{y}(t) \in \mathfrak{R}^N \quad (2.1)$$

where the state of the system is described by the  $N$ -dimensional vector  $\mathbf{y}(t)$ . The state velocity  $\dot{\mathbf{y}}(t) = d\mathbf{y}(t)/dt$  is a function of time  $t$  and the state of the system itself through the evolution function  $\mathbf{f}$ . By looking at stationary solutions of dynamical systems as in (2.1), predictions can be made about their long-term behaviour. Possible stationary solutions to nonlinear systems include fixed points, limit cycles, limit tori and strange attractors [10]. The current discussion is limited to fixed points and limit cycles. These are referred to as constant and periodic stationary states respectively.

If the solution is a fixed point of a dynamical system, the structure described by this solution is often said to be in a constant equilibrium state. In structural dynamics, linearizing around an equilibrium state leads to the canonical linear equation of motion with mass, damping and stiffness matrices. Mathematically speaking, this linear system is described by linear ordinary differential equations with constant coefficients.

In case of a limit cycle, the structure is said to be in periodic state. Linearizing the system around the limit cycle leads to a time-periodic linear system. The equation of motion now has one or more time-periodic coefficients. These systems are sometimes referred to as parametric systems since the parameter variation can be seen as an excitation of the system [11]. Computing stability and the characteristic response of these systems is a non-trivial task.

Other solutions such as tori and strange attractors, which lead to chaotic behavior [10], are beyond the scope of this work. Limit tori lead to almost-periodic systems, these can be approximated as periodic systems [65] to compute stability.

Almost-periodic functions [66] do not have a closed limit cycle, which would be the case for periodic functions. However the system almost repeats itself within an arbitrarily close distance  $\epsilon$  given sufficient time  $\tau_0$ . So that if we take a continuous function  $g(t)$ , the system almost repeats itself:  $|g(t) - g(t + \tau_0)| < \epsilon$ . In the work of Strogatz [10] this is referred to as a quasi-periodic function.

The state of a system  $\mathbf{y}(t)$  is what determines the change in state  $\dot{\mathbf{y}}(t)$ . If the system is at a fixed point  $\mathbf{y}_0(t) = \mathbf{y}_0$ , then it will stay in that state so that:  $\mathbf{f}(t, \mathbf{y}(t)) = \mathbf{0}$ . For periodic stationary state, the state is periodically repeating. When the limit cycle has a period  $T$ , the periodic equilibrium state and its derivative are periodic:  $\mathbf{y}_0(t) = \mathbf{y}_0(t + T)$ ,  $\dot{\mathbf{y}}_0(t) = \dot{\mathbf{y}}_0(t + T)$ . In state space this results in a closed trajectory [67].

By looking at linearized systems around stationary states, properties of the stationary state such as stability and oscillatory modes can be analyzed. Linearizing a dynamical system around a stationary solution consists in writing out a first order approximation of

the nonlinear system at this stationary state. This reveals the properties of the latter such as stability and the linear vibratory response. Mathematically, this linearization process consists in a first order perturbation of the stationary solution

$$\begin{aligned}\mathbf{y}(t) &= \mathbf{y}_0(t) + \epsilon \mathbf{y}_1(t) + H.O.T. \\ \mathbf{y}(t) &\approx \mathbf{y}_0(t) + \epsilon \mathbf{y}_1(t).\end{aligned}\tag{2.2}$$

by expanding the response into a power series with a sufficiently small parameter  $\epsilon$ . Since the parameter  $\epsilon$  is small, the higher order terms (H.O.T.)  $\epsilon^2, \epsilon^3, \dots, \epsilon^n$  can be neglected. Since we are linearizing at a limit cycle, the zeroth order response  $\mathbf{y}_0(t)$  is the limit cycle itself and is supposed to be known.

Analyzing first order response  $\mathbf{y}_1(t)$  determines stability and shows the vibratory modes around the stationary state. By expanding the nonlinear function (2.1) into a Taylor serie, one obtains

$$\dot{\mathbf{y}}_0(t) + \epsilon \dot{\mathbf{y}}_1(t) = \mathbf{f}(t, \mathbf{y}_0(t)) + \epsilon \frac{\partial \mathbf{f}}{\partial \mathbf{y}}(t, \mathbf{y}_0(t)) \mathbf{y}_1(t).\tag{2.3}$$

Separating the variables with and without  $\epsilon$  gives:  $\dot{\mathbf{y}}_0(t) = \mathbf{f}(t, \mathbf{y}_0(t))$  and  $\epsilon \dot{\mathbf{y}}_1(t) = \epsilon \frac{\partial \mathbf{f}}{\partial \mathbf{y}}(t, \mathbf{y}_0(t)) \mathbf{y}_1(t)$ .

The first order derivative with respect to vector  $\mathbf{y}_0(t)$  is also referred to as the Jacobian matrix:

$$\mathbf{J}(t) = \mathbf{J}(t, \mathbf{y}_0(t)) = \frac{\partial \mathbf{f}}{\partial \mathbf{y}}(t, \mathbf{y}_0(t)).\tag{2.4}$$

By isolating the equation in  $\epsilon$ , we get the first order dynamical equation around the studied stationary state

$$\dot{\mathbf{y}}_1(t) = \mathbf{J}(t) \mathbf{y}_1(t).\tag{2.5}$$

It is from this linear equation that the linear vibratory response around a stationary state,  $\mathbf{y}_0(t)$ , is determined. Equation (2.5) is the linear ordinary differential equation that will be studied throughout the report. The difference compared to (2.4) is that in the rest of this work, the stationary state will be trivial and will not need to be computed in order to only focus on linear systems. A final note on notation, the first order response  $\mathbf{y}_1(t)$  is simplified to  $\mathbf{y}(t)$  throughout this thesis.

### 2.1.2 Time-periodicity in Ordinary Differential Equations

Linear time invariant (LTI) systems can be seen as a special case of linear time periodic (LTP) systems. The difference between LTP and LTI systems is that they have time-periodic and time-invariant coefficients, respectively. They are governed by a set of linear ordinary differential equations (ODEs) that for second order systems are in the form:

$$\mathbf{a}_0(t) \mathbf{x}(t) + \mathbf{a}_1(t) \dot{\mathbf{x}}(t) + \mathbf{a}_2(t) \ddot{\mathbf{x}}(t) = \mathbf{F}(t).\tag{2.6}$$

Note that the dot notation is used for derivatives with respect to  $t$  so that the derivative  $d\mathbf{x}(t)/dt$  is noted as  $\dot{\mathbf{x}}$ . The second derivative  $d^2\mathbf{x}(t)/dt^2$  is represented by double dots  $\ddot{\mathbf{x}}(t)$ . The coefficients  $\mathbf{a}_i(t)$ ,  $i = 0, 1, 2$  depend periodically on time. Periodic coefficients repeat themselves after a certain period by definition. If the period is noted as  $T$ , the periodic coefficient  $\mathbf{a}_i(t)$  verifies  $\mathbf{a}_i(t) = \mathbf{a}_i(t+T)$ , where  $T$  is the period. The link between time periodic and invariant systems is that as the period approaches zero, the coefficients become constant. In other words, if a coefficient is constant, it could be considered as a special class of periodicity with  $T = 0$ .

### 2.1.3 Time-periodic vibrations in engineering

In this section, equations of motion of LTP systems are given in the context of time-periodic vibrations in engineering. The link between physical and state space equations is explained. When analyzing LTP systems based on Floquet theory, state space equations will be used which follows the notation from [21, 37, 39, 62].

When studying the vibrations around a structure in equilibrium state, the governing equations of LTI systems have the canonical form:

$$\mathbf{M}\ddot{\mathbf{x}}(t) + \mathbf{C}\dot{\mathbf{x}}(t) + \mathbf{K}\mathbf{x}(t) = \mathbf{F}(t). \quad (2.7)$$

In the classic set of linear discrete  $N$ -dimensional equation (2.7), the stiffness  $\mathbf{K}$ , damping  $\mathbf{C}$  and mass  $\mathbf{M}$  matrices are constant over time. This case corresponds to equations of motion with constant coefficients. In the following, we will consider no damping in our system so that  $\mathbf{C} = \mathbf{0}$ .

If one wants to study the oscillations around a structure in periodic stationary state, the coefficients of the ODEs (2.7) can vary periodically. Any system parameter, such as mass, damping or stiffness, can be a source of periodicity. In the current work only elasticity is assumed to be periodic, which is the most usual case in engineering.

In structural vibrations, periodic elasticity translates as a periodic stiffness matrix:

$$\mathbf{M}\ddot{\mathbf{x}}(t) + \mathbf{K}(t)\mathbf{x}(t) = \mathbf{F}(t). \quad (2.8)$$

Equation (2.8) can be the result of nonlinear processes or because of an imperfection in rotating machinery for example [59]. Note that limiting our framework to periodic stiffness terms does not mean other sources of periodicities can not be analyzed. Eventual periodicities in damping or mass can always be rewritten in the form of constant mass with periodic stiffness (as in equation (2.8)) by a change of coordinates [11].

In this work, the periodic stiffness matrix consists of a constant part  $\mathbf{K}_0$  and a periodic part  $\mathbf{K}_\sigma(t)$  with period  $T$ :

$$\mathbf{K}(t) = \mathbf{K}_0 + \mathbf{K}_\sigma(t), \quad \mathbf{K}_\sigma(t) = \mathbf{K}_\sigma(t + T). \quad (2.9)$$

Not only this is often the case in of practical problems (any slender structure under periodic compressive or tensile prestress for example) but it can be useful to separate the

constant and periodic terms. This allows to compare the classic response of the system without periodicity to the system including periodicity. One can define the periodicity using the period  $T$  or the frequency  $\beta = 2\pi/T$ .

In structural vibration, it is computationally useful to rewrite equations of motion (2.7) in state space where they become first order differential equations. The state space formalism is adopted for time-periodic systems (2.8), leading to:

$$\begin{bmatrix} \mathbf{0} & \mathbf{I} \\ \mathbf{M} & \mathbf{0} \end{bmatrix} \begin{pmatrix} \dot{\mathbf{z}}(t) \\ \dot{\mathbf{x}}(t) \end{pmatrix} = \begin{bmatrix} \mathbf{I} & \mathbf{0} \\ \mathbf{0} & -\mathbf{K}_\sigma(t) - \mathbf{K}_0 \end{bmatrix} \begin{pmatrix} \mathbf{z}(t) \\ \mathbf{x}(t) \end{pmatrix} + \begin{pmatrix} \mathbf{0} \\ \mathbf{F}(t) \end{pmatrix}. \quad (2.10)$$

In equation (2.10), the state variable  $\mathbf{z}$  is introduced that reads  $\mathbf{z}(t) = \dot{\mathbf{x}}(t)$ .

The state matrices  $\mathbf{A}(t)$  and  $\mathbf{B}$  of sizes  $2N \times 2N$  are introduced along with state vector  $\mathbf{y}(t)$  of size  $2N \times 1$  to simplify the notation

$$\mathbf{A}(t) = \begin{bmatrix} \mathbf{I} & \mathbf{0} \\ \mathbf{0} & -\mathbf{K}_\sigma(t) - \mathbf{K}_0 \end{bmatrix}, \quad \mathbf{B} = \begin{bmatrix} \mathbf{0} & \mathbf{I} \\ \mathbf{M} & \mathbf{0} \end{bmatrix}, \quad \mathbf{y}(t) = \begin{pmatrix} \mathbf{z}(t) \\ \mathbf{x}(t) \end{pmatrix}. \quad (2.11)$$

Furthermore the Jacobian matrix of the system is written as  $\mathbf{J}(t) = \mathbf{B}^{-1}\mathbf{A}(t)$  so that the canonical form of time-periodic dynamical systems can be obtain

$$\dot{\mathbf{y}} = \mathbf{J}(t)\mathbf{y}, \quad \mathbf{J}(t) = \mathbf{J}(t + T). \quad (2.12)$$

This state space formulation with periodic Jacobian of size  $2N \times 2N$  will be used extensively in Floquet theory. It is interesting to note that equation (2.12) is identical to (2.5), but the difference is that the expression of the periodic Jacobian matrix here is trivial, when in (2.5),  $\mathbf{J}(t)$  was depending on the nonlinear stationary state we had to compute.

## 2.2 Examples: vibrations of beams in periodic elastic states

In figure 2.1 the cases analyzed throughout this work is shown. The first system is a finite element model of the linear transverse vibrations of a cantilever beam under periodic prestress (Fig.2.1(a,b)). The second case concerns the oscillatory motion of a straight double pendulum under periodic compression load (Fig.2.1(c)).

The 2-DoF beam is an archetypical example of a time-periodic system. It is modeled as a lumped mass and stiffness system with a periodic compressive load. This load can be either constant in direction throughout deformation ( $\eta = 0$ ), leading to a conservative system. Or in case of  $\eta = 1$  the load follows the direction of the beam  $\theta_2(t)$ , which makes the system nonconservative. This is a fundamental case which serves as a benchmark to present time-periodic analysis techniques, notably in the frequency domain.

For the  $N$  degrees of freedom (DoF) beam the finite element formalism is used. The finite element method (FEM) is a well-established numerical technique used in structural engineering. Its equations of motion are derived from virtual work principles and solved

numerically. This example is used to generalize analysis techniques of time-periodic systems to many DoFs, making them applicable in practical cases. Only the conservative case of a discretized beam is considered.

### 2.2.1 Ziegler column

To illustrate the concept of time-periodic modal analysis, we consider the archetypal example of the planar bi-articulated bar illustrated in Fig. 2.1(c), also known as the Ziegler column. This case is a smaller and therefore computationally simpler case than the  $N$ -DoF problem. However this case still shows a very rich picture of instabilities. It is a simple system yet containing both conservative and non-conservative cases. It is well known in literature and therefore it would be possible to compare our approach to other methods [43, 68, 69]. Another advantage of this system is that it is possible to switch between a conservative and non-conservative problem by simply changing the parameter  $\eta$  from 0 to 1 in Fig. 2.1(c).

The rigid and inextensible bars of length  $2l$  have a mass  $m$ . The two bars are allowed to rotate at points  $O$  and  $B$  thanks to elastic hinges characterized by a rotational stiffness  $k$ . At rest, the bi-articulated structure is lying in the horizontal direction  $(O, x)$ . The structure is moving in the plane  $(O, x, y)$  under the action of a constant end compressive force. This force is either conservative ( $\eta = 0$ , i.e. horizontal force) or non-conservative ( $\eta = 1$ , i.e. following force). The motion of this structure is completely parameterized by the two angles  $\theta_1(t)$  and  $\theta_2(t)$  between the horizontal axis  $(O, x)$  and the first and second bar, respectively. In this work, we are interested in the linear vibrations of this two degrees-of-freedom structure about the trivial straight state  $\theta_1(t) = \theta_2(t) = 0$ . Such a model is qualitatively representative of a tremendous amount of applications in structural

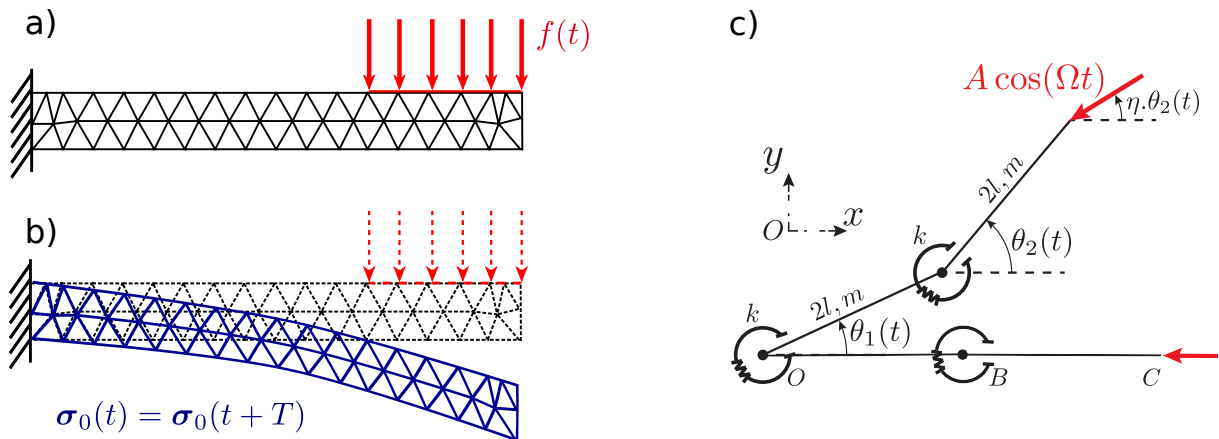


Figure 2.1: Cases investigated are beam-models in periodic elastic states. a) A finite element model of a beam under periodic prestress. Periodically varying stiffness is taken into account as a geometric stress tensor. The geometric stress is directed along the beam's axis and is constant in space so that the geometric stress is:  $\sigma_g = \sigma_{g,xx}(t) = \sigma_{g,xx}(t + T)$ . An external load is applied on the beam  $f(t)$ . b) The actual configuration of the beam at time instant  $t$ . c) A two degrees of freedom Ziegler column with a periodically varying axial compression load  $A \cos(\Omega t)$ . The beam is parametrized by the angles  $\theta_{1,2}$  and has stiffness  $k$ , mass  $m$  and length  $2l$ .

mechanics as it exhibits most of the classic bifurcations of dynamical systems, although the perturbed stationary state is spatially trivial.

Balancing the quantity of acceleration of each bar of the bi-articulated elastic system with the applied external moments (the expression of those quantities are given in Appendix A), the nonlinear equation of motion of the Ziegler column, reads, in the physical space  $(\theta_1(t), \theta_2(t))$

$$\begin{aligned}
 0 &= \frac{16}{3}ml^2\ddot{\theta}_1 + 2ml^2\ddot{\theta}_2 \cos(\theta_1 - \theta_2) + 12ml^2\dot{\theta}_2 \sin(\theta_1 - \theta_2) + 2k\theta_1 - 2k\theta_2 + \\
 &\quad 2lA \cos(\Omega t) [\cos \theta_1 \sin \eta\theta_2 - \sin \theta_1 \cos \eta\theta_2], \\
 0 &= \frac{4}{3}ml^2\ddot{\theta}_2 + 2ml^2\ddot{\theta}_1 \cos(\theta_1 - \theta_2) - 2ml^2\dot{\theta}_1 \sin(\theta_1 - \theta_2) + k\theta_1 - k\theta_2 + \\
 &\quad 2Al \cos(\Omega t) [\sin \theta_1 \cos \eta\theta_2 - \cos \theta_1 \sin \eta\theta_2]. \quad (2.13)
 \end{aligned}$$

By introducing the dimensionless time variable  $\tau = \omega_n t$  with a reference natural frequency  $\omega_n = \sqrt{k/(ml^2)}$  and multiplying the equations Eq.(2.13) by  $3/(16k)$  and  $3/(4k)$ ,

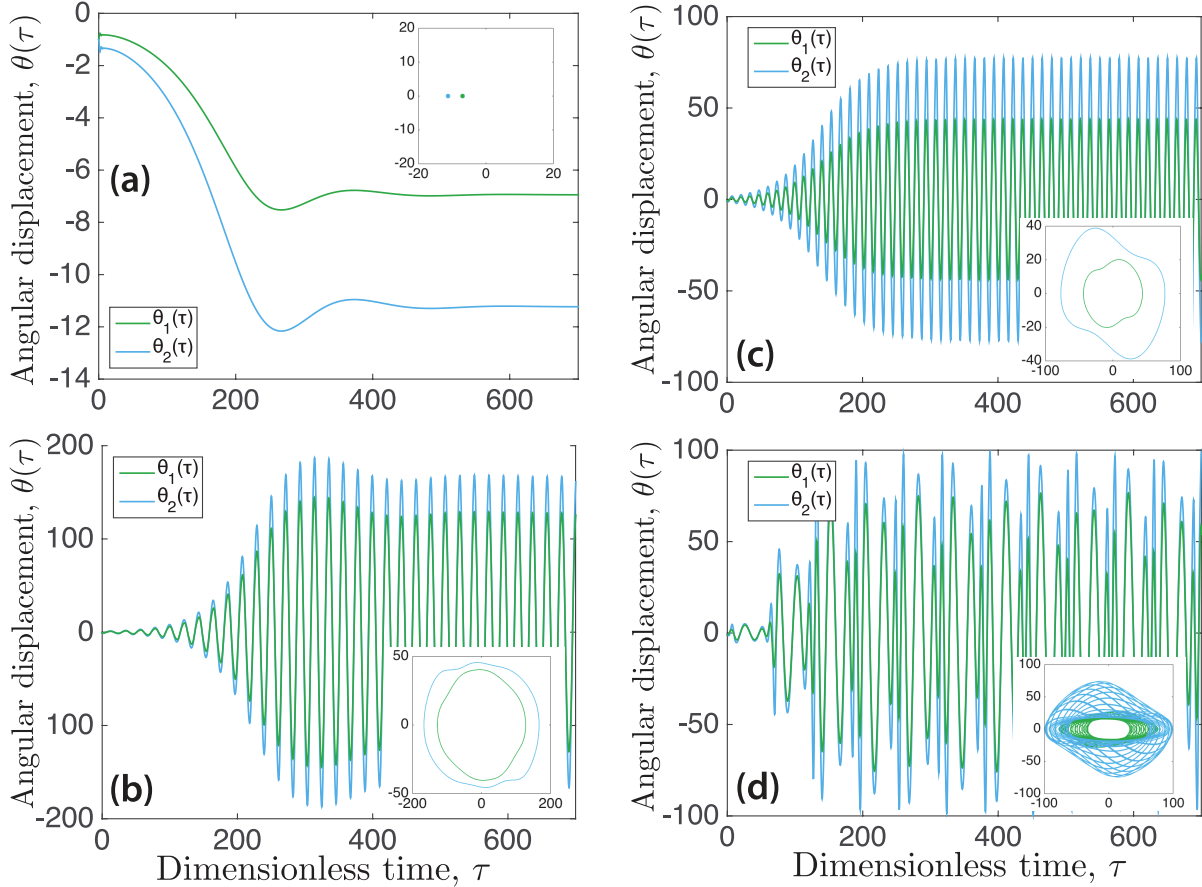


Figure 2.2: Nonlinear dynamical response for various loading parameters and initial conditions  $\theta_1(0) = \theta_2(0) = -1^\circ$  and  $\dot{\theta}_1(0) = \dot{\theta}_2(0) = 0$ . A little amount of viscous damping has been introduced to help the simulations. (a) Bifurcation to an equilibrium state for  $\eta = 0$ ,  $\beta = 0$  and  $\lambda = 0.072$ . (b) Flip bifurcation to a dynamic state with a  $2T$ -period for  $\eta = 0$ ,  $\beta = 0.584$  and  $\lambda = 0.036$ . (c) Hopf bifurcation to a periodic stationary state for  $\eta = 1$ ,  $\beta = 0$  and  $\lambda = 0.4$ . (d) Secondary Hopf or Neimark-Sacker bifurcation on a quasi-periodic state for  $\eta = 1$ ,  $\beta = 0.1$  and  $\lambda = 0.6$ . Insets show the bifurcated stationary states in the state space  $(\theta(\tau), \dot{\theta}(\tau))$ .

respectively, one can rewrite Eq.(2.13) in the dimensionless form

$$\begin{aligned}
0 &= \ddot{\theta}_1 + \frac{3}{8}\ddot{\theta}_2 \cos(\theta_1 - \theta_2) + \frac{3}{8}\dot{\theta}_2^2 \sin(\theta_1 - \theta_2) + \frac{3}{8}\theta_1 - \frac{3}{16}\theta_2 \\
&\quad + \lambda \cos(\beta\tau) [\cos(\theta_1) \sin(\eta\theta_2) - \sin(\theta_1) \cos(\eta\theta_2)], \\
0 &= \ddot{\theta}_2 + \frac{3}{2}\ddot{\theta}_1 \cos(\theta_1 - \theta_2) - \frac{3}{2}\dot{\theta}_1^2 \sin(\theta_1 - \theta_2) + \frac{3}{4}\theta_2 - \frac{3}{4}\theta_1 \\
&\quad + 4\lambda \cos(\beta\tau) [\cos(\theta_2) \sin(\eta\theta_2) - \sin(\theta_2) \cos(\eta\theta_2)].
\end{aligned} \tag{2.14}$$

where  $(\dot{\phantom{x}})$  denotes differentiation with respect to  $\tau$ ,  $\beta = \Omega/\omega_n$  is the ratio between the excitation and the reference natural frequency and  $\lambda = A/(8k/3L)$  represents the dimensionless amplitude of the harmonic compressive load. The dimensionless period of the applied compressive force now reads  $\bar{T} = 2\pi/\beta$ .

Eq.(2.14) is an implicit nonlinear system of Ordinary Differential Equations (ODEs) with periodic coefficients in the form  $\mathbf{f}(\mathbf{x}(t), \dot{\mathbf{x}}(t), t) = \mathbf{0}$ , where the 4-dimensional state vector reads  $\mathbf{x}(t) = \{\theta_1, \theta_2, \dot{\theta}_1, \dot{\theta}_2\}^T$ . By changing the dimensionless loading parameters  $\lambda$  and  $\beta$  in the conservative case  $\eta = 0$  or non-conservative one  $\eta = 1$  and for a given set of initial conditions  $\mathbf{x}(0)$ , this simple system exhibits most of the qualitative vibrational behavior of stationary states of nonlinear dynamical systems as shown in Fig. 2.2.

The non-linear response of the 2-dof beam in fig.2.2 shows what happens when non-linearity effects take effect, after loss of local stability. The stationary response leaves the equilibrium state  $\{\theta_1^0, \theta_2^0\} = \mathbf{0}$  since it is locally unstable. This is due to magnitude and frequency of the force applied. In the conservative case ( $\eta = 0$ ) with constant load buckling occurs, see fig.2.2(a). The system starts at the unstable point  $\boldsymbol{\theta}(0) = \mathbf{0}$ , the response diverges until it stabilizes at a new equilibrium. Therefore in state space the stationary response is described by points.

In case of fig.2.2(b) compression in the beam is periodic ( $\beta \neq 0$ ), and a bifurcation occurs. The stationary response is not constant, but periodic. The period of the response depends on what type of bifurcation has occurred. In this case there is a flip bifurcation. A flip bifurcation is sometimes referred to as a period doubling bifurcation [10]. The response period of the new periodic equilibrium state doubles so that it becomes  $2T$ .

In the case of nonconservative compression ( $\eta = 1$ ), other types of bifurcation occur. With a constant compressive load, the system undergoes a Hopf bifurcation. This results in flutter instability. Response grows while oscillating until it reaches a new dynamic equilibrium, see fig.2.2(c). The response in figures 2.2(b) and 2.2(c) is in both cases periodic. Both have periodic stationary states, although at different frequencies and amplitudes. In state space the steady state for cases (b) and (c) are described by limit cycles.

Including periodicity in the nonconservative case ( $\beta \neq 0, \eta = 1$ ), leads to a stationary response which is not periodic but quasi-periodic. The corresponding bifurcation is of the Neimark-Sacker type [10, 70]. In state space, there is some order to the response but it is neither a point nor a limit cycle as we have seen before.

The nonlinear response, also known as the post-critical behaviour, shows what happens

when the beam is unstable. The type of bifurcation tells what stationary state to expect qualitatively. Linear models, that are studied in this report, can show what type of bifurcation occurs when varying parameters. But those models do not describe nonlinear response quantitatively, the post-critical qualitative behavior is deduced from bifurcations.

### Linearization of Ziegler column

By introducing methods to analyze the stability of time-periodic systems, post-critical behavior can be analyzed qualitatively without the need for nonlinear analysis. For this purpose, the Ziegler column is linearized by taking the nonlinear equations of motion (2.14) and linearizing the response with respect to  $\epsilon$  after setting  $\theta_{1,2}(\tau) = \boldsymbol{\theta}_0(\tau) + \epsilon\boldsymbol{\theta}^*(\tau)$ . An equilibrium is found that corresponds to the trivial state  $\boldsymbol{\theta}_0(\tau) = \mathbf{0}$ . The linear response around the trivial state leads to canonical undamped equations of motion:

$$\mathbf{M}\ddot{\mathbf{x}}(\tau) + \mathbf{K}(\tau)\mathbf{x}(\tau) = \mathbf{0}, \quad (2.15)$$

where the displacement  $\mathbf{x}(\tau) = \{\theta_1^*(\tau), \theta_2^*(\tau)\}^T$  and the values for mass  $\mathbf{M}$  and stiffness  $\mathbf{K}$  matrices read:

$$\mathbf{M} = \begin{bmatrix} 1 & \frac{3}{8} \\ \frac{3}{2} & 1 \end{bmatrix}, \quad \mathbf{K}(\tau) = \begin{bmatrix} \frac{3}{8} & \frac{3}{16} \\ -\frac{3}{4} & \frac{3}{4} \end{bmatrix} + \lambda \cos(\beta\tau) \begin{bmatrix} -1 & \eta \\ 0 & 4\eta - 4 \end{bmatrix}. \quad (2.16)$$

where the dimensionless frequency  $\beta$  and load  $\lambda$  come from (2.14). The stability and response of the Ziegler column depend on the modulation parameters  $\beta$  and  $\lambda$ .

An LTP system has been derived from the linearization around the trivial straight state of Ziegler column in periodic compression and traction. This system provides a benchmark to test time-periodic analysis methods.

### 2.2.2 Finite element discretization of the cantilever beam with periodic prestress

The periodically prestressed beam of Fig.2.1(a,b) is modeled using finite elements. FEM is a general method to solve differential equations and is used to model problems from structural and fluid mechanics, heat transfer, and electromagnetism, among others. Applying the analysis of time-periodic structures in the framework of FEM allows its application in many fields. The goal of this section is to show, while using FEM, how to arrive at the canonical equation  $\mathbf{M}\ddot{\mathbf{x}}(t) + \mathbf{K}(t)\mathbf{x}(t) = \mathbf{F}(t)$ . Only the case of a conservative system is considered.

The beam considered is modeled in 2D as a cantilever beam under periodic prestress. The periodic prestress is directed along the axial direction and is of magnitude  $\sigma_0(t)$ . We will show that the periodic axial prestress induces a periodic geometric stiffness matrix:  $\mathbf{K}_g(t) = \mathbf{K}_g \cos \beta t = \lambda \mathbf{K}_c \cos \beta t$  where the parameters  $\lambda$  and  $\beta$  are the amplitude and frequency modulation, respectively and where  $\mathbf{K}_c$  is the critical compressive stress matrix that induced the first buckling mode of the cantilever beam.

The investigated beam is modeled as a steel beam occupying in its reference configuration the domain  $\Omega$  of length 1 m and height 0.1 m. We set the mass density  $7800 \text{ kg/m}^3$ , the Young's modulus  $E = 2.1 \text{ GPa}$ , and the Poisson's ratio  $\nu = 0.3$ . The beam is clamped on the left hand side and is prestressed axially with a value  $\sigma_0(t) = P_x(t)/S$ , where  $S$  is the cross-sectional area and  $P_x(t)$  is an end axial periodic load. The current configuration of the beam at time  $t$  is described by the field  $u(t) : x \in \Omega \rightarrow u(t)(x) \in \mathcal{R}^3$ . The linearized deformation  $\epsilon(u)$  and stress  $\sigma(u)$  tensors are

$$\epsilon(u) = \frac{1}{2} (\nabla u + \nabla^T u), \quad \sigma(u) = \bar{\lambda} \text{tr}(\epsilon(u)) I + 2\bar{\mu} \epsilon(u), \quad (2.17)$$

where  $\bar{\lambda}$  and  $\bar{\mu}$  are the Lamé constants that in plane strain read as  $\bar{\lambda} = \frac{E\nu}{(1+\nu)(1-2\nu)}$  and  $\bar{\mu} = \frac{E}{2(1+\nu)}$ , and  $I$  is the identity tensor.

The finite element method is based on the weak formulation of the equations of motion of the system. After discretizing the domain  $\Omega$  in a set of elements, the field  $u(t)$  is approximated as a linear combination of  $n$  basis functions having a compact support on a patch of element. The coefficients of this linear combinations becomes the news unknowns of the discretized problem. It can be shown that the weak formulation of the linearized equation of motion around the straight prestressed configuration for our prestressed beam is as follows: Find at smooth function  $u(t)$  respecting the kinematic boundary conditions such that

$$a_m(\ddot{u}(t), v) + a_k(u(t), v) + a_g(u(t), v) = 0, \quad (2.18)$$

for each admissible test function  $v$  and each time  $t$ , where

$$\begin{aligned} a_m(u, v) &= \int_{\Omega} \rho u \cdot v d\mathbf{x}_0, \\ a_k(u, v) &= \int_{\Omega} \sigma(u) \cdot \epsilon(v) d\mathbf{x}_0, \\ a_g(u, v) &= \sigma_0(t) \int_{\Omega} \frac{\partial u}{\partial x} \frac{\partial v}{\partial x} d\mathbf{x}_0. \end{aligned} \quad (2.19)$$

are bilinear forms associated to the mass, the material stiffness, and the geometric stiffness, respectively.

Substituting into (2.19) the discrete finite element approximation of the solution in the form

$$\mathbf{u}(t)(x) = \sum_{j=1}^N U_j(t) \phi_j(x), \quad (2.20)$$

where  $\phi_j(x)$  are the finite element basis function, one gets the discretized system

$$\mathbf{M} \ddot{\mathbf{u}}(t) + (\mathbf{K}_0 + \mathbf{K}_g(t)) \mathbf{u}(t) = \mathbf{0}, \quad (2.21)$$

where

$$\mathbf{M}_{ij} = a_m(\phi_i, \phi_j), \quad \mathbf{K}_0^{ij} = a_k(\phi_i, \phi_j), \quad \mathbf{K}_g^{ij} = a_g(\phi_i, \phi_j), \quad (2.22)$$

are the mass matrix, the material stiffness matrix, and the geometric stiffness matrix, respectively.

Introducing the parameter  $\lambda$  as a fraction of the critical compressive load and the frequency  $\beta$  as the system frequency, this leads to:  $\sigma_0(t) = \lambda\sigma_c \cos \beta t$  where  $\sigma_c$  is the critical buckling stress in the beam. The geometric stiffness matrix can then be reformulated as:  $\mathbf{K}_g(t) = \lambda\mathbf{K}_c \cos \beta t$ . The advantage of this formulation is that the modulation parameters becomes explicit in the expression of the geometric stiffness matrix.

In this work use is made of the FEM-software FEniCS [71]. This is an open-source software having a python interface that allows for an easy and efficient implementation of the finite element method, including the assembling of the finite element matrix defined above.

## 2.3 Stability of time-periodic systems

To illustrate stability analysis, the case of a 2-DoF pendulum 2.2.1 is analyzed. Both the periodic and constant compressive prestress cases are investigated. These cases show the difference between time-periodic stability and what happens when the coefficients become constant. One difference between linear ODEs with periodic and constant coefficient is the types of instabilities that can occur [10].

### 2.3.1 Floquet theory

The goal of this section is to explain what Floquet solutions are and how we can analyze the stability of time-periodic systems. Floquet theory is based on work by its name-giver, Gaston Floquet, on differential equations [34]. In this work he has proven that the solutions of differential equations with periodically varying coefficients can be decomposed in almost-periodic solutions. To compute these solutions, we can distinguish two approaches in Floquet theory.

The first approach is made in the time domain method. It computes the periodic solutions by integrating the equations of motion over time. The modulation parameters are taken into account by direct time integration. The second approach transforms coefficients and almost-periodic solutions into the frequency domain. In the frequency domain the so-called Hill matrix is constructed. From the eigenspectrum of the Hill matrix the periodic almost-periodic solutions are computed, as will be shown in more detail in chapter 3.

Floquet has shown that time-periodic differential equations in the form  $\dot{\mathbf{y}}(t) = \mathbf{J}(t)\mathbf{y}(t)$  where  $\mathbf{J}(t)$  is  $T$ -periodic have solutions in the form:

$$\mathbf{y}(t) = \sum_{n=1}^N \mathbf{p}_n(t)e^{s_n t}, \quad \mathbf{p}_n(t) = \mathbf{p}_n(t + T), \quad (2.23)$$

where the component of the solution  $\mathbf{p}_n(t)$  is a time-periodic vector function in state space. The state vector  $\mathbf{y}(t)$  is of size  $N$  so that  $\mathbf{y}(t) \in R^N$ . The time-periodic vector is of the same size so that  $\mathbf{p}(t) \in R^N$ .

Equation (2.23) is very similar to a classic decomposition on classic harmonic eigenmodes when considering ODEs with constant coefficients where the  $\mathbf{p}_n(t)$  would then be constant in time.

An even more general formulation of eqn.(2.23), is to use the more general Floquet amplitude  $q_n(t)$ . This results in a Floquet transform  $\mathbf{y}(t) = \sum_{n=1}^N \mathbf{p}_n(t)q_n(t)$ . The amplitudes  $q_n(t)$  are used in chapter 4 when the system undergoes forcing so that  $\dot{\mathbf{y}}(t) = \mathbf{J}(t)\mathbf{y}(t) + \mathbf{F}(t)$ .

This section focuses on computing Floquet exponents  $s_n$  and multipliers  $\rho_n = e^{s_n T}$  that are used for stability analysis. Computation of functions  $\mathbf{p}_n(t)$  will be discussed in detail in chapter 3. Applying these functions for modal analysis is explained in chapter 4.

### 2.3.2 Time domain

The time domain approach to time-periodic ODEs consists in integrating the system over a period. Computing Floquet solutions in the time-domain has been well established for stability analysis and requires a non-trivial time-integration [37, 39].

#### State Transition Matrix

An important concept for Floquet theory in the time domain is the State Transition Matrix (STM),  $\Phi(t, t_0)$ , which is defined as the change of state over time:

$$\mathbf{y}(t) = \Phi(t, t_0)\mathbf{y}(t_0). \quad (2.24)$$

The STM itself is defined as a matrix from a specific initial time  $t_0$  to time  $t$  where one can set the initial time to zero,  $t_0 = 0$ .

The derivative of the STM,

$$\dot{\Phi}(t, 0) = \mathbf{J}(t)\Phi(t, 0), \quad (2.25)$$

is found by substituting (2.24) into the time-periodic linear equation of motion (2.12),  $\dot{\mathbf{y}}(\tau) = \mathbf{J}(\tau)\mathbf{y}(\tau)$ . The STM derivative is important in order to integrate the STM over time.

It is easy to see that the initial value of the STM is the unit matrix

$$\Phi(0, 0) = \mathbf{I}, \quad (2.26)$$

since when considering the STM of (2.24) at time  $t = t_0$ , the STM has to map the initial condition  $\mathbf{y}(0)$  to itself.

It is important to note that the STM itself is not periodic but there are periodic properties that can be extracted from the STM. One of this property is to look at the STM after one period  $T$  and analyze the so-called Monodromy matrix.

## Monodromy matrix

The STM over one period is known as the monodromy matrix

$$\Phi(T, 0) = \mathbb{M}. \quad (2.27)$$

From this matrix, the stability of a time-periodic system can be computed.

Since the monodromy matrix is defined as the STM over one period, the STM after more than one period can be defined as

$$\Phi(t + T, 0) = \mathbb{M}\Phi(t, 0). \quad (2.28)$$

The relation between the STM and monodromy matrix over multiple periods is defined by

$$\Phi(t + nT, 0) = \mathbb{M}^n \Phi(t, 0). \quad (2.29)$$

This relation shows that computing the monodromy matrix gives insight into the long-term behavior of the system. To get more insights in the properties on the long term, it is possible to decompose the matrix  $\mathbb{M}^n$  in the form

$$\mathbb{M}^n = \mathbf{Q}^{-1} \mathbf{B}^n \mathbf{Q}. \quad (2.30)$$

where  $\mathbf{Q}$  is the matrix that gathers the eigenvectors of  $\mathbb{M}^n$  and  $\mathbf{B}^n$  is a diagonal matrix whose entries are  $\rho_i^n$  where  $\rho_i$ , the eigenvalues of the monodromy matrix  $\mathbb{M}$ , are called the Floquet multipliers.

### 2.3.3 Frequency domain

Stability of linear time-periodic systems can also be computed in the frequency domain. An advantage of the frequency domain is that no time integration is needed. However, as we will see later, there will be a larger eigenproblem to be solved. Another advantage of the frequency domain method is that spectral informations or the frequency content of the vibratory response  $\mathbf{y}(T)$  is directly obtained. The method itself is based on transforming the periodic equations of motion into the frequency domain, i.e. by expanding periodic functions in Fourier series and applying the harmonic balance method. This eliminates the time dependencies of coefficients in the equation.

#### Floquet-Fourier-Hill transform

According to Floquet theory expressed in equation (2.23), the oscillatory motion  $\mathbf{y}(t)$  can be decomposed in the sum of  $N$  independent fundamental solutions  $\mathbf{y}_n(t)$

$$\mathbf{y}(t) = \sum_{n=1}^N c_n \mathbf{y}_n(t), \quad (2.31)$$

where  $c_n$  are constant coefficients and the particular form  $\mathbf{y}_n(t) = \mathbf{p}_n(t)e^{s_n t}$  is known as a Floquet form (FF). The subscript  $n$  denotes the  $n^{\text{th}}$  FF. We recall the Jacobian matrix  $\mathbf{J}(t)$  of the  $N$ -DoF system under study  $\dot{\mathbf{y}}(t) = \mathbf{J}(t)\mathbf{y}(t)$  is periodic with period  $T$  or fundamental frequency  $\beta = 2\pi/T$ . Therefore each fundamental solution  $\mathbf{y}_n(t)$  has a  $T$ -periodic vector function  $\mathbf{p}_n(t)$  with size  $N$ :  $\mathbf{p}_n(t) = \mathbf{p}_n(t + T)$  and an amplitude  $q_n(t) = e^{s_n t}$ .

Using  $m$  FFs, the total response of the system can be written in matrix form  $\mathbf{y}(t) = \mathbf{p}(t)\mathbf{q}(t)$  where  $\mathbf{p}(t) = \{\mathbf{p}_1(t), \dots, \mathbf{p}_m(t)\}$  is an  $N \times m$ -matrix with periodically repeating eigenfunctions in columns and the amplitudes are gathered as an  $m \times 1$  vector  $\mathbf{q}(t) = \{q_1(t), \dots, q_m(t)\}^T$ .

Only one FF is considered for deriving the following Floquet-Fourier-Hill transformation. The basic idea is to expand the periodic vector function  $\mathbf{p}_n(t)$  in the Fourier series

$$\mathbf{p}_n(t) = \sum_{h=-\infty}^{\infty} \mathbf{p}_n^h e^{ih\beta t}. \quad (2.32)$$

Since the amplitude  $q_n(t)$  is an exponential function  $e^{s_n t}$ , the total response for one FF is written as

$$\mathbf{y}_n(t) = \sum_{h=-\infty}^{\infty} \mathbf{p}_n^h e^{(s_n + ih\beta)t}. \quad (2.33)$$

The periodic Jacobian is also transformed into the frequency domain

$$\mathbf{J}(t) = \sum_{j=-\infty}^{\infty} \mathbf{J}^j e^{ij\beta t}. \quad (2.34)$$

Note that none of the coefficients  $\mathbf{J}^j$ , or  $\mathbf{p}_n^h$  are time dependent. Now that we have all the periodic quantities in the frequency domain, the decomposed equation of motion can be written. By replacing equations (2.32), (2.33) and (2.34) in the equation of motion  $\dot{\mathbf{y}}(t) = \mathbf{J}(t)\mathbf{y}(t)$ , one obtains

$$\sum_{h=-\infty}^{\infty} (s_n + ih\beta)\mathbf{p}_n^h e^{(s_n + ih\beta)t} = \sum_{h=-\infty}^{\infty} \sum_{j=-\infty}^{\infty} \mathbf{J}^j \mathbf{p}_n^h e^{(s_n + i(h+j)\beta)t}. \quad (2.35)$$

The problem with (2.35) is that the exponentials on the left and right hand side have different power values. This is due to the variable  $j$ , which can be eliminated by using a frequency shift of  $h \rightarrow h - j$ . This means that all values of  $h$  are shifted to the new value  $h - j$ .

$$\sum_{h=-\infty}^{\infty} (s_n + ih\beta)\mathbf{p}_n^h e^{(s_n + ih\beta)t} = \sum_{h=-\infty}^{\infty} \sum_{j=-\infty}^{\infty} \mathbf{J}^j \mathbf{p}_n^{h-j} e^{(s_n + ih\beta)t} \quad (2.36)$$

Now that the power of the exponentials are equal on the left and right hand side, the equation can be rewritten

$$\sum_{h=-\infty}^{\infty} \sum_{j=-\infty}^{\infty} [\mathbf{J}^j \mathbf{p}_n^{h-j} - (s_n + ih\beta)\mathbf{p}_n^h] e^{(s_n + ih\beta)t} = \mathbf{0}. \quad (2.37)$$

In this equation, the vectors  $\mathbf{p}_n^h$  and matrix-vector products  $\mathbf{J}^j \mathbf{p}_n^{h-j}$  are grouped per harmonic ( $s_n + ih\beta$ ). The relation with the original time-periodic equation  $\mathbf{J}(t)\mathbf{y}(t) - \dot{\mathbf{y}}(t) = \mathbf{0}$  is that now equation (2.37) can be easily recast in a time-independent system of algebraic equations. Indeed, in order for equation (2.37) to be true for each time  $t$ , it needs to be true for each harmonic ( $s_n + ih\beta$ ). This is called the harmonic balance method which consists in equating each harmonic of (2.37) to zero:

harmonic number	exponential	balance equation
$h = -2$	$e^{(s_n - 2i\beta)t}$	$\sum_{j=-\infty}^{\infty} [\mathbf{J}^j \mathbf{p}_n^{-2-j}] - (s_n - 2i\beta)\mathbf{p}_n^{-2} = \mathbf{0},$
$h = -1$	$e^{(s_n - i\beta)t}$	$\sum_{j=-\infty}^{\infty} [\mathbf{J}^j \mathbf{p}_n^{-1-j}] - (s_n - i\beta)\mathbf{p}_n^{-1} = \mathbf{0},$
$h = 0$	$e^{s_n t}$	$\sum_{j=-\infty}^{\infty} [\mathbf{J}^j \mathbf{p}_n^{-j}] - s_n \mathbf{p}_n^0 = \mathbf{0},$
$h = 1$	$e^{(s_n + i\beta)t}$	$\sum_{j=-\infty}^{\infty} [\mathbf{J}^j \mathbf{p}_n^{1-j}] - (s_n + i\beta)\mathbf{p}_n^1 = \mathbf{0},$
$h = 2$	$e^{(s_n + 2i\beta)t}$	$\sum_{j=-\infty}^{\infty} [\mathbf{J}^j \mathbf{p}_n^{2-j}] - (s_n + 2i\beta)\mathbf{p}_n^2 = \mathbf{0}. \quad (2.38)$

The next step consists in reformulate the algebraic equations (2.38) into matrix form in order to compute the Floquet exponents  $s_n$  to determine the stability of time-periodic system.

### Infinite Hill matrix

The harmonically balanced equations 2.37 can be rewritten in matrix form, which leads to an eigenproblem

$$(\mathbb{H} - s_n \mathbf{I}) \phi_n = \mathbf{0}. \quad (2.39)$$

This new formulation contains three important components: the so called Hill matrix  $\mathbb{H}$ , the Floquet exponents  $s_n$  and their corresponding eigenvector  $\phi_n$ . The obtained Hill matrix is an infinite dimensional Toeplitz matrix [72] in the form

$$\mathbb{H} = \begin{bmatrix} \ddots & \vdots & \vdots & \vdots & \ddots \\ \cdots & \mathbf{J}^0 + i\beta \mathbf{I} & \mathbf{J}^{-1} & \mathbf{J}^{-2} & \cdots \\ \cdots & \mathbf{J}^1 & \mathbf{J}^0 & \mathbf{J}^{-1} & \cdots \\ \cdots & \mathbf{J}^2 & \mathbf{J}^1 & \mathbf{J}^0 - i\beta \mathbf{I} & \cdots \\ \ddots & \vdots & \vdots & \vdots & \ddots \end{bmatrix}, \quad (2.40)$$

where each block row in the Hill matrix represents a harmonic  $h$ . In equation (2.39), the eigenvector of Hill's matrix  $\phi_n$  is defined by

$$\phi_n^j = [\mathbf{p}_n^{-\infty-j}, \dots, \mathbf{p}_n^{-1-j}, \mathbf{p}_n^{0-j}, \mathbf{p}_n^{-1-j}, \dots, \mathbf{p}_n^{\infty-j}]^T. \quad (2.41)$$

This is a block vector that consists of Floquet eigenfunction components  $\mathbf{p}_n^{h-j}$ . The corresponding eigenvalues  $s_n^j$  are defined by

$$s_n^j = s_n + ij\beta. \quad (2.42)$$

Note that both the eigenvector and eigenvalue depend on harmonic  $j$  that reads  $j = -\infty, \dots, \infty$ .

### Finite Hill spectrum

Up until now the Hill matrix was infinite, however for evident numerical reasons we need to truncate the matrix. This means that the number of harmonics taken into account is limited for practical purposes. The harmonics are truncated so that  $j, h = -H, \dots, H$ . This truncation raises a new question: whether the eigenvalues of the truncated Hill matrix converge to the same values as the original infinite matrix? The answer to this has been studied in literature [50, 73]. Although the eigenvalues converge, there will always remain an error near the edges of the eigenspectrum. In other words the largest truncation error is when the harmonic  $j$  approaches truncation  $H$ .

One effective method that has been used in literature is the sorting of Floquet exponents based on their imaginary values. For the converged part of the Hill spectrum, we can express the Floquet exponents as  $s_n^k = s_n + ik\beta$  for  $n = 1 \dots N$  and  $-H \leq k \leq +H$ . Since we want to obtain only  $N$  linearly independent Floquet exponents to assess linear stability of the studied periodic stationary state, this method only takes into account the  $N$  eigenvalues that are in a certain domain:  $-\beta/2 < \Im(s_n) \leq \beta/2$  [58]. This domain is referred to as the spectral primitive cell (this name is derived from the primitive cell of spatially periodic structures [74]). By taking the  $N$  eigenvalues whose imaginary parts are contained in the spectral primitive cell  $-\beta/2 \leq \Im(s_l) < \beta/2$ , the latter will eventually converge to Floquet exponents as  $H$  is increased. The convergence of the sorted eigenvalues has been rigorously proved [57, 58].

In chapter 3, we will show in detail that one has to be very careful when sorting the spectrum of the finite Hill matrix and notably that sorting strategies to clean up this spectrum are needed.

### 2.3.4 Stability types

There are two ways to look at stability of a periodic system: Floquet exponents or multipliers. Both methods are based on Floquet theory, but are computed using time and frequency-domain methods respectively. The growth rate shows whether the system is stable or not. In case of an instability, Floquet multipliers or exponents can tell what type of local bifurcation takes place. Since we are studying linear stability concepts, the perturbation will grow exponentially until infinity but in reality, nonlinearities take effect that would limit the response.

The reader should pay attention to the fact that the stability computations are done in state space. This means that the number of eigensolutions is double that of the number of physical modes. This means also that each Floquet exponent has a complex conjugate.

### Floquet multipliers

As shown in section 2.3.2, Floquet multipliers are the eigenvalues of the monodromy matrix  $\mathbb{M}$  and are the amplification factor of the time-periodic system's fundamental modes between each period. The limit after an infinite number of periods is expressed using the  $i^{\text{th}}$  complex Floquet multiplier  $\rho_i$  and monodromy eigenvector  $\mathbf{Q}_i$ :

$$\lim_{n \rightarrow \infty} \mathbf{y}(nT)_i = \lim_{n \rightarrow \infty} \mathbf{Q}_i^{-1} \rho_i^n \mathbf{Q}_i. \quad (2.43)$$

From this equation conclusions can be drawn about the stability based on the magnitude of the Floquet multiplier  $\rho_i$ . This is useful if one wants to know how the system's response will qualitatively behave over the long term. There are three cases possible when looking at Floquet multipliers of periodic systems:

- $|\rho_i| > 1$ : The system is unstable in case the norm of a Floquet multiplier  $\rho_n$  is bigger than unity. This corresponds to an unstable periodic stationary state  $\mathbf{y}_0(t)$ , whereby the solution grows exponentially.
- $|\rho_i| = 1$ : A Floquet multiplier of one implies an undamped, neutrally stable stationary solution. This neutral periodic state means the perturbation  $\mathbf{y}(t)$  neither grows nor diminishes over time.
- $|\rho_i| < 1$ : The stationary state  $\mathbf{y}_0(t)$  is stable and the perturbation  $\mathbf{y}(t)$  diminishes over time.

Moreover, the qualitative behavior in case of instability can be determined by the complex value of the Floquet multipliers.

In figure 2.3, four different cases are identified when the Floquet multiplier norm is superior or equal to one ( $|\rho_i| \geq 1$ ). Depending on the phase or how the Floquet multipliers cross the unit circle, different types of instabilities can occur. In fig.2.3(a) the neutrally stable case is presented with  $|\rho| = 1$ . A Floquet multiplier  $\rho$  and its complex conjugate  $\bar{\rho}$  are shown. This complex conjugate is due to the state space definition of the governing equations.

Figure 2.3(b) shows a steady state bifurcation at  $\rho = \bar{\rho} = 1$ . This type of bifurcation leads to an exponential growth of the perturbed response with period  $T$ . The state of the  $i^{\text{th}}$  Floquet form is given as  $\mathbf{y}_i(t+T) = |\rho_i| \mathbf{y}_i(t)$ . This is referred to as a  $T$ -instability. In nonlinear analysis a new stationary state with a period  $T$  would be found.

Figure 2.3(c) shows a flip bifurcation at  $\rho = \bar{\rho} = -1$ . Similar to the nonlinear response as illustrated in Fig.2.2(b). This type of bifurcation leads to an exponential growth

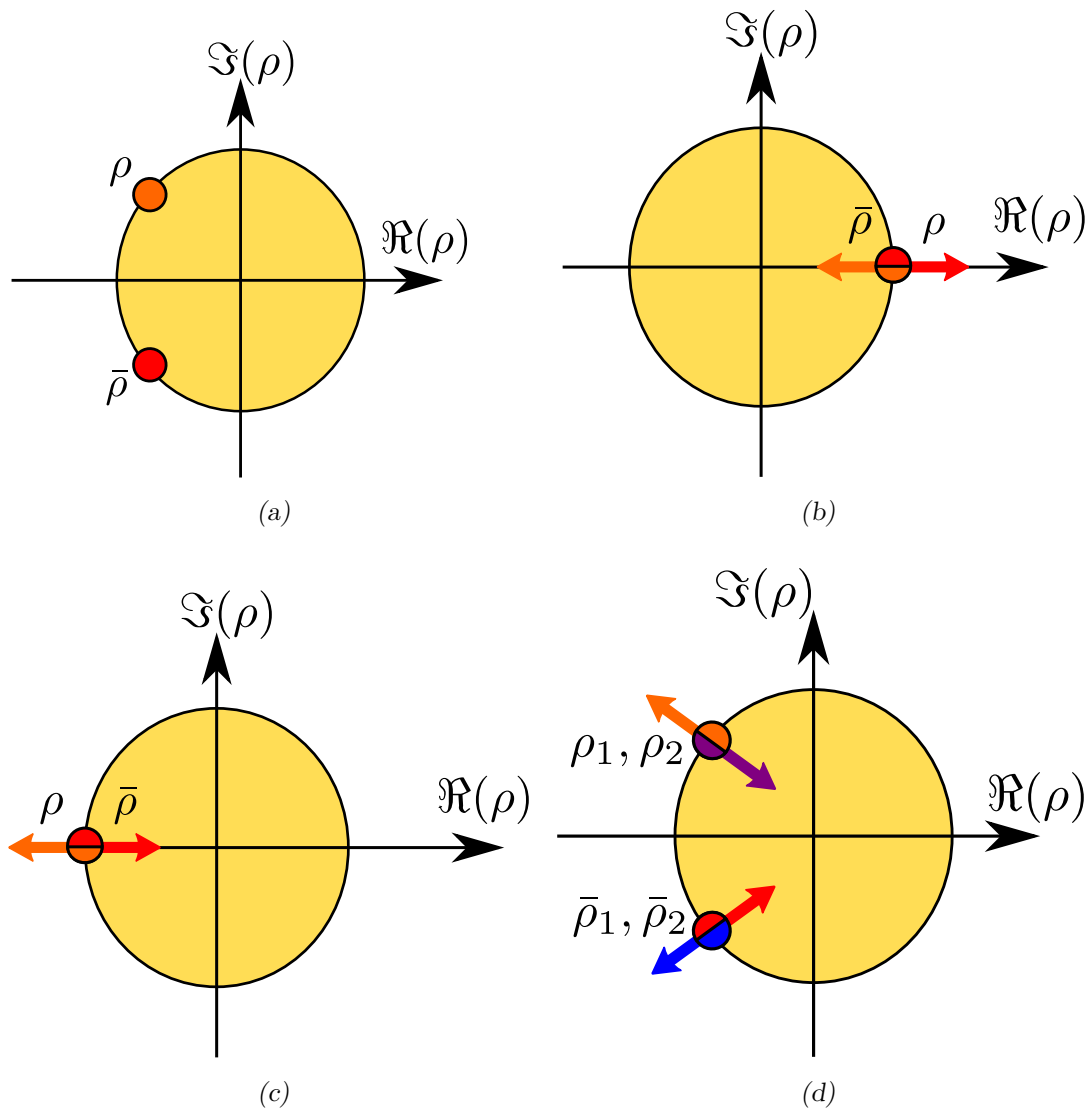


Figure 2.3: Stability analysis using Floquet multipliers with the unit circle in yellow. (a) Neutral stability at  $|\rho| = 1$ . (b) Steady bifurcation leading to a new dynamic stability with response period  $T$  at  $\rho = 1$ . (c) Flip or period doubling bifurcation leading to a new dynamic stability with response period  $2T$  at  $\rho = -1$ . (d) Secondary Hopf or Neimark-Sacker bifurcation leading to a almost-periodic instability.

of the linear response with period  $2T$ . The state of the  $i^{\text{th}}$  Floquet form is given as  $\mathbf{y}_i(t+2T) = 2|\rho_i|\mathbf{y}_i(t)$ . This is referred to as a  $2T$ -instability. In nonlinear analysis a new stationary state with a period  $2T$  would be found.

Figure 2.3(d) shows a Neimark-Sacker bifurcation leading to a new almost-periodic stationary state. The motion of the corresponding emerging nonlinear solution would be almost-periodic. Similar to the nonlinear response as illustrated in fig.2.2(d). This type of bifurcation occurs when two FFs with multipliers  $\rho_1 = \rho_2$  are coupled in a value that is not  $\pm 1$ . This is similar to coupled-mode flutter which is caused by frequency lock-in as illustrated in fig.2.2(c)[75].

## Floquet exponents

The relation between Floquet multipliers and exponents of equation (2.23) is

$$\rho_n \iff e^{s_n T}. \quad (2.44)$$

Both describe how a particular fundamental state is multiplied after one period so that  $\mathbf{y}_n(T) = \rho_n \mathbf{y}_n(0) = \mathbf{y}(0)e^{s_n T}$ .

From the frequency approach shown in section 2.3.3, Floquet exponents  $s_n$  can be directly computed. These exponents determine the frequency and stability of the response  $\mathbf{y}(t) = \sum_{n=1}^N c_n \mathbf{y}_n(t)$  with  $\mathbf{y}_n(t) = \mathbf{p}_n(t)e^{s_n t}$ . The link between constant and time-periodic systems is that the well known Lyapunov exponent is a particular case of Floquet exponent when dealing with the perturbation of equilibrium states. By looking at the long term behavior of the exponential term  $e^{s_n t}$ , the stability of the system is determined by the limit  $\lim_{t \rightarrow \infty} e^{s_n t}$ . If we write the complex Floquet exponent in the form  $s_n = a + ib$ , the computed real part, also known as the growth rate, is the one that determines linear stability of a periodic stationary state:

$$\begin{cases} a < 0, \text{ damped, stable} & \lim_{t \rightarrow \infty} e^{(a+ib)t} = 0, \\ a = 0, \text{ undamped, neutrally stable} & \lim_{t \rightarrow \infty} e^{(a+ib)t} \neq 0, \\ a > 0, \text{ unstable} & \lim_{t \rightarrow \infty} e^{(a+ib)t} = \infty. \end{cases} \quad (2.45)$$

We will come back in more details on the computation and determination of the linear stability of time-periodic systems through Floquet exponents and Floquet forms in chapter 3.

### 2.3.5 Stability analysis of the 2-DoF Ziegler column

A stability analysis is shown on the simple example of the two degrees of freedom Ziegler column with an axial harmonically varying load from section 2.2.1 illustrated in Fig.2.2(c). As already seen, this example has a rich stability behavior, since steady-state, flip and Neimark-Sacker bifurcations are found by changing the modulation parameters of the periodic axial load.

As previously stated, the stability of this time-periodic system can be solved in the time domain by studying the Floquet multipliers of its monodromy matrix or by sorting the spectrum of its finite Hill matrix in the frequency domain. The latter will be explained in more detail in chapter 3 and we will focus on the more classic technique of the monodromy matrix. Varying the fundamental frequency  $\beta$  and amplitude  $\lambda$  of the axial periodic load, different stability types due to different bifurcation types are observed. The difference between the non-conservative  $\eta = 1$  (a following axial load throughout deformation) and conservative case  $\eta = 0$  (a horizontal axial load throughout deformation) results in different types of instabilities.

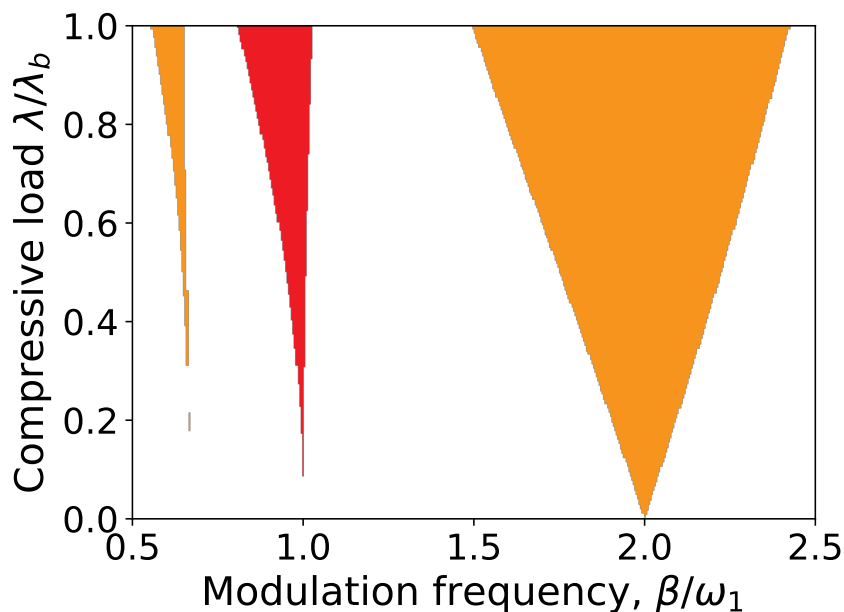


Figure 2.4: Stability chart of the conservative case  $\eta = 0$ . In red the  $T$ -instability is shown. Orange shows the  $2T$ -instability region. The white area is where the straight Ziegler column is stable. The stability is computed on a  $500 \times 500$  grid in the  $(\beta, \lambda)$  modulation parameter space and colors are plotted according to the closest data point.

In Fig.2.4 a stability diagram of the undamped straight Ziegler beam under conservative, harmonically varying axial load is shown. The amplitude of the harmonic load  $\lambda$  varies between 0 and 1.0, where 1.0 is the critical static buckling load of the compressed 2-DoF Ziegler column. The frequencies  $\beta$  are normalized with the first natural frequency  $\omega_1$  of the unloaded system. On a 500 by 500 grid in the  $(\beta, \lambda)$  modulation space, the monodromy matrix is computed as well as its Floquet multipliers. The stability is determined by observing the complex Floquet multipliers in the unit circle as shown in the previous section. We see that stability regions and  $T$  and  $2T$ -instabilities regions alternate under axial loads with various excitation frequency  $\beta$  and amplitude  $\lambda$ .

From literature [11] it is known that time-periodic systems can destabilize at low modulation amplitudes compared to static instabilities. In case of a static compressive load, the beam destabilizes at buckling load  $\lambda = \lambda_b$  and no earlier. While the time-periodic system dynamically destabilizes for example at  $\lambda > 0$  and  $\beta = 2\omega_1$ . This is known as the principal parametric instability region [11].

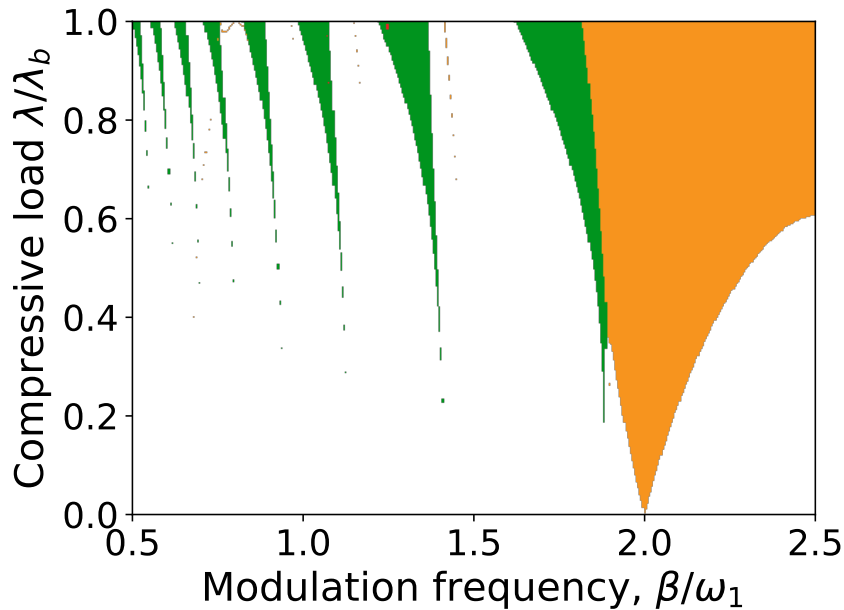


Figure 2.5: Stability chart of the nonconservative case ( $\eta = 1$ ). In green the instability regions where Neimark-Sacker bifurcations take place is shown. Orange shows the  $2T$ -instability regions. The white area is where the system is stable. On the vertical axis is the load  $\lambda$  relative to the classic flutter critical load,  $\lambda_f$ . On the horizontal axis the frequency normalized with the first natural frequency  $\beta/\omega_1$  is shown. The stability is computed on a  $500 \times 500$  grid in the  $(\beta, \lambda)$  modulation parameter space and colors are plotted according to the closest data point.

In Fig.2.5 the stability diagram of the nonconservative case  $\eta = 1$  is shown. This time, the load parameter  $\lambda$  is normalized to the flutter load  $\lambda_f$ . In the modulation parameter space  $(\beta, \lambda)$ , we observe an alternance between stable zones, almost-periodic and  $2T$ -instabilities regions. In the nonconservative case, instabilities are qualitatively different as compared to the conservative case. There are Neimark-Sacker bifurcations leading to almost-periodic instabilities and there are no  $T$ -instabilities observed. The distribution of instability zones itself is different as well. The only similar zone is at  $\beta = 2\omega_1$  leading to the only  $2T$ -instability, although with increasing load the  $2T$ -zone develops very different than its conservative counterpart shown in Fig.2.4.

In chapter 3, we will come back on the numerical determination of the linear stability of the Ziegler column in periodic elastic state, but this time, by looking in detail how to correctly reproduce the stability charts of Figs.2.4 and 2.5 in the frequency domain through Floquet exponents.

## 2.4 Classic Modal Analysis

Modal analysis is a well established tool used in structural engineering. It consists of using modes to compute and gain physical insights in the physical vibratory response of a structure in equilibrium state. A classic normal mode, or harmonic eigenmode, is

composed of a natural frequency and a mode shape. Decomposing a vibratory response into modes relies on the expansion theorem, which states that any vector of size  $N$  can be represented by the sum of  $N$  orthogonal vectors. If this theorem is applied to the vector of degrees of freedom of the discretized cantilever beam of Fig.2.2(a), decomposing the physical vibratory response  $\mathbf{x}(t)$  into  $N$  free vibrating modes reads

$$\mathbf{x}(t) = \sum_{n=1}^N \mathbf{X}_n e^{i\omega_n t}. \quad (2.46)$$

Here, the natural frequencies  $\omega_n$  show at which operating conditions resonance can be expected. The mode shapes  $\mathbf{X}_n$  reveal how loading or constraining a structure changes the vibratory response. For dynamic analysis, modal projection is an important tool for model reduction. Indeed, the number of degrees of freedom in a system can often be projected to a selected number of modes. This allows for much shorter computation time. Also, classic normal modes themselves can be analyzed to decide how to change stiffness and mass properties of a structure.

### Computation of the classic modal basis

Consider the classic linear discrete equations of motion where the stiffness and mass matrices are constant, like it would be the case after applying the finite element method on the cantilever beam of Fig.2.2(a) without periodic prestress and without external load:

$$\mathbf{M}\ddot{\mathbf{x}}(t) + \mathbf{K}_0\mathbf{x}(t) = \mathbf{0}. \quad (2.47)$$

Classic modal analysis consists in rewriting the vibratory response  $\mathbf{x}(t)$  as a linear combination of harmonic eigenmodes. This makes use of the expansion theorem that states a vector can be decomposed into a series of orthogonal vectors. We can then write

$$\mathbf{x}(t) = \sum_n \mathbf{X}_n T_n(t) = \mathbf{X}\mathbf{T}(t). \quad (2.48)$$

For each mode, the time and space variables are separated into two distinct quantities: the space dependent matrix of mode shape  $\mathbf{X}$  and the vector of time dependent modal amplitude  $\mathbf{T}(t)$ .

The equations of motion are transformed to modal coordinates by replacing  $\mathbf{x}(t)$  by its expression (2.48) in (2.47)

$$\mathbf{M}\mathbf{X}\ddot{\mathbf{T}}(t) + \mathbf{K}\mathbf{X}\mathbf{T}(t) = \mathbf{0}. \quad (2.49)$$

Modal coordinates refers to the fact that the physical coordinates of the system  $\mathbf{x}(t)$  are now written as a superposition of modes  $\mathbf{X}\mathbf{T}(t)$ . Modal amplitudes are free variables and can be considered coordinates in this equation.

By imposing the solution  $T_n(t) = e^{i\omega_n t}$  its second derivative is  $\ddot{T}_n(t) = -\omega_n^2 e^{i\omega_n t} = -\omega_n^2 T_n(t)$ . Substituting this in the homogeneous equation of motion (2.49) results in the generalized eigenproblem

$$(\mathbf{K} - \omega_n^2 \mathbf{M}) \mathbf{X}_n e^{i\omega_n t} = \mathbf{0}. \quad (2.50)$$

where the  $e^{i\omega_n t}$  can be discarded. The mode shapes and frequencies are simply found by solving the eigenvectors and eigenvalues, respectively. Solving this eigenproblem can be done by one of many eigensolver algorithms available [76, 77].

### Mode shapes visualization

Here, we compute the mode shapes of the cantilever beam from section 2.2.2 illustrated in Fig.2.2(a) but with no periodic prestress thanks to the FEM-software FEniCS [71]. The finite element model for this case has  $N = 108$  degrees of freedom.

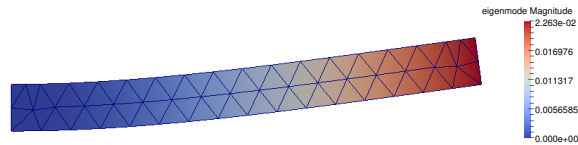


Figure 2.6: First bending mode shape of the discretized cantilever beam which has a natural frequency  $\omega_1 = 21.433$  rad/s.

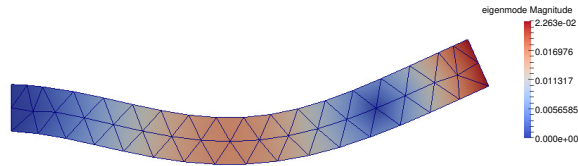


Figure 2.7: Second bending mode shape of the discretized cantilever beam which has a natural frequency  $\omega_2 = 127.015$  rad/s.

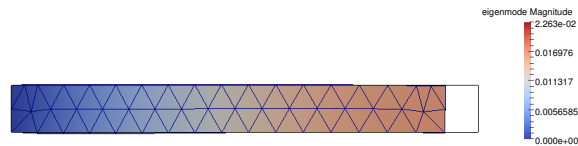


Figure 2.8: Third mode shape of the discretized cantilever beam which has a natural frequency  $\omega_3 = 271.587$  rad/s. This is a compression mode, the original shape is shown with black lines.

In Fig.2.6 the first bending mode is shown. The color indicates displacement magnitude. In Fig.2.7 the second bending mode is shown when Fig.2.8 shows a compression mode (to show this clearly the reference configuration of the beam is shown in black). These mode shapes are representations of the vector  $\mathbf{X}_n$  with  $n = 1, 2, 3$ . These principal or natural vibrational motions capture important information when projecting on them. Usually only a few modes are necessary to get an accurate representation of the system vibratory response [78].

### 2.4.1 Modal projection of the cantilever beam with periodic prestress

Once modes are computed, these are often used to project linear discrete equations of motion. Projection has the advantage that the equations can then be reduced because a small basis of modes is often sufficient to capture the physics underlying the vibration. Furthermore algebraic solutions could be found for certain types of excitation, avoiding time-integration of dynamic problems, especially when dealing with classic systems in the form (2.47).

Here, taking the equations of motion (2.21) of the beam in periodic elastic states and projecting them on  $n$  classic eigenmodes  $\mathbf{x}(t) = \mathbf{X}\mathbf{T}(t)$ , where the modes are computed using the constant mass  $\mathbf{M}$  and material stiffness  $\mathbf{K}_0$  matrices (as shown before) results in

$$\ddot{\mathbf{T}}(t) + \left( \omega_n^2 + \lambda \hat{\mathbf{K}}_c \cos(\beta t) \right) \mathbf{T}(t) = \mathbf{X}^T \mathbf{F}(t). \quad (2.51)$$

The modal projected matrices  $\hat{\mathbf{K}}_c$ ,  $\omega_n^2$  and  $\mathbf{M}$  are of size  $n \times n$  and modal amplitude  $\mathbf{T}(t)$  and modal excitation  $\mathbf{X}^T \mathbf{F}(t)$  are of size  $n \times 1$ . The modal projected mass matrix is unity  $\mathbf{X}^T \mathbf{M} \mathbf{X} = \mathbf{1}$  and the material stiffness results in a diagonal matrix with modal frequencies squared  $\mathbf{X}^T \mathbf{K}_0 \mathbf{X} = \omega_n^2$ . The geometric stiffness, expressed as  $\lambda \hat{\mathbf{K}}_c \cos \beta t = \lambda \mathbf{X}^T \mathbf{K}_c \mathbf{X} \cos \beta t$ , is the projected periodic geometric stiffness matrix. Note that the geometric stiffness is defined by its fundamental frequency  $\beta$  and amplitude scaling  $\lambda$  where  $\lambda = 1$  corresponds to the compressive buckling matrix  $\mathbf{K}_g = \mathbf{K}_c$ .

In the projected equations (2.51),  $\lambda \hat{\mathbf{K}}_c \cos(\beta t)$  is a time dependent full matrix. This is because classic modal analysis is defined on ODEs with constant coefficients and does not decouple periodic problems because it is not a full orthonormal basis for the whole period.

#### Classic case with no prestress ( $\lambda = 0$ )

When applying modal analysis on a linear time independent system which is the case of equation (2.51) with  $\lambda = 0$ , the equations of motion in the modal basis are fully decoupled. The equations can be truncated up to a small number of modes that significantly contribute to the vibratory response  $\mathbf{x}(t)$ . Furthermore this has the advantage that for certain cases, an analytical solution can be found for the modal amplitude response.

The equation of motion is homogeneous when there is no excitation. For modes this leads to  $n$  simple undamped harmonic motions:  $\ddot{T}_n(t) + \omega_n^2 T_n(t) = 0$ . The solution to these equations can be formulated as  $T_n(t) = C_n e^{i\omega_n t}$  where  $C_n = T_n(0)$ . From a structural engineering point of view these solutions are transient vibrations that in practice dampen out over time.

The particular solution represents the steady state of a system undergoing excitation. The steady state itself is computed using modal projection of the force  $\mathbf{X}^T \mathbf{F}(t)$ . In case

of a harmonic excitation this results in

$$\ddot{\mathbf{T}}(t) + \boldsymbol{\omega}_n^2 \mathbf{T}(t) = \mathbf{X}^T \mathbf{F}_0 \cos(\Omega t), \quad (2.52)$$

where  $\mathbf{F}_0$  is the excitation amplitude and  $\Omega$  is the excitation frequency. The corresponding particular solution to this undamped problem is in the form  $\mathbf{T}(t) = \mathbf{T}_0 \cos(\Omega t)$  where the amplitude for each mode  $i$  is given by  $T_{i0} = \frac{X_i^T \mathbf{F}_0}{\omega_i^2 - \Omega^2}$ . Note that when the excitation frequency  $\Omega$  approaches the modal frequency  $\omega_i$  the denominator goes to zero, meaning the amplitude goes to infinity (2.53):

$$\lim_{\Omega \rightarrow \omega_i} \frac{X_i^T \mathbf{F}_0}{\omega_i^2 - \Omega^2} \rightarrow \infty. \quad (2.53)$$

This is the resonance phenomenon. In practice there will be damping or nonlinearities limiting the linear vibratory response. However when analyzing a linear undamped case, the resonance response diverges to infinity.

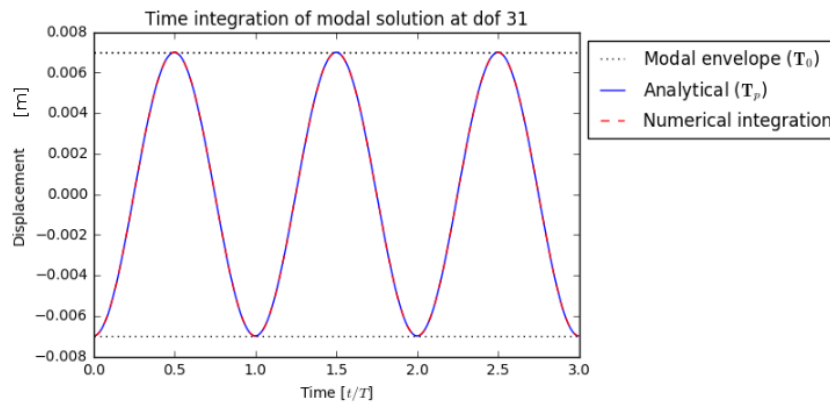


Figure 2.9: Particular solution of a cantilever beam with no prestress under harmonic excitation. The modal solution  $\mathbf{q}_p(t)$  is compared to direct time integration. Envelopes are computed from  $|\mathbf{q}_0|$ . The line force applied on top of the beam is  $500 \text{ Nm}^{-1}$  with a fundamental frequency of  $2.9\omega_1$ . The number of modes used in the modal basis is  $n = 10$ .

The steady state solution of the cantilever beam with no prestress under a harmonic excitation is shown in figure 2.9. The finite element model for this case has  $N = 108$  degrees of freedom and is projected on  $n = 10$  modes. The system's initial condition is chosen such that  $\mathbf{x}(0) = \sum_{n=1}^N \mathbf{X}_n T_n(0)$ . The modal response (red),  $\mathbf{T}_p(t) = \mathbf{T}_0 \cos(\Omega t)$ , has been validated with a direct numerical time integration scheme (blue). The response envelope is found from  $\pm|\mathbf{T}_0|$  which determines the system's maximum response.

The frequency spectrum of the response is shown in fig.2.10. This frequency has been computed by taking a response signal at a specific degree of freedom over 150 periods. From this the Fourier spectrum is computed numerically. This spectrum shows a peak at the excitation frequency since the response is expressed by  $\mathbf{T}_p(t) = \mathbf{T}_0 \cos(\Omega t)$ . This verifies that the only frequency of importance in steady state response is the excitation frequency in the case of the transverse forced vibration of a structure in equilibrium state.

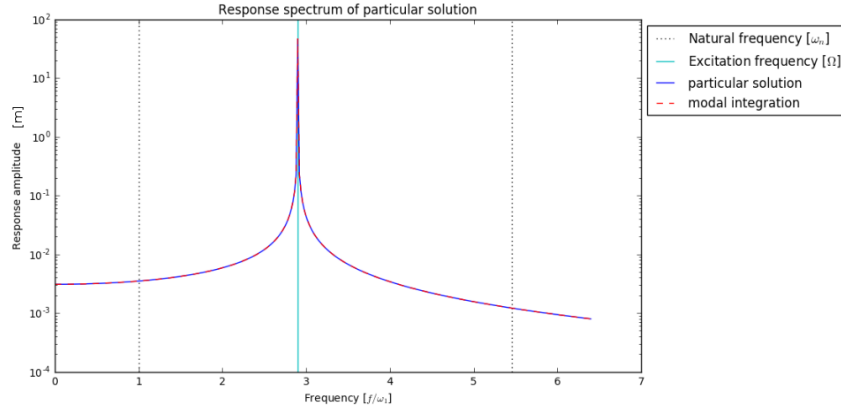


Figure 2.10: Frequency response spectrum of the cantilever beam with no prestress undergoing harmonic excitation. The peak at frequency  $\Omega = 2.9\omega_1$  corresponds with the excitation frequency.

### The case of periodic prestress ( $\beta \neq 0$ and $\lambda \neq 0$ )

For the periodic case the modal solutions cannot be used the same way as in the time invariant case. The difference is that the left hand side of the equations are now periodic. The equations are coupled through the periodic stiffness matrix  $\lambda \hat{\mathbf{K}}_c \cos \beta t$ . Therefore exact solutions cannot be found, however it is possible to integrate solutions over time using an ODE solver.

To analyze the system, the time-periodic equations of motion reduced in a classic modal basis (2.51) are integrated over time. Like in the previous part, we analyze the stationary transverse vibratory response of the cantilever beam under an external harmonic force that reads  $\mathbf{F}(t) = \mathbf{F}_0 \cos \Omega t$ . But this time, the beam is in periodic elastic state.

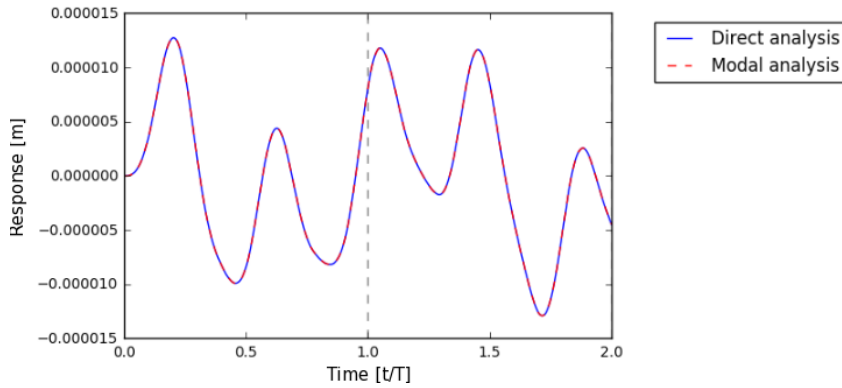


Figure 2.11: Modal time integration for a periodically prestressed beam undergoing an external harmonic load. The prestress has a fundamental frequency  $\beta = 1.5\omega_1$  and a modulation amplitude  $\lambda = 0.5$ . The line force applied on top of the beam is  $500 \text{ Nm}^{-1}$  with a frequency of  $2.9\omega_1$ . The number of modes used in the modal basis is  $n = 10$ .

In fig.2.11 the forced vibratory response over time is plotted. The time integration in the classic reduced modal basis is compared to direct time integration of the original equations of motion for validation. The response of modal and direct time-integration are in good agreement for  $n = 10$ . Therefore the reduced modal equations can be used

to compute the response of the system. This has the advantage that response can be computed in a much smaller set of equations, thereby increasing calculation speed.

Comparing the constant and time-periodic forced vibratory response from figures 2.9 and 2.11, respectively, we see that the main difference is the multi-harmonic response in the case where the beam is in periodic elastic state. Instead of a single harmonic for the constant case. To get a better understanding of what frequencies are in the response we need to look at the frequency response spectrum.

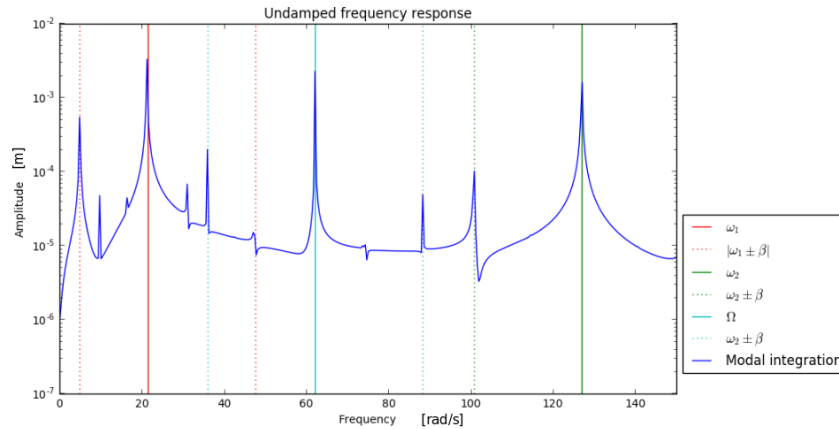


Figure 2.12: Frequency response for a periodically prestressed beam under a harmonic load. With prestress frequency  $\beta = 1.5\omega_1$  and excitation frequency  $\Omega = 2.9\omega_1$ . The number of DoFs is 108 and the line force applied is  $500 \text{ Nm}^{-1}$ . The Fourier transform of the response of 75 prestress periods computed using  $n = 10$  modes is shown. The natural frequencies are noted  $\omega_i$ , with  $i = 1, 2, 3$ . The first subharmonics are shifted with  $\beta$  from natural and excitation frequencies and illustrated by dotted lines.

In fig.2.12 the frequency response of the transverse vibrations of the periodically prestressed beam under harmonic load is shown. Since we look at the undamped general response both the natural as well as the excitation frequencies are found. The subharmonic frequencies  $\Omega \pm \beta$  are a fundamental difference with the frequency response of time-invariant systems shown in Fig.2.10.

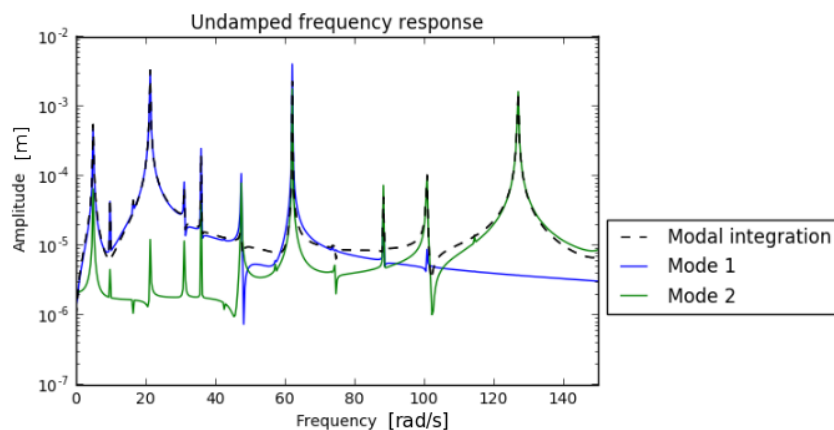


Figure 2.13: Frequency response for a periodically prestressed beam under a harmonic load per mode. The first mode (blue) and second mode (green) are shown. For comparison the frequency response spectrum of the total response is shown in dotted black lines.

In fig.2.13 the frequency response spectrum per mode is analyzed. The modal response is slightly coupled because of the full periodic geometric stiffness matrix  $\hat{\mathbf{K}}$ . This can be seen by the peaks in mode 2 around the first natural frequency and the subharmonics of the first natural frequency.

Using classic modal analysis we have now reached the limit of what we can analyze about time-periodic systems. The response can be computed on a reduced basis. This increases the speed of dynamic analyses or can be used to compute the frequency response function of a time-periodic system. But one of the main advantage of classic modal analysis, namely decoupling the equations of motion, is no longer valid for time-periodic systems. We will see in chapter 4 that this decoupling will be affective in a basis of Floquet forms.

## 2.5 Conclusions

We have introduced in this chapter linear time-periodic (LTP) systems whose governing equations are characterized by ODEs with periodically repeating coefficients. Those systems notably model structures in periodic elastic states that are ubiquitous in structural vibration. Linear time-invariant (LTI) systems govern the transverse vibration of structures in equilibrium states and they can be seen as particular cases of LTP systems.

Modal analysis is a well established method to compute and gain physical insights in the solutions of LTI systems. Classic harmonic eigenmodes are used effectively for modal reduction and stability analysis of systems in equilibrium states. The limits of their applications are linear time invariant systems since classic modes are not a full orthonormal basis for time-periodic systems. Floquet forms (FFs), introduced in Floquet theory, would be good candidates for generalization of modal analysis to time-periodic systems but the FF periodic eigenvectors are almost never used in literature.

Instead, Floquet theory is almost uniquely applied for stability analysis of time-periodic systems. By using time domain methods and integrating the equations over time the Monodromy matrix can be computed. By solving its eigenvalues, the Floquet multipliers are obtained which give stability of the solutions of LTP systems. Another method to analyse stability is through the frequency domain, by computing the eigenvalues, or Floquet exponents, of Hill's matrix. These are related to Floquet multipliers and determine stability as well. Both these stability analysis methods make use of some Floquet forms information but the FF periodic eigenvectors, or modal shapes, that could allow for a proper generalization of modal analysis of structures in periodic states, are often neglected, even though they are usually available from the eigenvalue computation.

To properly generalize modal and stability analysis to time-periodic systems, Floquet forms need to be computed efficiently and robustly, especially in the frequency domain where classic eigenmodes are usually computed and where current methods based on Hill matrix are questionable due to truncation errors. Thus, computing FFs in the frequency domain is treated in chapter 3. Applying FFs to project the equations of motion of the transverse vibration of a beam in periodic elastic state in order to generalize modal

analysis to LTP systems is treated in chapter 4.



# Frequency domain analysis of Floquet forms

---

## 3.1 Introduction

In this chapter the computation of Floquet forms (FFs) is discussed. FFs are the time-periodic generalization of classic modes for linear time-invariant (LTI) systems. That is to say, FFs allow to orthogonally decomposed solutions of linear time-periodic (LTP) equations of motion and one could project LTP systems on its basis of FFs to obtain a reduced, uncoupled LTI system. This mathematically means we can linearly decompose the state vector  $\mathbf{y}(t)$  into a finite number of Floquet forms

$$\mathbf{y}(t) = \sum_{i=1}^m c_m \mathbf{p}_i(t) e^{s_i t}. \quad (3.1)$$

In eqn.(3.1),  $m$  FFs  $\mathbf{p}_i(t) e^{s_i t}$  are used in the FFs basis. This orthogonality property is important because this allows us to gain physical insights in the structural vibratory response by analyzing individual FFs. An individual FF consists of a Floquet amplitude  $q_m(t) = c_m e^{s_m t}$  and a periodic eigenvector  $\mathbf{p}_m(t)$ . In case of a autonomous time-periodic problem (free vibrations),  $\dot{\mathbf{y}}(t) = \mathbf{J}(t)\mathbf{y}(t)$ , the Floquet amplitude is expressed as  $q_i(t) = q_i(0) e^{s_i t}$  where  $q_i(0)$  is the initial condition projected on the  $i^{th}$  FF modes and  $s_i$  is the  $i^{th}$  Floquet exponent. Alike for classic modes,  $s_i$  is a complex number which determines stability and the natural fundamental frequency of the free vibration of a structure in periodic elastic state. The fundamental frequencies are important to determine where resonances occur and can tell a designer which critical frequencies to avoid in structural engineering. However, resonances are more complicated for LTP systems than LTI systems because internal resonances can occur.

Besides stability and critical frequencies, FFs describe structural displacement patterns. The FF eigenfunction  $\mathbf{p}_i(t)$  is what describes the shape of the intrinsic vibratory response. Alike constant modal shapes of LTI system,  $\mathbf{p}_i(t)$  is an eigenfunction of the LTP system but it is time-dependent and periodic. Those eigenfunctions can be useful for dynamic analysis, as it reveals the principal vibratory motions of the system. Furthermore the periodic response envelope of the almost-periodic oscillations is determined by the eigenfunction as well. These properties allow an analyst to assess whether a periodic system is within its operational envelope.

The main difficulty is in computing and applying Floquet forms. There are two methods available: integrating STM vectors in the time domain that is classic or computing

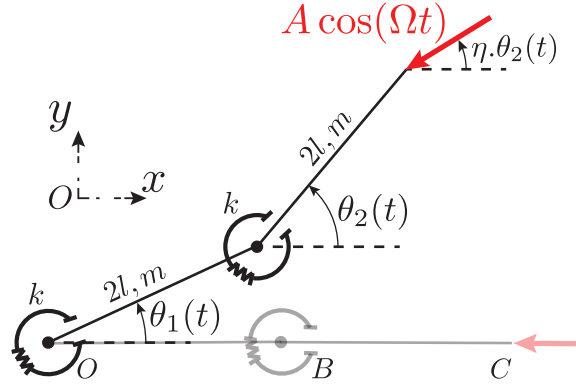


Figure 3.1: The 2D structure under study is a bi-articulated bar submitted to a compressive periodic load at its end either conservative ( $\eta = 0$ , i.e. horizontal force) or non conservative ( $\eta = 1$ , i.e. following force).

Hill matrix eigensolutions in the frequency domain that is more questioned in the literature. Both methods start from Floquet theory by transforming the response into FFs thanks to (3.1).

The results in this chapter give physical insights on the natural relation between classic harmonic modes of vibrations and Floquet modes for structures that are in periodic elastic states. This chapter also clarifies the debate about the Floquet-Hill frequency method to assess the stability of periodic states by clearly showing the necessity of sorting the spectral outcomes of the Hill matrix in the frequency domain. Those results pave the way for a modal analysis of structures in periodic states that will be developed in chapter 4 and the use of Floquet forms for stability analysis, structural design, or as candidates for modal reduction techniques.

To illustrate the method the case of the modulated Ziegler column is analyzed. This case was introduced in section 2.2.1 and is illustrated again in Fig.3.1. This case is a simple yet fundamental benchmark. Either a conservative horizontal or a nonconservative following axial periodic load is applied to the Ziegler column. The linear equations of motion have been derived in chapter 2 and resulted in periodically time varying linear ordinary differential equations describing the transverse linear oscillations about the trivial state. This case is used to show FFs could be used as time periodic generalizations of modes. By investigating stability and FF properties the similarities and differences of FFs to classic modes are analyzed. As a reminder, the time periodic linear equations of motion in the physical domain of our Ziegler column are recall

$$\mathbf{M}\ddot{\mathbf{x}}(\tau) + \mathbf{K}(\tau)\mathbf{x}(\tau) = \mathbf{0}. \quad (3.2)$$

where

$$\mathbf{x}(\tau) = \begin{Bmatrix} \theta_1(\tau) \\ \theta_2(\tau) \end{Bmatrix}, \quad \mathbf{M} = \begin{bmatrix} 1 & \frac{3}{8} \\ \frac{3}{2} & 1 \end{bmatrix}, \quad \mathbf{K}(\tau) = \begin{bmatrix} \frac{3}{8} & \frac{3}{4} \\ -\frac{3}{4} & \frac{3}{4} \end{bmatrix} + \lambda \cos(\beta\tau) \begin{bmatrix} -1 & \eta \\ 0 & 4\eta - 4 \end{bmatrix}.$$

The angular displacements are formulated into the vector  $\mathbf{x}(\tau)$ . The dimensionless time variable  $\tau = \omega_n t$  was used to simplify the equation. The harmonically varying stiffness

matrix has the dimensionless load parameter  $\lambda$  and frequency  $\beta$ . The parameter  $\eta$  determines whether the load follows angle  $\theta_2$  resulting in either conservative ( $\eta = 0$ ) or nonconservative ( $\eta = 1$ ) problems.

Since all our computations will be performed in the state space, we transform the equation (3.2) in the form

$$\dot{\mathbf{y}}(\tau) = \mathbf{J}(\tau)\mathbf{y}(\tau). \quad (3.3)$$

where the state vector  $\mathbf{y}(\tau)$  and  $T$ -periodic Jacobian were derived in section 2.1.3 and read

$$\mathbf{y}(\tau) = \begin{pmatrix} \dot{\mathbf{x}}(\tau) \\ \mathbf{x}(\tau) \end{pmatrix}, \quad \mathbf{J}(\tau) = \begin{bmatrix} \mathbf{I} & \mathbf{0} \\ \mathbf{0} & -\mathbf{M}^{-1}\mathbf{K}(\tau) \end{bmatrix}, \quad \mathbf{J}(\tau) = \mathbf{J}(\tau + T). \quad (3.4)$$

## 3.2 Time-domain method

Computing the Floquet forms (FFs) of LTP systems is important in understanding trends and patterns of the system's vibratory response. In order to do so, the goal is to find the Floquet exponents and periodic eigenvectors. Floquet exponents can be obtained through Floquet multipliers as described in section 2.3.2. In this section, we explain how to obtain the periodic eigenvectors in the time domain through the State Transition Matrix (STM) and monodromy matrix that have already been introduced for computing the linear stability of solutions of LTP systems.

Computing Floquet forms in the time domain is a classic method to analyze time-periodic systems. This approach has been described in the literature [79]. It has been used to implement modal control [39]. An efficient computation method is by using a shooting method to compute the monodromy matrix [37] or by using Chebyshev polynomials [40]. An overview of different methods to compute the monodromy matrix is given in [51].

### 3.2.1 STM eigenvectors

The starting point to compute the time-periodic eigenfunctions  $\mathbf{p}_i(t)$  of the Floquet decomposition given in equation (3.1) is the linear time periodic problem in state space  $\dot{\mathbf{y}}(\tau) = \mathbf{J}(\tau)\mathbf{y}(\tau)$ . First, the STM matrix, already described in section 2.3.2, is introduced in the equations of motion:

$$\mathbf{y}(\tau) = \Phi(\tau, \tau_0)\mathbf{y}(\tau_0). \quad (3.5)$$

It is independent of initial conditions and the STM itself is time dependent but not periodic. To simplify equations the initial time is set to zero  $\tau_0 = 0$ . Inserting equation (3.5) in the state space equation (3.3) gives the STM derivative

$$\dot{\Phi}(\tau, \tau_0) = \mathbf{J}(\tau)\Phi(\tau, \tau_0). \quad (3.6)$$

By rewriting the STM as  $\Phi(\tau, 0) = \mathbf{y}(\tau)\mathbf{y}^{-1}(0)$  and applying a Floquet transform on the vector of state variables  $\mathbf{y}(\tau) = \mathbf{p}(\tau)e^{s\tau}$  where  $\mathbf{p}(t) = \{\mathbf{p}_1(t), \dots, \mathbf{p}_m(t)\}$  is an  $N \times m$ -matrix with periodically repeating eigenfunctions in columns and  $\mathbf{s}$  is a diagonal matrix whose entries are Floquet exponents  $s_i$  for  $i = 1, \dots, m$ , the STM can then be decomposed in its Floquet forms

$$\Phi(\tau, 0) = \mathbf{p}(\tau)e^{s\tau}\mathbf{p}^{-1}(0). \quad (3.7)$$

Plugging the decomposed STM formulation (3.7) and its derivative,

$$\dot{\Phi}(\tau, 0) = (\dot{\mathbf{p}}(\tau) + \mathbf{s}\mathbf{p}(\tau))e^{s\tau}\mathbf{p}^{-1}(0) \quad (3.8)$$

into equation (3.6), leads to an expression for the FFs over time

$$\dot{\mathbf{p}}(\tau) = \mathbf{J}(\tau)\mathbf{p}(\tau) - \mathbf{p}(\tau)\mathbf{s}. \quad (3.9)$$

For an individual Floquet form this expression becomes

$$\dot{\mathbf{p}}_n(\tau) = (\mathbf{J}(\tau) - s_n\mathbf{I})\mathbf{p}_n(\tau). \quad (3.10)$$

Integrating the Floquet eigenfunction over time is possible, although there are two problems. The Floquet exponent  $s_n$  is not known and there is no starting point for the periodic eigenvector  $\mathbf{p}_n(\tau)$ . These issues are resolved by considering the monodromy matrix.

The matrix of periodic eigenvectors  $\mathbf{p}(\tau)$  is found with the help of the monodromy matrix eigenproblem. Since the monodromy matrix is defined as the STM at the fundamental period, its expression is quite similar to (3.7), although the time is set to one period  $\tau = T$ :

$$\mathbb{M} = \mathbf{p}(T)e^{sT}\mathbf{p}^{-1}(0) = \mathbf{p}(0)\mathbf{B}\mathbf{p}^{-1}(0). \quad (3.11)$$

Thus, computing the spectrum of the monodromy matrix  $\mathbb{M}$ , Floquet eigenvectors  $\mathbf{p}(\tau)$  are found at initial time  $\tau = 0$  (in equation (3.11), we have used the periodicity of the eigenvectors  $\mathbf{p}(T) = \mathbf{p}(0)$ ). Note that the Floquet exponent is not found directly. Instead, the Floquet multipliers  $\boldsymbol{\rho}$  are found when solving the monodromy eigenproblem. We recall that the relation between the diagonal matrix of Floquet multipliers  $\boldsymbol{\rho}$  and the one of Floquet exponent  $\mathbf{s}$  reads

$$\boldsymbol{\rho} = e^{sT} \iff \frac{1}{T} \log \boldsymbol{\rho} = \mathbf{s}. \quad (3.12)$$

Now that the Floquet exponent and initial vector are known, the periodic eigenfunction  $\mathbf{p}(\tau)$  can be integrated over time through equation (3.10). All components of the Floquet forms are known when the spectrum of the monodromy matrix is computed and the time integration of equation (3.10) is done. Note that we from equation (3.11) that the Floquet exponents found are not unique, since the equation  $e^{(s+ik\beta)T} = \mathbf{B}$  holds for any integer  $k$ . However, the computed exponent with the presented time method always has an imaginary value that falls in the region  $-i\beta/2 \leq \Im(s_n) < i\beta/2$  (denoted as the primitive cell in the frequency domain) because the Floquet exponent is obtained from the Floquet multiplier defined in the relation (3.12).

Here, the periodic eigenfunctions  $\mathbf{p}(\tau)$  are integrated directly over time. A disadvantage is that this leaves out frequency information, which would have been directly known if a spectral approach has been used.

### 3.3 Hill Matrix

Computing Floquet forms in the frequency domain requires careful treatment of Hill's spectrum to find converged Floquet forms. In section 2.3.3 the frequency domain approach for Floquet theory has been introduced. This approach is also known as Hill's method [50] or Floquet-Fourier-Hill transform [80]. The Hill matrix can be derived in either the complex (section 3.3.1) or the real frequency domain (section 3.3.2).

A crucial point we have already expressed is that the spectrum of Hill's matrix with a finite dimension is spurious and is therefore not to be used directly, without sorting it. For this purpose, strategies have been developed to sort FFs out of the Hill spectrum. These strategies are based on sorting the eigenvector or eigenvalues of the spectrum [62]. In the following, we will study and challenge those sorting methods on the canonical case of the Ziegler column in periodic elastic state.

#### 3.3.1 Complex Hill Matrix Derivation

The first step to establish the Hill matrix in the complex domain is to transform the vector of state variables  $\mathbf{y}(\tau)$  of the considered LTP system,  $\dot{\mathbf{y}}(\tau) = \mathbf{J}(\tau)\mathbf{y}(\tau)$ , in its Floquet form in order to be able to expand the periodic eigenfunction  $\mathbf{p}_n(\tau)$  in a complex Fourier series

$$\mathbf{y}_n(\tau) = \mathbf{p}_n(\tau)e^{s_n\tau} = \sum_{h=-\infty}^{\infty} \mathbf{p}_n^h e^{(s_n+ih\beta)\tau} \quad (3.13)$$

where  $\beta$  is the fundamental frequency of the  $T$ -periodically time-varying Jacobian matrix  $\mathbf{J}(\tau)$ . A second step is to expand  $\mathbf{J}(\tau)$  in the complex Fourier series

$$\mathbf{J}(\tau) = \sum_{k=-\infty}^{+\infty} \mathbf{J}^k e^{ik\beta\tau} \quad (3.14)$$

Note that in this work, we would like to compute the FFs and stability of the Ziegler column under a harmonically varying axial load. In this case, the Fourier series from equation (3.14) is simplified in a closed analytical form as the contributions of  $\mathbf{J}(\tau)$  of equation (3.3) is limited to the fundamental and first harmonic only, i.e.  $\mathbf{J}^k = \mathbf{0}_N$  for  $|k| > 1$ . This results in a constant and cosine part:  $\mathbf{J}(\tau) = \mathbf{J}^0 + \mathbf{J}_c^1 \cos \beta\tau = \mathbf{J}^{-1}e^{-i\beta\tau} + \mathbf{J}^0 + \mathbf{J}^1e^{i\beta\tau}$ .

The Floquet-Fourier transformed state vector of equation (3.13) and the Fourier transformed Jacobian matrix of equation (3.14) are substituted into the state space equation (3.3). This results in a harmonic balance formulation:

$$\sum_{h=-\infty}^{\infty} \sum_{k=-\infty}^{\infty} [\mathbf{J}^k \mathbf{p}_n^{h-k} - (s_n + ih\beta)\mathbf{p}_n^h] e^{(s_n+ih\beta)t} = \mathbf{0}. \quad (3.15)$$

This harmonic balance is rewritten into matrix form, resulting in an eigenvalue problem:

$$(\mathbf{H}^H - s\mathbf{1}) \mathbf{q}^H = \mathbf{0} \quad (3.16)$$

where the Hill matrix  $\mathbf{H}^H$  takes  $H$  harmonics into account. Each block row in this matrix stands for a different harmonic. For example, when looking at  $\mathbf{H}^2$ :

$$\mathbf{H}^2 = \begin{bmatrix} \mathbf{J}^0 + i2\beta\mathbf{1}_4 & \mathbf{J}^{-1} & \mathbf{J}^{-2} & \mathbf{J}^{-3} & \mathbf{J}^{-4} \\ \mathbf{J}^1 & \mathbf{J}^0 + i\beta\mathbf{1}_4 & \mathbf{J}^{-1} & \mathbf{J}^{-2} & \mathbf{J}^{-3} \\ \mathbf{J}^2 & \mathbf{J}^1 & \mathbf{J}^0 & \mathbf{J}^{-1} & \mathbf{J}^{-2} \\ \mathbf{J}^3 & \mathbf{J}^2 & \mathbf{J}^1 & \mathbf{J}^0 - i\beta\mathbf{1}_4 & \mathbf{J}^{-1} \\ \mathbf{J}^4 & \mathbf{J}^3 & \mathbf{J}^2 & \mathbf{J}^1 & \mathbf{J}^0 - i2\beta\mathbf{1}_4 \end{bmatrix}. \quad (3.17)$$

$\mathbf{H}^2$  of equation (3.17) is the complex Hill matrix truncated to the order  $H = 2$ ,  $\mathbf{1}_N$  is the identity matrix of size  $N$  ( $N = 4$  in the state space of the Ziegler column under study),  $\mathbf{1}$  is the identity matrix of size  $N(2H + 1) \times N(2H + 1)$  and  $\mathbf{0}$  is a null matrix of dimension  $N(2H + 1) \times N$ .

Computing the spectrum of the square Hill matrix  $\mathbf{H}^H$  with size  $N(2H + 1) \times N(2H + 1)$ , we get  $N(2H + 1)$  eigenvalues  $s_l$  and complex eigenvectors  $\mathbf{q}_l^H$  of size  $N(2H + 1) \times 1$ . For  $H = 2$ ,  $\mathbf{q}_l^{H=2}$  is in the form  $\mathbf{q}_l^{H=2} = \{\mathbf{p}_l^{-2} \mathbf{p}_l^{-1} \mathbf{p}_l^0 \mathbf{p}_l^1 \mathbf{p}_l^2\}^T$  where  $\mathbf{p}_l^h$  is the harmonic contribution of the  $l^{\text{th}}$  Floquet form  $\mathbf{y}_l(\tau)$  given in Eq.(3.13). Replacing the computed eigenvalues  $s_l$  and eigenvectors  $\mathbf{q}_l^H$  in the expression Eq.(3.13), we get  $N(2H + 1)$  numerically approximated Floquet forms  $\mathbf{y}_l(\tau)$ . Since we were theoretically expecting  $N$  Floquet forms in the state space, some information is redundant and some interpretation is needed.

When the number of harmonic goes to infinity  $H \rightarrow \infty$ , the computed eigenvalues and eigenvectors are not all independent. Actually, there are  $N$  independent families of solutions that verify the relations  $s_{n+k} = s_n + ik\beta$  and  $\mathbf{p}_{n+k}^{h+k} = \mathbf{p}_n^h$  for  $n = 1 \dots N$ ,  $-\infty < k < +\infty$  and  $-\infty < h < +\infty$ . By replacing the  $N$  families of infinite eigenvalues and eigenvectors in Eq.(3.13), only  $N$  Floquet forms  $\mathbf{y}_n(\tau)$  are obtained, the rest of the information being redundant. In practice, when truncating  $H$  to a finite value, only some of the  $N(2H + 1)$  computed eigenvalues  $s_l$  and eigenvectors  $\mathbf{q}_l^H$  eventually converge, as  $H$  is increased, to the aforementioned relations; some of the spectrum is spurious, whatever the chosen truncation order. The presence of this spurious spectrum lies in the fact that the infinite Hill operator  $\mathbf{H}^\infty$  is self-adjoint when the truncated one  $\mathbf{H}^H$  is not. As a consequence, there is a necessity to sort the computed spectrum to obtain the  $N$  converged Floquet forms. Based on the particular relations between eigenvalues or eigenvectors that exist for  $H \rightarrow \infty$ , two different sorting strategies can be used:

1. *Eigenvalue sorting*: For the converged part of the computed spectrum, we have the particular relations  $s_{n+k} = s_n + ik\beta$  for  $n = 1 \dots N$  and  $-H \leq k \leq +H$ . By taking the  $N$  eigenvalues whose imaginary parts are contained in the spectral primitive cell  $-\beta/2 \leq \Im(s_l) < \beta/2$ , the latter will eventually converge to Floquet exponents as  $H$  is increased. Replacing those  $N$  converged eigenvalues  $s_l$  with their associated eigenvectors  $\mathbf{q}_l^H$  in Eq.(3.13), we can reconstruct the  $N$  Floquet forms  $\mathbf{y}_n(\tau)$ . The convergence of the sorted eigenvalues has been rigorously proved [57, 58].
2. *Eigenvector sorting*: Since the converged eigenvectors verify  $\mathbf{p}_{n+k}^{h+k} = \mathbf{p}_n^h$  for  $-H \leq k \leq +H$  and  $-H \leq h \leq +H$ , the  $N$  fundamental eigenvectors  $\mathbf{q}_n^H$  associated with the fundamental Floquet exponents  $s_{n+k} = s_n + ik\beta$  for  $k = 0$ , are the most symmetric ones as compared to  $\mathbf{p}_n^0$  [20]. To compute those  $N$  fundamental eigenvectors

in practice, we compute the  $N \times (2H + 1)$  weighted means  $w_l = \sum_h h |\mathbf{p}_l^h| / \sum_h |\mathbf{p}_l^h|$ . In this dual space, the converged spectrum verifies  $w_{n+k} = w_n + k$ . The  $N$  eigenvectors and associated eigenvalues that lead to the  $N$  fundamental Floquet forms  $\mathbf{y}_n(\tau)$  through Eq.(3.13), are the ones inside the primitive cell  $-1/2 \leq w_l < 1/2$ . Currently, there is no mathematical proof on the convergence of this sorting method but we will show that computing the  $N$  fundamental FFs associated with  $k = 0$  is often more efficient than the eigenvalue sorting method, especially for small fundamental frequency of the periodic state  $\beta$  [62].

Like a vibrational mode for a perturbed equilibrium, the  $N$  computed FFs  $\mathbf{y}_n(\tau)$ , with complex spectrum  $\sum_h (s_n + ih\beta)$ , allow to determine the local stability of a perturbed periodic stationary state. Notably, if it exists a subscript  $g$  for which  $\Re(s_g) > 0$ , the perturbed stationary state increases exponentially in the direction of the  $g^{\text{th}}$  mode  $\mathbf{y}_g(\tau)$  and the stationary state is said to be locally unstable.

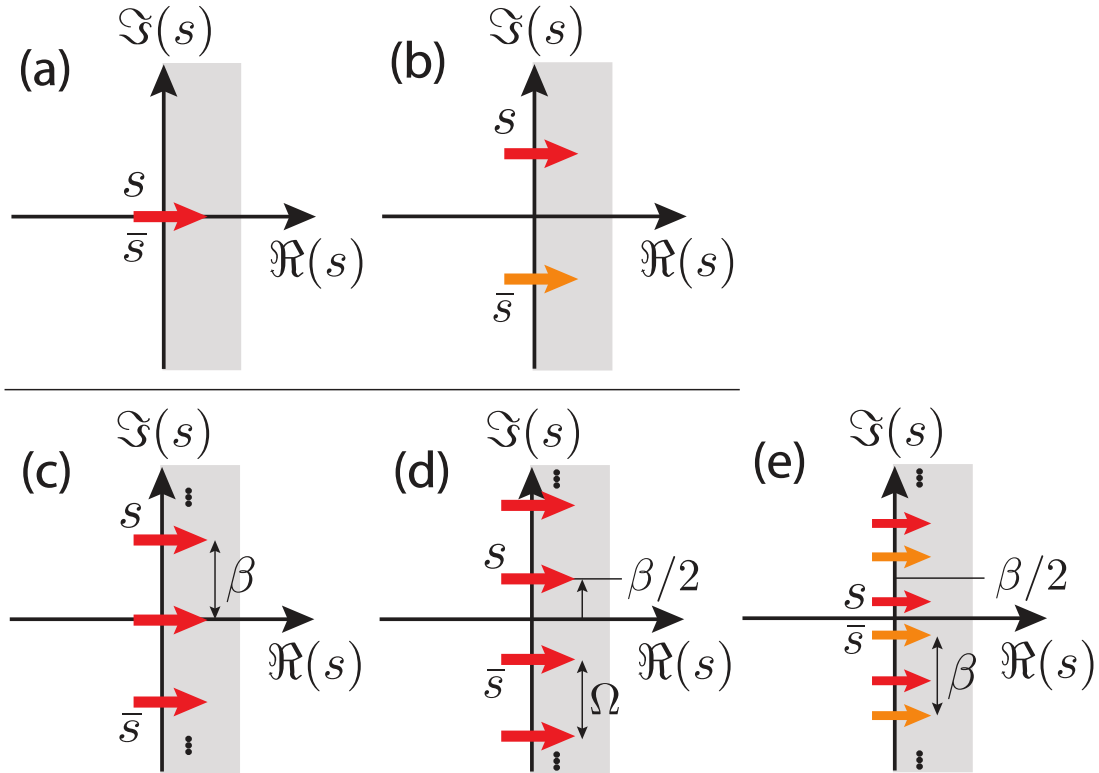


Figure 3.2: Bifurcation and local stability analysis of a periodic stationary state by studying the spectrum of the destabilizing Floquet form in the Argand plane. (a) Static instability leading to a steady-state bifurcation. (b) Dynamical instability responsible for the Hopf bifurcation. (c) Steady bifurcation of a  $T$ -periodic state. (d) Flip or period doubling bifurcation of a periodic state. (e) Secondary Hopf or Neimark-Sacker bifurcation of a periodic state.

By analyzing how the spectrum  $\sum_h (s_g + ih\beta)$  and its complex conjugate in the state space  $\sum_h (\bar{s}_g + ih\beta)$  cross the imaginary axis in the Argand plane, as shown in Fig. 3.2, it is possible to characterize the bifurcation that will undergo the perturbed stationary state. Note that for both algorithms, it is important to exclude one of the limit of the ranges  $-\beta/2 \leq \Im(s_l) < \beta/2$  or  $-1/2 \leq w_l < 1/2$  in order to keep  $N$  eigenvalues or eigenvectors even if the conjugate spectra lock in  $i(\beta/2 \pm m\beta)$  as shown in Fig. 3.2(d).

### 3.3.2 Real Hill Matrix Derivation

There exist some situations where the presence of the pure imaginary number  $i = \sqrt{-1}$  in the complex Hill matrix is a problem. An alternative is to deal with a real Hill matrix. The difference with section 3.3.1 is to expand the time-periodic equation of motion Eq.(3.3),  $\dot{\mathbf{y}}(\tau) = \mathbf{J}(\tau)\mathbf{y}(\tau)$ , in real Fourier series. More details on the derivation of the real Hill matrix and its numerical implementation are found in appendix B.

In the particular case of the Ziegler column with a harmonically modulated elasticity, the  $T$ -periodic Jacobian reads:

$$\mathbf{J}(\tau) = \frac{1}{2}\mathbf{J}_c^0 + \mathbf{J}_c^1 \cos(\beta\tau) \quad (3.18)$$

where the expressions of  $\mathbf{J}_c^0$  and  $\mathbf{J}_c^1$  are given by

$$\mathbf{J}_c^0 = 2 \begin{bmatrix} 0 & 0 & 1 & 0 \\ 0 & 0 & 0 & 1 \\ -\frac{3}{2} & \frac{15}{14} & 0 & 0 \\ 3 & -\frac{33}{14} & 0 & 0 \end{bmatrix} \text{ and } \mathbf{J}_c^1 = 2\lambda \begin{bmatrix} 0 & 0 & 0 & 0 \\ 0 & 0 & 0 & 0 \\ \frac{8}{7} & (\frac{4}{7}\eta - \frac{12}{7}) & 0 & 0 \\ -\frac{12}{7} & (-\frac{20}{7}\eta + \frac{32}{7}) & 0 & 0 \end{bmatrix}. \quad (3.19)$$

The  $N = 4$  Floquet forms  $\mathbf{y}(\tau)$  given in the complex domain in Eq.(3.13) can be expressed by the real expansion:

$$\mathbf{y}(\tau) = \left( \frac{1}{2}\mathbf{a}^0 + \sum_{h=1}^{\infty} [\mathbf{a}^h \cos(h\beta\tau) + \mathbf{b}^h \sin(h\beta\tau)] \right) e^{s\tau}, \quad (3.20)$$

and the associated time derivative reads:

$$\begin{aligned} \dot{\mathbf{y}}(\tau) = & \left( \frac{1}{2}\mathbf{a}^0 s + \sum_{h=1}^{\infty} [(s\mathbf{a}^h + h\beta\mathbf{b}^h) \cos(h\beta\tau) \right. \\ & \left. + (s\mathbf{b}^h - h\beta\mathbf{a}^h) \sin(h\beta\tau)] \right) e^{s\tau}. \end{aligned} \quad (3.21)$$

Replacing the expanded expressions of  $\mathbf{y}(\tau)$ ,  $\dot{\mathbf{y}}(\tau)$  and  $\mathbf{J}(\tau)$  of Eq.(3.18)-(3.21) in Eq.(3.3), we can recast the time-periodic coefficients to the spectral domain:

$$\begin{aligned} \mathbf{0} &= \mathbf{J}(\tau)\mathbf{y}(\tau) - \dot{\mathbf{y}}(\tau), \\ \mathbf{0} &= \sum_{h=1}^{\infty} \left[ \left( \frac{1}{2}\mathbf{J}_c^0 \mathbf{a}^h - s\mathbf{a}^h - h\beta\mathbf{b}^h \right) \cos(h\beta\tau) \right] \\ &+ \sum_{h=1}^{\infty} \left[ \left( \frac{1}{2}\mathbf{J}_c^0 \mathbf{b}^h - s\mathbf{b}^h + h\beta\mathbf{a}^h \right) \sin(h\beta\tau) \right] \\ &\left( \frac{1}{2}\mathbf{J}_c^0 - s \right) \frac{\mathbf{a}^0}{2} + \mathbf{J}_c^1 \left( \frac{\mathbf{a}_0}{2} \cos(\beta\tau) \right. \\ &+ \sum_{h=1}^{\infty} \left[ \frac{\mathbf{a}^h}{2} \left( \cos((1+h)\beta\tau) + \cos((1-h)\beta\tau) \right) \right. \\ &\left. \left. + \frac{\mathbf{b}^h}{2} \left( \sin((1+h)\beta\tau) - \sin((1-h)\beta\tau) \right) \right] \right). \end{aligned} \quad (3.22)$$

Like for Eq.(2.38) and (3.15), the harmonic balance method allows us to recast the problem in  $2H + 1$  algebraic equations of dimension  $N$  by independently equating to zero all the constant terms in  $\cos(0\beta\tau)$ , the first harmonics  $\cos(\beta\tau)$  and  $\sin(\beta\tau)$ , the second harmonics  $\cos(2\beta\tau)$  and  $\sin(2\beta\tau)$  and so on. By putting those equations in a matrix form, we obtain an eigenvalue problem  $(\mathbf{H}^H - s\mathbf{1})\mathbf{q}^H = \mathbf{0}$  where  $\mathbf{H}^H$  is the  $N(2H + 1) \times N(2H + 1)$ -dimensional square real Hill matrix truncated at order  $H$ ,  $s$  and  $\mathbf{q}^H$  are the  $N(2H + 1)$  complex eigenvalues and eigenvectors of  $\mathbf{H}^H$ , respectively. If we order the eigenvector in the form  $\mathbf{q}^H = \left\{ \frac{1}{2}\mathbf{a}^0 \mathbf{a}^1 \dots \mathbf{a}^H \mathbf{b}^1 \dots \mathbf{b}^H \right\}^T$ , the real Hill matrix reads, e.g. for  $\mathbf{H}^3$  and  $\mathbf{q}^3 = \left\{ \frac{1}{2}\mathbf{a}^0 \mathbf{a}^1 \mathbf{a}^2 \mathbf{a}^3 \mathbf{b}^1 \mathbf{b}^2 \mathbf{b}^3 \right\}^T$ :

$$\mathbf{H}^3 = \begin{bmatrix} \frac{1}{2}\mathbf{J}_c^0 & \frac{1}{2}\mathbf{J}_c^1 & \mathbf{0}_4 & \mathbf{0}_4 & \mathbf{0}_4 & \mathbf{0}_4 & \mathbf{0}_4 \\ \mathbf{J}_c^1 & \frac{1}{2}\mathbf{J}_c^0 & \frac{1}{2}\mathbf{J}_c^1 & \mathbf{0}_4 & -\beta\mathbf{1}_4 & \mathbf{0}_4 & \mathbf{0}_4 \\ \mathbf{0}_4 & \frac{1}{2}\mathbf{J}_c^1 & \frac{1}{2}\mathbf{J}_c^0 & \frac{1}{2}\mathbf{J}_c^1 & \mathbf{0}_4 & -2\beta\mathbf{1}_4 & \mathbf{0}_4 \\ \mathbf{0}_4 & \mathbf{0}_4 & \frac{1}{2}\mathbf{J}_c^1 & \frac{1}{2}\mathbf{J}_c^0 & \mathbf{0}_4 & \mathbf{0}_4 & -3\beta\mathbf{1}_4 \\ \mathbf{0}_4 & \beta\mathbf{1}_4 & \mathbf{0}_4 & \mathbf{0}_4 & \frac{1}{2}\mathbf{J}_c^0 & \frac{1}{2}\mathbf{J}_c^1 & \mathbf{0}_4 \\ \mathbf{0}_4 & \mathbf{0}_4 & 2\beta\mathbf{1}_4 & \mathbf{0}_4 & \frac{1}{2}\mathbf{J}_c^1 & \frac{1}{2}\mathbf{J}_c^0 & \frac{1}{2}\mathbf{J}_c^1 \\ \mathbf{0}_4 & \mathbf{0}_4 & \mathbf{0}_4 & 3\beta\mathbf{1}_4 & \mathbf{0}_4 & \frac{1}{2}\mathbf{J}_c^1 & \frac{1}{2}\mathbf{J}_c^0 \end{bmatrix}. \quad (3.23)$$

When replacing the eigenvalues  $s$  and associated eigenvectors  $\mathbf{q}$  of the real Hill matrix in the real Fourier expansion of the fundamental solutions given in Eq.(3.20), one gets a numerical approximation of the FFs of the systems. But like in the complex domain, because of truncation errors, the  $N = 4$  families of  $(2H + 1)$  computed solutions  $\mathbf{y}_n(\tau)$  do not all converge to the FFs and a sorting algorithm is needed. The computed eigenvalues are the same whether it comes from the real or complex Hill matrix. Consequently, the eigenvalue algorithm still holds with the real Hill matrix: by keeping the  $N$  eigenvalues inside the spectral primitive cell  $-\beta/2 \leq \Im(s_l) < \beta/2$ , this sill (with their associated eigenvectors) eventually lead to  $N$  converged FFs as  $H$  is increased.

The eigenvector sorting algorithm that allows to compute the  $N$  fundamental FFs also holds with the real Hill matrix. It still consists in computing the weighted means  $w_l = \sum_h |\mathbf{p}_l^h| / \sum_h |\mathbf{p}_l^h|$  for  $-H \leq h \leq H$  and keeping the spectrum associated with the  $N$  weighted means that belong to the primitive cell  $-1/2 \leq w_l < 1/2$ . The only supplementary step to compute  $w_l$  with the real Hill matrix is that we need the complex/real transformation formulas  $\mathbf{p}^0 = \mathbf{a}^0/2$  for  $h = 0$  and  $\mathbf{p}^{-h} = (\mathbf{a}^h + i\mathbf{b}^h)/2$  or  $\mathbf{p}^h = (\mathbf{a}^h - i\mathbf{b}^h)/2$  for  $h > 0$ .

If instead of a harmonic modulation as in equation (3.18), we consider a general periodic modulation, the  $T$ -periodic Jacobian would read

$$\mathbf{J}(\tau) = \frac{1}{2}\mathbf{J}_c^0 + \sum_{h=1}^{\infty} \left[ \mathbf{J}_c^h \cos(h\beta\tau) + \mathbf{J}_s^h \sin(h\beta\tau) \right]. \quad (3.24)$$

In this situation, the linear equation of motion  $\dot{\mathbf{y}}(\tau) - \mathbf{J}(\tau)\mathbf{y}(\tau) = \mathbf{0}$ , expanded in the real spectral domain, becomes much more complicated. However, the harmonic balance method can still be applied, leading to an eigenvalue problem  $(\mathbf{H}^H - s\mathbf{1})\mathbf{q}^H = \mathbf{0}$ . The expression of the real Hill matrix  $\mathbf{H}^H$  is yet more complicated than the one of Eq.(3.23) in the harmonic modulation case. If decomposed in a sum of block matrices and by ordering

the eigenvector in the form  $\mathbf{q}^H = \left\{ \frac{1}{2} \mathbf{a}^0 \mathbf{a}^1 \dots \mathbf{a}^H \mathbf{b}^1 \dots \mathbf{b}^H \right\}^T$ ,  $\mathbf{H}^H$  reads:

$$\mathbf{H}^H = \begin{bmatrix} \frac{1}{2} \mathbf{J}_c^0 & \frac{1}{2} \mathbf{J}_c & \frac{1}{2} \mathbf{J}_s \\ \mathbf{J}_c^T & \begin{bmatrix} \mathbf{K}_c + \mathbf{T}_c \\ \mathbf{K}_s + \mathbf{T}_s \end{bmatrix} & \begin{bmatrix} \mathbf{K}_s - \mathbf{T}_s \\ \mathbf{T}_c - \mathbf{K}_c \end{bmatrix} \\ \mathbf{J}_s^T & & \end{bmatrix}, \quad (3.25)$$

where

$$\mathbf{J}_c = \left\{ \mathbf{J}_c^1 \mathbf{J}_c^2 \dots \mathbf{J}_c^H \right\} \quad \text{and} \quad \mathbf{J}_s = \left\{ \mathbf{J}_s^1 \mathbf{J}_s^2 \dots \mathbf{J}_s^H \right\}$$

are  $(N \times HN)$ -dimensional block vectors ( $\mathbf{J}_c^T$  and  $\mathbf{J}_s^T$  are the transpose of the above block vectors, not of the full matrices  $\mathbf{J}_c$  and  $\mathbf{J}_s$  meaning one has to be careful to not transpose the matrices  $\mathbf{J}_c^h$  and  $\mathbf{J}_s^h$  in the process but simply ordering them in a column block vector),

$$\mathbf{K}_{c,s} = \frac{1}{2} \begin{bmatrix} \mathbf{J}_{c,s}^2 & \mathbf{J}_{c,s}^3 & \mathbf{J}_{c,s}^4 & \dots & \mathbf{J}_{c,s}^{H+1} \\ \mathbf{J}_{c,s}^3 & \mathbf{J}_{c,s}^4 & \mathbf{J}_{c,s}^5 & \dots & \mathbf{J}_{c,s}^{H+2} \\ \mathbf{J}_{c,s}^4 & \mathbf{J}_{c,s}^5 & \mathbf{J}_{c,s}^6 & \dots & \mathbf{J}_{c,s}^{H+3} \\ \vdots & \vdots & \vdots & \ddots & \vdots \\ \mathbf{J}_{c,s}^{H+1} & \mathbf{J}_{c,s}^{H+2} & \mathbf{J}_{c,s}^{H+3} & \dots & \mathbf{J}_{c,s}^{2H} \end{bmatrix}$$

are  $(NH \times NH)$ -dimensional block matrices with harmonic contributions of the Jacobian either on cosine or sine, and where

$$\mathbf{T}_c = \frac{1}{2} \begin{bmatrix} \mathbf{J}_c^0 & \mathbf{J}_c^1 & \mathbf{J}_c^2 & \dots & \mathbf{J}_c^{H-1} \\ \mathbf{J}_c^1 & \mathbf{J}_c^0 & \mathbf{J}_c^1 & \dots & \mathbf{J}_c^{H-2} \\ \mathbf{J}_c^2 & \mathbf{J}_c^1 & \mathbf{J}_c^0 & \dots & \mathbf{J}_c^{H-3} \\ \vdots & \vdots & \vdots & \ddots & \vdots \\ \mathbf{J}_c^{H-1} & \mathbf{J}_c^{H-2} & \mathbf{J}_c^{H-3} & \dots & \mathbf{J}_c^0 \end{bmatrix}$$

and

$$\mathbf{T}_s = \frac{1}{2} \begin{bmatrix} 2\beta \mathbf{1}_4 & -\mathbf{J}_s^1 & -\mathbf{J}_s^2 & \dots & -\mathbf{J}_s^{H-1} \\ \mathbf{J}_s^1 & 4\beta \mathbf{1}_4 & -\mathbf{J}_s^1 & \dots & -\mathbf{J}_s^{H-2} \\ \mathbf{J}_s^2 & \mathbf{J}_s^1 & 6\beta \mathbf{1}_4 & \dots & -\mathbf{J}_s^{H-3} \\ \vdots & \vdots & \vdots & \ddots & \vdots \\ \mathbf{J}_s^{H-1} & \mathbf{J}_s^{H-2} & \mathbf{J}_s^{H-3} & \dots & 2H\beta \mathbf{1}_4 \end{bmatrix}$$

are  $(NH \times NH)$ -dimensional block matrices. Although seemingly complicated if compared to the general complex Hill matrix given in Eq.(3.16) that is the sum of a complex block diagonal matrix and a real Toeplitz block matrix, the general real Hill matrix is relatively easy to numerically implement. Indeed, it is composed of  $\mathbf{K}_c$  and  $\mathbf{K}_s$  which are Hankel block matrices,  $\mathbf{T}_c$  that is a Toeplitz matrix and  $\mathbf{T}_s$  that is the sum of a real block diagonal matrix and a Toeplitz matrix. Applying the eigenvector sorting algorithm on the real Hill matrix  $\mathbf{H}^H$  of Eq.(3.17) allows to compute the  $N$  fundamental FFs of a system in a general periodic state.

### 3.4 Periodically conservative case ( $\eta = 0$ )

In this section, we analyze the influence of the modulation loading parameters  $\beta$  and  $\lambda$  on the transverse vibrational modes and stability of the Ziegler column under an end com-

pressive horizontal load ( $\eta = 0$ ). We start with the classic case of a constant compressive force, i.e. for  $\beta = 0$  and study the influence of periodicity when  $\beta \neq 0$  on the harmonic modes and stability. We finish with some remarks on the particular limit  $\beta \rightarrow 0$ .

### 3.4.1 Constant elastic state ( $\beta = 0$ )

When  $\beta = 0$ , the applied compressive dimensionless load  $P(\tau) = \lambda \cos(\beta\tau)$  is constant in time and the Hill matrix of Eq.(3.17) truncated to the order  $H = 2$  becomes

$$\mathbf{H}^2 = \begin{bmatrix} \mathbf{J}^0 & \mathbf{0}_4 & \mathbf{0}_4 & \mathbf{0}_4 & \mathbf{0}_4 \\ \mathbf{0}_4 & \mathbf{J}^0 & \mathbf{0}_4 & \mathbf{0}_4 & \mathbf{0}_4 \\ \mathbf{0}_4 & \mathbf{0}_4 & \mathbf{J}^0 & \mathbf{0}_4 & \mathbf{0}_4 \\ \mathbf{0}_4 & \mathbf{0}_4 & \mathbf{0}_4 & \mathbf{J}^0 & \mathbf{0}_4 \\ \mathbf{0}_4 & \mathbf{0}_4 & \mathbf{0}_4 & \mathbf{0}_4 & \mathbf{J}^0 \end{bmatrix}, \quad (3.26)$$

with

$$\mathbf{J}^0 = \begin{bmatrix} 0 & 0 & 1 & 0 \\ 0 & 0 & 0 & 1 \\ -\frac{3}{2} & \frac{15}{14} & 0 & 0 \\ 3 & -\frac{33}{14} & 0 & 0 \end{bmatrix} + \lambda \begin{bmatrix} 0 & 0 & 0 & 0 \\ 0 & 0 & 0 & 0 \\ \frac{8}{7} & -\frac{12}{7} & 0 & 0 \\ -\frac{12}{7} & \frac{32}{7} & 0 & 0 \end{bmatrix}.$$

From Eq.(3.26) we see that the lines and rows of the truncated Hill matrix of Eq.(3.16) are independent, whatever the truncation order  $H$ . If  $H = 0$ , no spectral sorting is needed as the Hill matrix reduces to its central block  $\mathbf{J}^0$  whose spectrum gives  $N = 4$  eigenvalues and eigenvectors that correspond to the  $N$  classic harmonic modes  $\mathbf{y}_n(\tau) = \mathbf{p}_n^0 e^{s_n \tau}$  when replaced in Eq.(3.13). If  $H > 0$ , the Hill matrix leads to  $(2H + 1)$  identical families of  $N$  independent eigenvalues and eigenvectors of  $\mathbf{J}^0$ . Applying the eigenvector sorting method would give the  $N$  correct harmonic modes but the eigenvalue sorting algorithm will return an empty spectrum as the computed eigenvalues will never be in the spectral primitive cell  $-\beta/2 \leq \Im(s_i) < \beta/2$  since  $\beta = 0$ . Thus, only the eigenvector sorting algorithm convey the notion that classic normal modes are particular cases of fundamental FFs.

Fig. 3.3 is the classical dynamical vision of buckling. It shows the evolution of the computed spectrum of the  $N = 4$  harmonic FFs as a function of dimensionless compressive load  $\lambda/\lambda_b$  where  $\lambda_b$  is the already mentioned buckling load. At  $\lambda = 0$ , the bi-articulated beam has two classic harmonic vibrational modes in the physical space: one with natural frequency  $\omega_1$  where the linearized angles  $\theta_1(\tau)$  and  $\theta_2(\tau)$  vibrates in phase; one with natural frequency  $\omega_2$  where  $\theta_1(\tau)$  and  $\theta_2(\tau)$  are out-of-phase. The time evolutions of the linearized angles  $\theta_1(\tau)$  and  $\theta_2(\tau)$  of those two modes are shown in the insets of Fig. 3.3(b). The dash-dotted lines represent the constant amplitude of the eigenfunction modulus  $|\mathbf{p}_n^0|$  whose value is undefined, unless normalized. The free vibratory response of the bi-articulated beam, solution of Eq.(3.3) with the Jacobian  $\mathbf{J}(\tau)$  given in Eq.(3.26), can be written as a linear superposition of these two normal modes. As the compressive load  $\lambda$  is increased, the frequencies of the two fundamental FFs decrease until the smallest one eventually goes to zero at  $\lambda = \lambda_b$ . The lock-in of the conjugate spectrum  $s_1$  and  $\bar{s}_1$  on the real axis induces a positive growth rate  $\Re(s_1) > 0$  and therefore a bifurcation of the trivial spatial straight state of the Ziegler column along the in-phase static mode. This local instability is the one shown in Fig. 3.2(a) and is responsible for the nonlinear

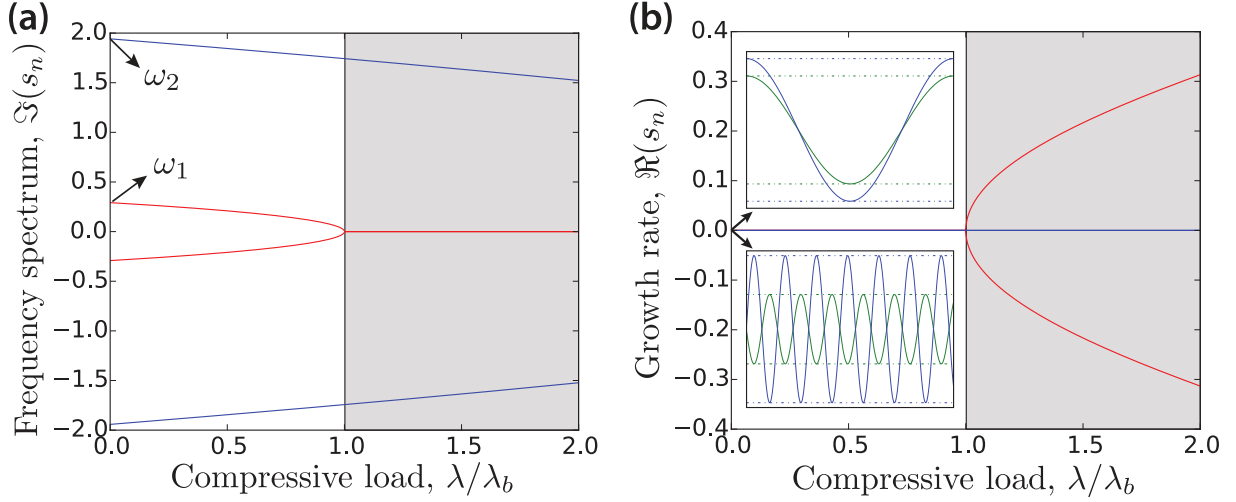


Figure 3.3: Evolution of the spectrum of the two Floquet forms (or classic harmonic modes) as a function of loading parameter  $\lambda$  for  $\eta = 0$  and  $\beta = 0$ . (a) Evolution of the natural frequencies of the bi-articulated bar in compression. (b) Evolution of the growth rate of the two modes. The grey regions in (a) and (b) indicate that the trivial state  $\theta_1^0(\tau) = \theta_2^0(\tau) = 0$  is locally unstable. Insets: Top and bottom respectively show, for  $\lambda = 0$ , the angles  $\theta_1(\tau)$  and  $\theta_2(\tau)$  of the in-phase and out-of-phase classic modes with natural frequency  $\omega_1$  and  $\omega_2$ , respectively. The dashed-dotted lines represent the moduli of the complex eigenfunctions  $|p_n^0|$  and  $-|p_n^0|$  that envelope the motion.

response shown in Fig. 2.2(a). Note that in this case, the two FFs are uncoupled in the physical space as highlighted in Fig. 3.3 by the fact that the two color lines never combine.

### 3.4.2 Periodic elastic state ( $\beta \neq 0$ )

When  $\beta \neq 0$ , the straight bi-articulated bar is in a periodic elastic state as the Jacobian  $\mathbf{J}(\tau)$  of Eq.(3.3) is  $T$ -periodic with  $T = 2\pi/\beta$ . In the particular conservative case where  $\eta = 0$ , the Hill matrix of Eq.(3.17), truncated to the order  $H = 2$ , becomes

$$\mathbf{H}^2 = \begin{bmatrix} \mathbf{J}^0 + i2\beta\mathbf{1}_4 & \mathbf{J}^1 & \mathbf{0}_4 & \mathbf{0}_4 & \mathbf{0}_4 \\ \mathbf{J}^1 & \mathbf{J}^0 + i\beta\mathbf{1}_4 & \mathbf{J}^1 & \mathbf{0}_4 & \mathbf{0}_4 \\ \mathbf{0}_4 & \mathbf{J}^1 & \mathbf{J}^0 & \mathbf{J}^1 & \mathbf{0}_4 \\ \mathbf{0}_4 & \mathbf{0}_4 & \mathbf{J}^1 & \mathbf{J}^0 - i\beta\mathbf{1}_4 & \mathbf{J}^1 \\ \mathbf{0}_4 & \mathbf{0}_4 & \mathbf{0}_4 & \mathbf{J}^1 & \mathbf{J}^0 - i2\beta\mathbf{1}_4 \end{bmatrix}, \quad (3.27)$$

with

$$\mathbf{J}^0 = \begin{bmatrix} 0 & 0 & 1 & 0 \\ 0 & 0 & 0 & 1 \\ -\frac{3}{2} & \frac{15}{14} & 0 & 0 \\ 3 & -\frac{33}{14} & 0 & 0 \end{bmatrix} \quad \text{and} \quad \mathbf{J}^1 = \lambda \begin{bmatrix} 0 & 0 & 0 & 0 \\ 0 & 0 & 0 & 0 \\ \frac{8}{7} & -\frac{12}{7} & 0 & 0 \\ -\frac{12}{7} & \frac{32}{7} & 0 & 0 \end{bmatrix}.$$

Unlike in Eq.(3.26), the lines and rows of the truncated  $\mathbf{H}^H$  of Eq.(3.27) are now fully coupled via the harmonic contribution of the Jacobian  $\mathbf{J}^1$  and the sorting of the spectrum of Hill's matrix given in Eq.(3.27) is a necessity to compute the  $N = 4$  FFs in the state space.

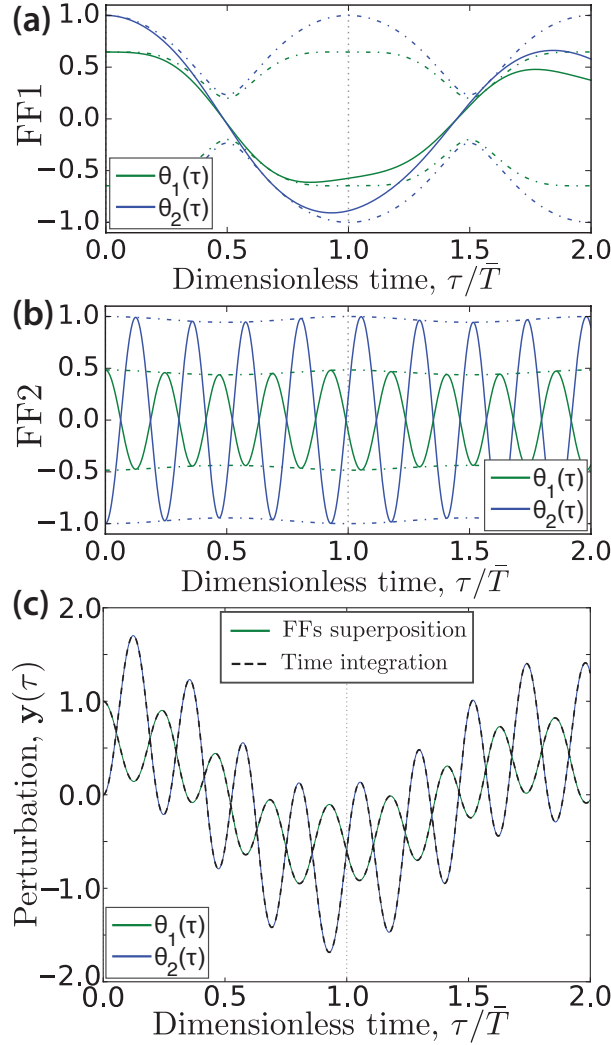


Figure 3.4: Vibratory response for  $\eta = 0$ ,  $\beta = 1.55\omega_1$ ,  $\lambda = 0.75\lambda_b$  and  $H = 3$ . (a) Time evolution of the angles  $\theta_1(\tau)$  and  $\theta_2(\tau)$  of the first fundamental Floquet form  $\mathbf{y}_1(\tau) = \mathbf{p}_1(\tau)e^{s_1\tau}$  over the first two periods  $2T$  where  $T = 2\pi/\beta$ . The dash-dotted lines show the moduli of the periodic eigenfunctions  $|\mathbf{p}_n(\tau)|$  and  $-|\mathbf{p}_n(\tau)|$  that envelope the almost periodic motions. (b) Same as (a) but for the second fundamental Floquet form. (c) Time evolution of the angles  $\theta_1(\tau)$  and  $\theta_2(\tau)$  of the free vibratory response  $\mathbf{y}(\tau)$  of Eq.(3.3) for the initial conditions  $\theta_1(0) = 1$  and  $\theta_2(0) = \dot{\theta}_1(0) = \dot{\theta}_2(0) = 0$ . The response has been computed either with a classic direct iterative ODE solver (dashed line) or by recombining the FFs (full line).

Figs. 3.4(a),(b) show the two fundamental FFs,  $\mathbf{y}_n(\tau) = \mathbf{p}_n(\tau)e^{s_n\tau}$ , computed with the eigenvector sorting algorithm, about the trivial spatial state  $\theta_1^0(\tau) = \theta_2^0(\tau) = 0$  for  $\eta = 0$ ,  $\beta = 1.55\omega_1$ ,  $\lambda = 0.75\lambda_b$  and  $H = 3$ . Those two typical physical FFs are the periodically modulated generalization of the classic harmonic modes shown in the insets of Fig. 3.5(b). Notably, the first FF of Fig. 3.4(a) almost-periodically vibrates with a  $\theta_1(\tau)$  and  $\theta_2(\tau)$  in phase and a fundamental frequency close to  $\omega_1$  when the second FF in Fig. 3.4(b) vibrates out-of-phase with a fundamental frequency close to  $\omega_2$ . Unlike classic harmonic modes, the modulus of the eigenfunction  $\mathbf{p}(\tau)$ , whose value is undefined unless normalized, is not constant but  $T$ -periodic as illustrated by the dashed-dotted lines in Figs. 3.4(a),(b). Like for  $\beta = 0$ , the moduli  $|\mathbf{p}(\tau)|$  and  $-|\mathbf{p}(\tau)|$  envelope the almost-periodic motion. The superposition property of FFs given in Eq.(3.1) is highlighted in

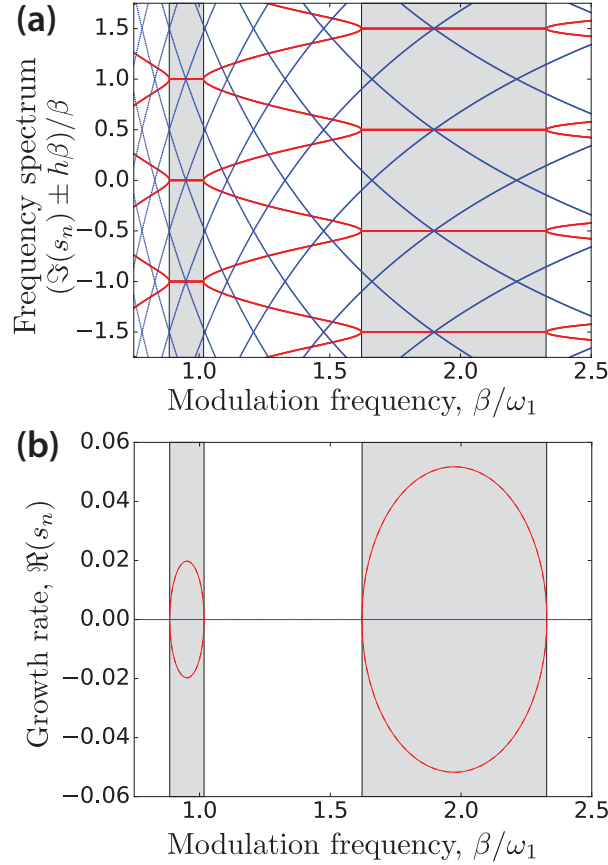


Figure 3.5: Evolution of the spectrum of the  $N = 4$  fundamental FFs as a function of  $\beta/\omega_1$  for  $\eta = 0$ ,  $\lambda = 0.75\lambda_b$  and  $H = 25$ . (a) Evolution of the frequency spectrum location of the FFs,  $\Im(s_n) + \sum_h ih\beta$ . (b) Evolution of the growth rate of the FFs,  $\Re(s_n)$ . The grey regions in (a) and (b) indicate that the straight bi-articulated bar is unstable.

Fig. 3.4(c) where we show the free vibratory response of the straight bi-articulated bar computed either through FFs or classic ODE time integrator. The perturbation  $\mathbf{y}(\tau)$ , solution of Eq.(3.3), can be decomposed in the normal basis of its FFs which notably means it would have been possible to find a set of initial conditions for which only one FF contributes to the solution  $\mathbf{y}(\tau)$  (e.g. in Fig. 3.4 for  $\theta_1(0) = 0.646$ ,  $\theta_2(0) = 1$  and  $\dot{\theta}_1(0) = \dot{\theta}_2(0) = 0$ , only the first FF would contribute to the linear response and Fig. 3.4(c) would have been identical to Fig. 3.4(a)).

Fig. 3.5 shows the evolution of the  $N = 4$  spectra  $s_n + \sum_h ih\beta$  of the computed fundamental FFs as a function of  $\beta/\omega_1$  for  $\lambda = 0.75\lambda_b$  and  $H = 25$  (to ensure convergence). The fundamental frequencies  $\Im(s_n)$ , and moreover the frequency spectra  $\Im(s_n) + \sum_h ih\beta$ , vary with the modulation parameters of the elastic state  $\lambda$  and  $\beta$ . Also, since the system is conservative, the two FFs are uncoupled in the physical space as highlighted in Fig. 3.5 by the independence between the red and blue modal colors. Furthermore, like the classic harmonic modes of Fig. 3.5, there exists some modulation parameters for which the straight bi-articulated bar becomes unstable, i.e. the spectrum of the in-phase FF  $\Im(s_n) + \sum_h ih\beta$  lock in the state space with its conjugate leading to a positive associated growth rate  $\Re(s_n)$  (we do not see here the lock-in of the out-of-phase FF in Fig. 3.5 because the latter happens at higher modulation frequency than the displayed one). As illustrated in Figs. 3.2(c),(d) and displayed in Fig. 3.5(a), FFs have a poly-harmonic

spectrum  $\Im(s_n) + \sum_h ih\beta$  and can lock either in  $i(\beta \pm m\beta)$  or in  $i(\beta/2 \pm m\beta)$ . These two phenomena respectively correspond to a  $T$  and  $2T$ -periodic FF that diverges exponentially and is responsible for the steady and flip bifurcation shown for example in Fig. 2.2(b). The principal region of instability, i.e. the one with the largest  $\beta$  range, corresponds to a lock-in of the fundamental frequency of a FF when secondary regions are related to lock-in of subharmonics.

Fig. 3.6(a) displays the stability chart of the straight bi-articulated bar with an end compressive horizontal force in the modulation parameters space  $(\lambda, \beta)$ . For each parameters, we chose a truncation order  $H$  so that the maximum difference  $\delta$  between the  $N = 4$  Floquet multipliers computed with the eigenvector sorting method and the ones obtained from a converged monodromy matrix algorithm [11] is  $\delta = 1 \times 10^{-6}$ . The resulting minimal truncation order map,  $H$ , as a function of  $(\lambda, \beta)$  to ensure convergence is displayed in Fig. 3.13(a). Colored regions, or Mathieu tongues, that theoretically

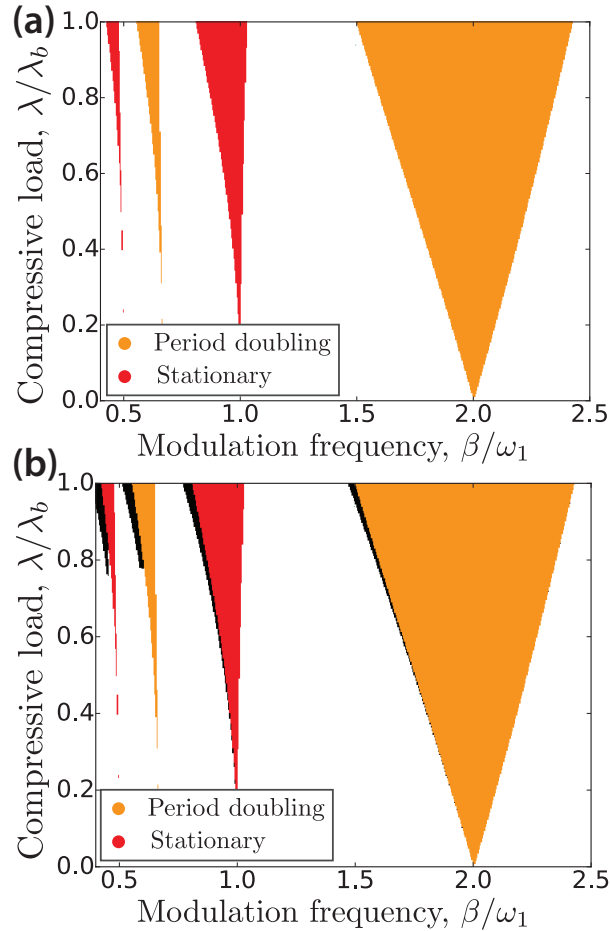


Figure 3.6: Stability chart of the conservative system in the  $(\lambda, \beta)$  space for  $\eta = 0$ ,  $\beta \neq 0$  and a variable converged truncation order  $H$  given in Fig. 3.13(a). (a)  $T$  (red) and  $2T$ -instability (orange) regions computed through the eigenvector or eigenvalue sorting algorithms. (b) Same stability chart but by analyzing all the spectrum of the Hill matrix, i.e. with no sorting of the eigenvectors or eigenvalues. The black color show supplementary instability regions which are spurious numerical results due to the truncation of the Hill matrix that would happen whatever  $H$ . The stability is computed on a  $500 \times 500$  grid in the  $(\beta, \lambda)$  modulation parameter space and colors are plotted according to the closest data point.

originate at  $2\beta/m\omega_1$  for  $\lambda \rightarrow 0$  with  $m$  a positive integer, correspond to parameters for which at least one of the growth rate  $\Re(s_n)$  of the 4 FFs is positive. Red regions are  $T$ -instability domains associated with lock of the frequency spectrum of the in-phase FF in  $\beta \pm m\beta$  when orange regions show  $2T$ -instability zones related to a  $\beta/2 \pm m\beta$  lock-in of the in-phase FF as shown in Fig. 3.5. In the particular conservative case  $\eta = 0$  and for the same truncation order map of  $H$  given in Fig. 3.13(a), the use of the eigenvalue sorting algorithm lead to the exact same stability chart displayed in Fig. 3.6(a). Indeed, we observe the eigenvector sorting method gives the  $N = 4$  Floquet exponents  $s_n$  that are in the primitive spectral cell  $-\beta/2 \leq s_n < \beta/2$  when in  $T$  or  $2T$ -periodic instability regions. Fig. 3.6(b) shows the stability chart but by using no sorting algorithms, i.e. by analyzing all the eigenvalues  $s_l$  of the Hill matrix to see whether  $\Re(s_l) > 0$ . The differences between both stability charts are highlighted in black. Whatever the truncation order  $H$ ,

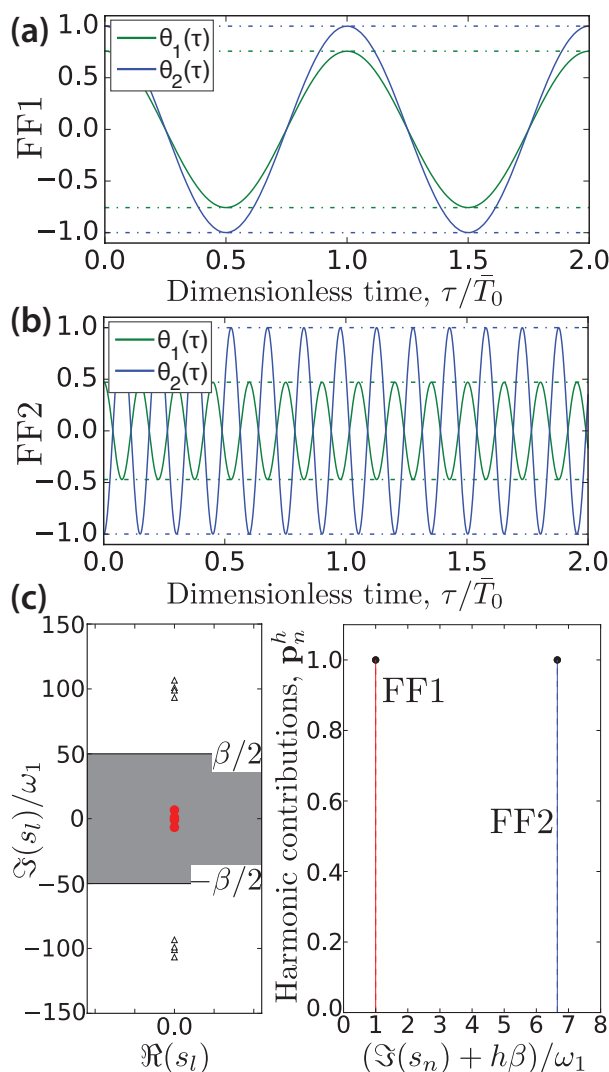


Figure 3.7: Fundamental FFs for  $\eta = 0$ ,  $\beta = 100\omega_1$ ,  $\lambda = 0.75\lambda_b$  and  $H = 1$ . (a) Time evolution of the angles  $\theta_1(\tau)$  and  $\theta_2(\tau)$  of FF1 over the first two natural periods  $2\bar{T}_0$  where  $\bar{T}_0 = 2\pi/\omega_1$ . The dash-dotted lines show the moduli of the periodic eigenfunctions  $|\mathbf{p}_n(\tau)|$  and  $-|\mathbf{p}_n(\tau)|$  that envelope the almost periodic motion. (b) Same as (a) but for FF2. (c) (left) Raw spectrum of the truncated Hill matrix. The  $N = 4$  fundamental Floquet exponents computed by eigenvector sorting are shown with red circles. The region  $-\beta/2 \leq \Im(s_l) < \beta/2$  for eigenvalue sorting is shown in grey. (right) FFT of the two quasi-harmonic FFs.

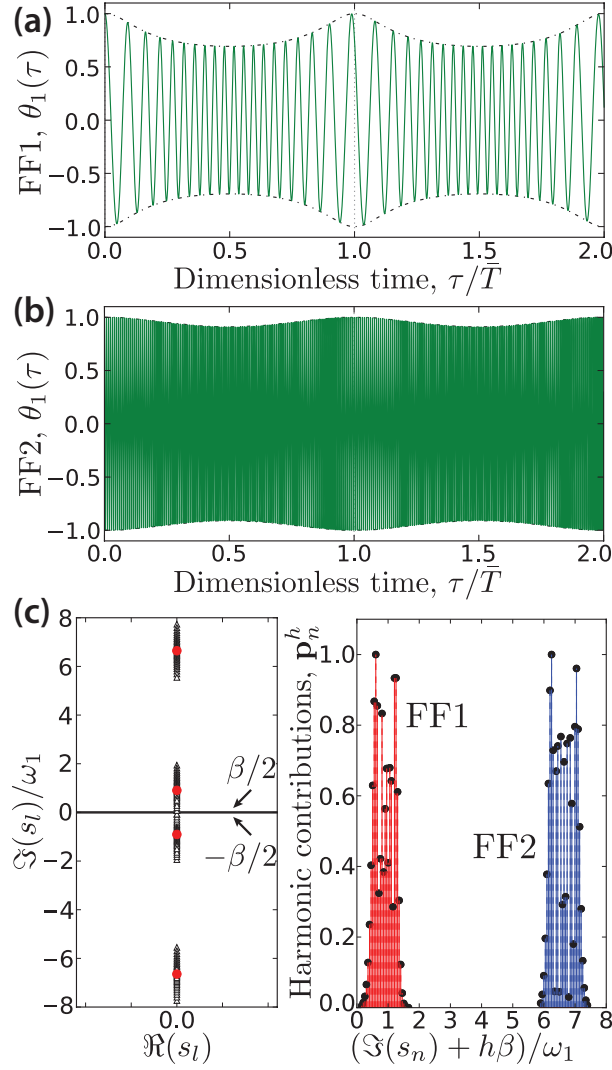


Figure 3.8: Fundamental FFs for  $\eta = 0$ ,  $\beta = 0.05\omega_1$ ,  $\lambda = 0.75\lambda_b$  and  $H = 15$ . (a) Time evolution of the angle  $\theta_1(\tau)$  of FF1 over the first two periods  $2T$  where  $T = 2\pi/\beta$  with their envelopes  $|\mathbf{p}_n(\tau)|$  and  $-|\mathbf{p}_n(\tau)|$ . (b) Same as (a) but for FF2. (c) (left) Raw spectrum of the truncated Hill matrix. The  $N = 4$  fundamental Floquet exponents computed by eigenvector sorting are shown with red circles. The region  $-\beta/2 \leq \Im(s_i) < \beta/2$  for eigenvalue sorting is shown in grey. (right) FFT of the two FFs.

the truncated Hill matrix will always give some spurious eigenvalues that are inherent to the harmonic balance method. Those spurious eigenvalues are more visible for high  $\lambda$  and close to the instability regions.

### 3.4.3 Asymptotic cases ( $\beta \rightarrow +\infty$ ) and ( $\beta \rightarrow 0$ )

In the asymptotic cases where  $\beta \rightarrow +\infty$  or  $\beta \rightarrow 0$ , i.e. in the situations where the modulation time scale is far from the natural time scale of the system given here by  $\omega_1$  and  $\omega_2$ , several qualitative and quantitative comments can be made about the FFs.

Fig. 3.7 illustrates the  $\beta \rightarrow +\infty$  scenario by showing the two fundamental FFs of

the straight bi-articulated bar in periodic elastic state for  $\eta = 0$ ,  $\lambda = 0.75\lambda_b$  and  $\beta = 100\omega_1$ . The time evolution of the two angles  $\theta_1(\tau)$  and  $\theta_2(\tau)$  of the two FFs are shown in Figs. 3.7(a) and (b). For high modulation frequencies, the harmonic contribution of the compressive force is averaged out and the bi-articulated elastic bar behaves like a classic effective oscillator. The two FFs asymptotically tend to the two classic in-phase and out-of-phase modes of the system with natural frequencies  $\omega_1$  and  $\omega_2$ . Notably, the  $T$ -periodic envelopes of the almost-periodic FFs,  $|\mathbf{p}(\tau)|$  and  $-|\mathbf{p}(\tau)|$ , appear constant over the natural period  $T_0$  since the small oscillations over  $T$  are negligible. Fig. 3.7(c) displays the raw spectrum of the Hill matrix (left) as well as the reconstructed spectrum of the FFs (right). In the  $\beta \rightarrow +\infty$  case, the FFs tend to classic harmonic modes with a spectrum composed of a single oscillation frequency. This spectrum is easily recovered with both eigenvector and eigenvalue sorting algorithms. Actually, both methods lead to the same eigenvalue output as the  $N = 4$  fundamental Floquet exponents obtained with the eigenvector sorting algorithm and represented by red circle in Fig. 3.7(c), are the one inside the  $-\beta/2 \leq \Im(s_l) < \beta/2$ .

Fig. 3.8 illustrates the  $\beta \rightarrow 0$  situation by showing the two in-phase and out-of-phase FFs of Fig. 3.7, but for a very small modulation frequency  $\beta = 0.05\omega_1$ . The time evolution of the angle  $\theta_1(\tau)$  of the two FFs are shown in Figs. 3.8(a) and (b) ( $\theta_2(\tau)$  is not displayed for a sake of clarity). For slow modulation frequency, the end compressive load quasi-statically takes all the amplitudes between the minimum  $\lambda = -0.75\lambda_b$  and maximum  $+0.75\lambda_b$ . As a consequence, the elasticity of our system is quasi-statically modulated and the transverse natural frequencies of the straight bi-articulated bar appear to almost continuously vary (with a small step  $\beta$ ) around  $\omega_1$  and  $\omega_2$ . We can see on Figs. 3.8(a) and (b) that the motion is modulated in frequency and amplitude. The FFTs of the two FFs are displayed on the right side of Fig. 3.8(c) and show two broad spectrum in the vicinity of  $\omega_1$  and  $\omega_2$  whose almost continuous width depend on the modulation amplitude  $\lambda$ . For small  $\beta$ , many frequencies are contained in the FFs and a high truncation order  $H$  is needed for the spectrum of Hill's matrix to converge. The raw spectrum of Hill matrix is shown on the left of Fig. 3.8(c) for  $H = 15$ . It is separated in four distinct packets, centered around  $\omega_1$ ,  $\omega_2$ ,  $-\omega_1$  and  $-\omega_2$ , that correspond to  $N = 4$  families of eigenvalues  $s_{n+k} = s_n + ik\beta$  where  $-H \leq k \leq +H$  (apart from the edges of the packets where the computed eigenvalues are spurious due to truncation errors). The eigenvector sorting algorithm finds the  $N = 4$  fundamental Floquet exponents, highlighted by red circles, that correspond to the most converged eigenvalues (center of the packets). Because of the small modulation frequency  $\beta$ , the eigenvalue sorting algorithm is far from being converged for  $H = 15$  as only two, yet not converged, eigenvalues relative to the first FFs are located in the  $-\beta/2 \leq \Im(s_l) < \beta/2$  region. For the two eigenvalues associated with the spectrum packet around  $\omega_2$  and  $-\omega_2$  to enter that region, more than  $H = 100$  would be needed. In the limit situation  $\beta \rightarrow 0$ , the eigenvalue sorting algorithm is not adapted to efficiently compute the FFs and their spectrum, on the contrary to the eigenvector sorting method that computes the most converged fundamental Floquet exponents and FFs whatever  $\beta$ . In the non-conservative case studied in next section, the same kind of convergence issue will happen in the determination of instability regions associated with Neimark-Sacker bifurcation when using the eigenvalue sorting algorithm.

Note that Fig. 3.8 illustrates a theoretical and physical paradox that the case  $\beta \rightarrow 0$  diverges from  $\beta = 0$ : the undamped vibrational mode of a quasi-statically varying elastic

state is completely different from the mode of vibration of a static elastic state.

### 3.5 Non-Conservative case ( $\eta = 1$ )

In this section, we analyze the influence of the modulation loading parameters  $\beta$  and  $\lambda$  on the transverse vibrational modes of the Ziegler column under a non-conservative end positional loading ( $\eta = 1$ ). We start with the classic case of a constant compressive force, i.e. for  $\beta = 0$ , and study the influence of periodicity when  $\beta \neq 0$  on the modes and stability.

#### 3.5.1 Constant elastic state ( $\beta = 0$ )

In the particular case  $\beta = 0$ , the applied compressive dimensionless load  $P(\tau) = \lambda \cos(\beta\tau)$  and therefore the periodically time-varying Jacobian  $\mathbf{J}(\tau)$  of Eq.(3.3) are independent of time. The Hill matrix of Eq.(3.17) truncated to the order  $H$  reduces to a block diagonal

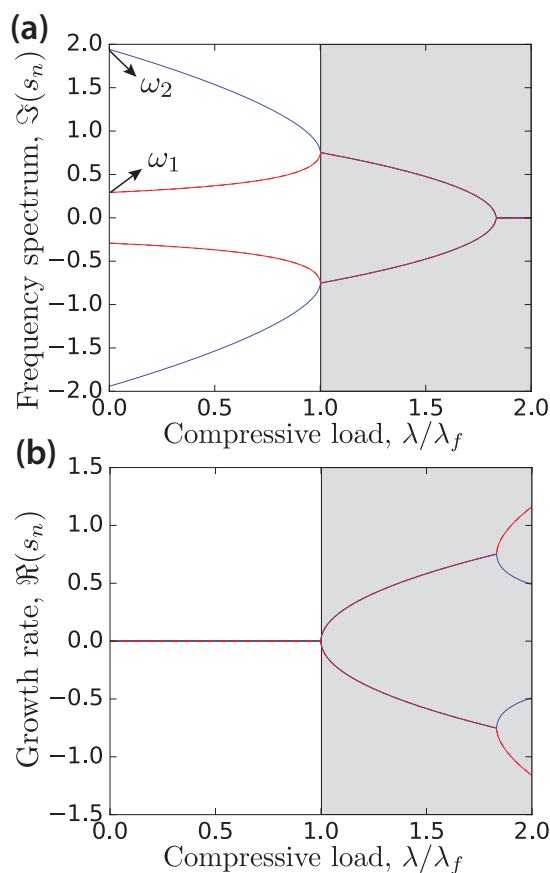


Figure 3.9: Evolution of the spectrum of the two Floquet forms (or classic harmonic modes) as a function of loading parameter  $\lambda$  for  $\eta = 1$  and  $\beta = 0$ . (a) Evolution of the natural frequencies of the bi-articulated bar in compression. (b) Evolution of the growth rate of the two modes. The grey regions in (a) and (b) indicate that the trivial state  $\theta_1^0(\tau) = \theta_2^0(\tau) = 0$  is locally unstable.

matrix with only the fundamental part of the Jacobian  $\mathbf{J}^0$  as shown in Eq.(3.26). In this section, since  $\eta = 1$ , the Jacobian  $\mathbf{J}^0$  reads,

$$\mathbf{J}^0 = \begin{bmatrix} 0 & 0 & 1 & 0 \\ 0 & 0 & 0 & 1 \\ -\frac{3}{2} & \frac{15}{14} & 0 & 0 \\ 3 & -\frac{33}{14} & 0 & 0 \end{bmatrix} + \lambda \begin{bmatrix} 0 & 0 & 0 & 0 \\ 0 & 0 & 0 & 0 \\ \frac{8}{7} & -\frac{5}{7} & 0 & 0 \\ -\frac{12}{7} & \frac{12}{7} & 0 & 0 \end{bmatrix}. \quad (3.28)$$

We can infer from the shape of the Jacobian in Eq.(3.28) that the problem is now non-conservative as the bottom left  $2 \times 2$  block matrix of  $\mathbf{J}^0$  depending on  $\lambda$  is non symmetric. Whether we compute the whole spectrum of  $\mathbf{J}^0$ , i.e. the truncated Hill matrix for  $H = 0$ , or we use the eigenvector sorting algorithm for  $H > 0$  (like in the conservative case, the eigenvalue sorting algorithm can not be used for  $\beta = 0$ ), one numerically approximates  $N = 4$  FFs for a given modulation parameter  $\lambda$ .

Fig. 3.9 shows the plot of the evolution of the computed spectrum of the  $N = 4$  fundamental FFs as a function of dimensionless compressive load  $\lambda/\lambda_f$  where  $\lambda_f$  is the already mentioned flutter load. At  $\lambda = 0$ , the unloaded straight bi-articulated bar has two classic in-phase and out-of-phase vibrational modes with natural frequency  $\omega_1$  and  $\omega_2$ , respectively. Unlike the conservative case, the two harmonic FFs are coupled for  $\eta = 1$  and influence each other so that their spectra eventually lock-in. As the compressive load  $\lambda$  grows, the frequency of the in-phase mode increases when the one of the out-of-phase mode decreases. At  $\lambda = \lambda_f$ , the spectra of the two physical FFs lock in a finite  $\Im(s_n) > 0$ , inducing a positive growth rate  $\Re(s_n)$  of the resulting locked mode (for  $\lambda > \lambda_f$ , only one in-phase mode subsists in the physical space which separates in an unstable and stable one in the state space). This destabilization mechanism corresponds to the flutter instability case shown in Fig. 3.2(b) that is responsible for the Hopf bifurcation illustrated in Fig. 2.2(c). Increasing  $\lambda$  further, the spectra of the remaining FF lock again, this time in the state space and on  $\Im(s_n) = 0$ . This second situation is qualitatively similar to the instability by divergence shown in Fig. 3.3 and Fig. 3.2(a) for the conservative case. The flutter instability only happens on a range of loading parameter  $\lambda$  and evolves toward a divergence instability for sufficiently high compressive loads.

### 3.5.2 Periodic elastic state ( $\beta \neq 0$ )

When  $\beta \neq 0$ , the straight Ziegler column is in a periodic elastic state and its perturbed motion is governed by  $\dot{\mathbf{y}}(\tau) = \mathbf{J}(\tau)\mathbf{y}(\tau)$  Eq.(3.3) with a  $T$ -periodic Jacobian  $\mathbf{J}(\tau)$  where  $T = 2\pi/\beta$ . The truncated matrix has therefore the shape of a tridiagonal matrix by block as shown in Eq.(3.27) but since  $\eta = 1$  in this section, the fundamental and first harmonic contributions of  $\mathbf{J}(\tau)$  now reads

$$\mathbf{J}^0 = \begin{bmatrix} 0 & 0 & 1 & 0 \\ 0 & 0 & 0 & 1 \\ -\frac{3}{2} & \frac{15}{14} & 0 & 0 \\ 3 & -\frac{33}{14} & 0 & 0 \end{bmatrix} \text{ and } \mathbf{J}^1 = \lambda \begin{bmatrix} 0 & 0 & 0 & 0 \\ 0 & 0 & 0 & 0 \\ \frac{8}{7} & -\frac{5}{7} & 0 & 0 \\ -\frac{12}{7} & \frac{12}{7} & 0 & 0 \end{bmatrix}. \quad (3.29)$$

We use the eigenvector sorting algorithm on the spectrum of the truncated Hill matrix with  $\mathbf{J}^0$  and  $\mathbf{J}^1$  given in Eq.(3.29) to compute the  $N = 4$  FFs of the straight Ziegler column under a given end following compressive load  $P(\tau) = \lambda \cos(\beta\tau)$ .

Figs. 3.10(a),(b) display the perturbed angles  $\theta_1(\tau)$  and  $\theta_2(\tau)$  of two fundamental FFs, in the form  $\mathbf{y}_n(\tau) = \mathbf{p}_n(\tau)e^{s_n\tau}$ , about the trivial spatial state  $\theta_1^0(\tau) = \theta_2^0(\tau) = 0$  for  $\eta = 1$ ,  $\beta = 1.55\omega_1$ ,  $\lambda = 0.75\lambda_f$  and  $H = 5$ . Like in the conservative case  $\eta = 0$  illustrated in Fig. 3.4, the FFs are the almost-periodic generalization of the classic harmonic modes shown in the insets of Fig. 3.9(b). For  $\beta \neq 0$ , the eigenfunction  $\mathbf{p}_n(\tau)$  are periodic and the moduli  $|\mathbf{p}_n(\tau)|$  and  $-|\mathbf{p}_n(\tau)|$  envelope the oscillation. In the non conservative case with  $\eta = 1$ , the following end compressive force modulates both FFs as illustrated in Fig. 3.10(a),(b) where the amplitude modulation of the periodic  $|\mathbf{p}_1(\tau)|$  and  $|\mathbf{p}_2(\tau)|$  are of similar intensity. The superposition property of the normal forms still holds in the non conservative case and is highlighted in Fig. 3.10(c). For a given set of initial condition, the perturbation  $\mathbf{y}(\tau)$  solution of (3.3) computed with a classic direct time ODE solver is in perfect agreement with the solution recombined from FFs with  $\mathbf{y}(\tau) = \sum_n \mathbf{p}_n(t)e^{s_n t}$  3.13.

Fig. 3.11 shows the evolution of the  $N = 4$  spectra  $s_n + \sum_h ih\beta$  of the computed FFs

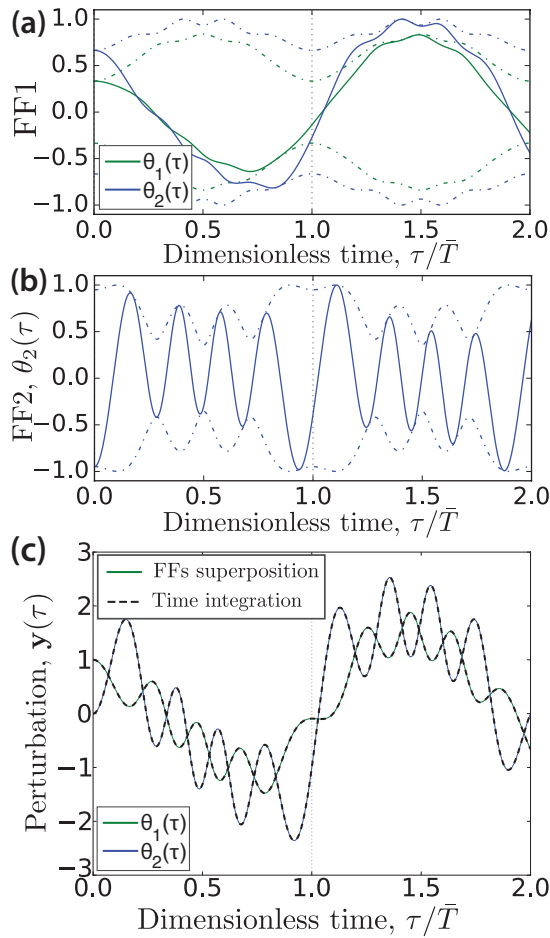


Figure 3.10: Vibratory response for  $\eta = 1$ ,  $\beta = 1.55\omega_1$ ,  $\lambda = 0.75\lambda_f$  and  $H = 5$ . (a) Time evolution of the angles  $\theta_1(\tau)$  and  $\theta_2(\tau)$  of the first fundamental FF  $\mathbf{y}_1(\tau) = \mathbf{p}_1(\tau)e^{s_1\tau}$  over the first two periods  $2T$  where  $T = 2\pi/\beta$ . The dash-dotted lines show the moduli of the periodic eigenfunctions  $|\mathbf{p}_n(\tau)|$  and  $-|\mathbf{p}_n(\tau)|$  that envelope the almost periodic motions. (b) Same as (a) but for the second fundamental FF (only  $\theta_2(\tau)$  is shown for a sake of clarity). (c) Time evolution of the angles  $\theta_1(\tau)$  and  $\theta_2(\tau)$  of the free vibratory response  $\mathbf{y}(\tau)$  of Eq.(3.3) for the initial conditions  $\theta_1(0) = 1$  and  $\theta_2(0) = \dot{\theta}_1(0) = \dot{\theta}_2(0) = 0$ . The response has been computed either with a classic direct iterative ODE solver or by recombining the FFs.

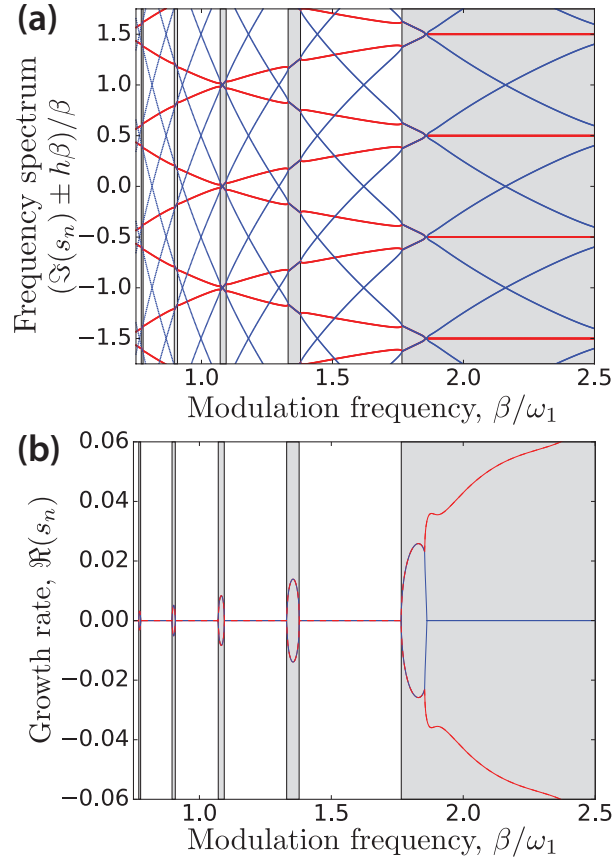


Figure 3.11: Evolution of the spectrum of the  $N = 4$  fundamental FFs as a function of  $\beta/\omega_1$  for  $\eta = 1$  and  $\lambda = 0.75\lambda_f$ . (a) Evolution of the frequency spectrum location of the FFs,  $\mathfrak{S}(s_n) + \sum_h ih\beta$ . (b) Evolution of the growth rate of the FFs,  $\Re(s_n)$ . The grey regions in (a) and (b) indicate that the straight Ziegler column is locally unstable.

as a function of  $\beta/\omega_1$  for  $\lambda = 0.75\lambda_f$  and  $H = 25$ . Similarly to Figs.3.3, 3.5 and 3.9, the frequency spectra  $\mathfrak{S}(s_n) + \sum_h ih\beta$  varies with the modulation parameters  $\lambda$  and  $\beta$  and can eventually lock-in. Because the FFs have a poly-harmonic spectrum and  $\eta = 1$ , it exists several ranges of frequency modulation  $\beta$  where the spectra of two different FFs are locked in frequencies that are not positive integer multiple of  $\beta/2$  (those are the regions where the red and blue colors in Fig. 3.11 mix and where every growth rates  $\Re(s_n)$  are different from zero in Fig. 3.11(b)). Those situations are qualitatively illustrated in Fig. 3.2(e) and are responsible for the Neimark-Sacker bifurcation illustrated in Fig. 2.2(d). The wider region of instability responsible for those secondary-hopf bifurcations corresponds to a lock-in of the fundamental harmonic of the two different FFs when the other ones are due to lock-in of sub-harmonics. It is interesting to note that in the main instability region (far right of Fig. 3.11), the spectra of the two FFs ultimately lock in  $i(\beta/2 \pm m\beta)$  when increasing  $\beta$ , i.e. the system undergoes a  $2T$ -instability. This main instability was already observed in Fig. 3.5.

Fig. 3.12(a) displays the stability chart of the straight Ziegler column with an end compressive positional following force in the modulation parameters space  $(\lambda, \beta)$ . Like in Fig. 3.6, the displayed stability chart obtained with the eigenvector sorting algorithm has been validated through the computation of the monodromy matrix and its Floquet multipliers in the time domain [11], leading to a map of truncation order  $H$  in the  $(\lambda, \beta)$

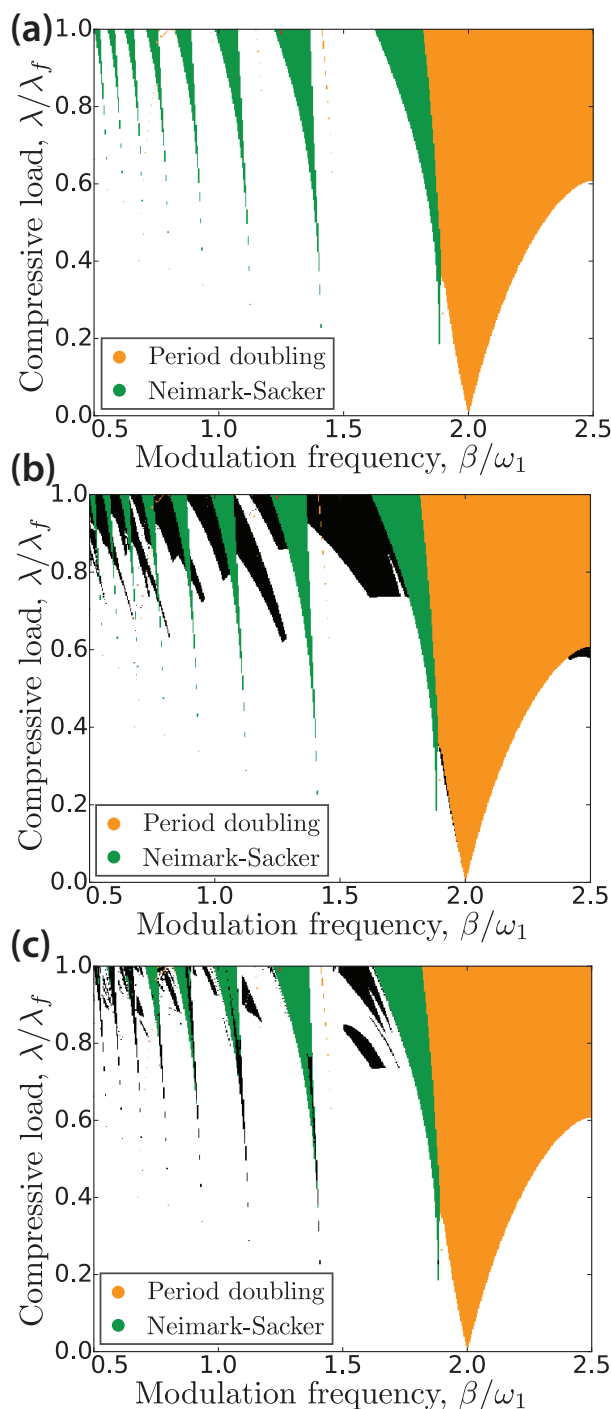


Figure 3.12: Stability chart of the non conservative system in the  $(\lambda, \beta)$  space for  $\eta = 1$ ,  $\beta \neq 0$  and a variable converged truncation order  $H$  given in Fig. 3.13(b). (a) Neimark-Sacker instability (green) and  $2T$ -instability (orange) regions computed through the eigenvector sorting algorithm. (b) Same stability chart but by analyzing the raw spectrum of the Hill matrix. The black color shows supplementary instability regions, a spurious numerical artifact inherent to the truncated Hill matrix. (c) Same stability chart but by using the eigenvalue sorting algorithm. The black color indicates supplementary instability regions where the eigenvalue sorting algorithm is not yet converged for the truncation order of Fig. 3.13(b). The stability is computed on a  $500 \times 500$  grid in the  $(\beta, \lambda)$  modulation parameter space and colors are plotted according to the closest data point.

space shown in Fig. 3.13(b). The system exhibits instability tongues that correspond to parameters for which at least one of the growth rate  $\Re(s_n)$  of the  $N = 4$  fundamental FFs is positive. Here, green regions are associated with secondary Hopf bifurcations and correspond to modulation ranges where the two physical FFs are locked in frequencies that are not integer multiple of  $\beta/2$  when the orange region shows the  $2T$ -instability situation related to a  $\beta/2 \pm m\beta$  lock-in of the fundamental of the resulting in-phase FF in the state space as illustrated in Fig. 3.11. Like in the conservative case in Fig. 3.6, the analysis of the full spectrum of Hill's matrix (no sorting) leads to a wrong stability diagram displayed in Fig. 3.12(b). Moreover, unlike for  $T$  and  $2T$ -instability regions, the eigenvalue sorting algorithm, represented by the stability chart of Fig. 3.12(c), is not giving the correct Neimark-Sacker instability regions for the optimal truncation order of Fig. 3.13(b). The reason is that for some modulation parameters and at this optimal truncation order, the sorted Floquet exponents  $s_n$  that are in the primitive spectral cell  $-\beta/2 \leq s_n < \beta/2$  are not yet converged because they are not the fundamental ones responsible for the Neimark-Sacker lock-in instability. On the contrary, the FFs computed with the eigenvector sorting algorithm are the fundamental ones, a property that is crucial when dealing with secondary Hopf bifurcations or stable FFs for small  $\beta$  as explained in Section 3.4.3.

### 3.6 Spectral convergence of the stability analysis

We focus here on the convergence of the spectrum of Hill matrix as a function of harmonic truncation order  $H$ . We have seen that the eigenvector sorting algorithm was converging the fastest, especially in the non-conservative case. Here, we want to see what minimum harmonic truncation order  $H$  is necessary to reach the desired accuracy in computing the linear stability, since the minimum dimension of Hill's matrix determines how much computational time will be needed for Floquet forms computation.

The stability charts of Figs. 3.6 and 3.12 have been computed and validated with a classic monodromy matrix algorithm in the time domain [11]. For each parameter  $(\beta, \lambda)$ , the  $N = 4$  Floquet multipliers of the Monodromy matrix were computed with a sufficiently small time step to ensure convergence and served as a reference solution. The Hill matrix was then constructed for various increasing truncation orders  $H$ . For each  $H$ , the Floquet multipliers  $\rho'_n$  were obtained from the  $N = 4$  fundamental Floquet exponents  $s_n$  computed with the eigenvector sorting algorithm explained in Section 3.3.1, thanks to the relation  $\rho'_n = e^{s_n T}$  where  $T = 2\pi/\beta$  is the dimensionless period of the considered perturbed elastic state. We defined a converged spectral truncation order  $H_{conv}$  as the minimal  $H$  for which the  $N = 4$  differences  $|\rho'_n - \rho_n|$  were not exceeding  $1 \times 10^{-6}$ . Where  $\rho_n$  is computed from the monodromy eigenproblem and  $\rho'_n$  from Floquet exponents computed from the Hill matrix eigenproblem.

The map of the converged truncation order  $H_{conv}$  in the  $(\beta, \lambda)$  space is given in Figs.3.13(a) and (b) for  $\eta = 0$  and  $\eta = 1$ , respectively. The number of required harmonics  $H_{conv}$  is generally larger as the modulation amplitude  $\lambda$  is enhanced and the frequency modulation  $\beta$  is decreased. Also more harmonics are required in the instability regions than in the stable ones. Those converged truncation order maps are the optimal ones

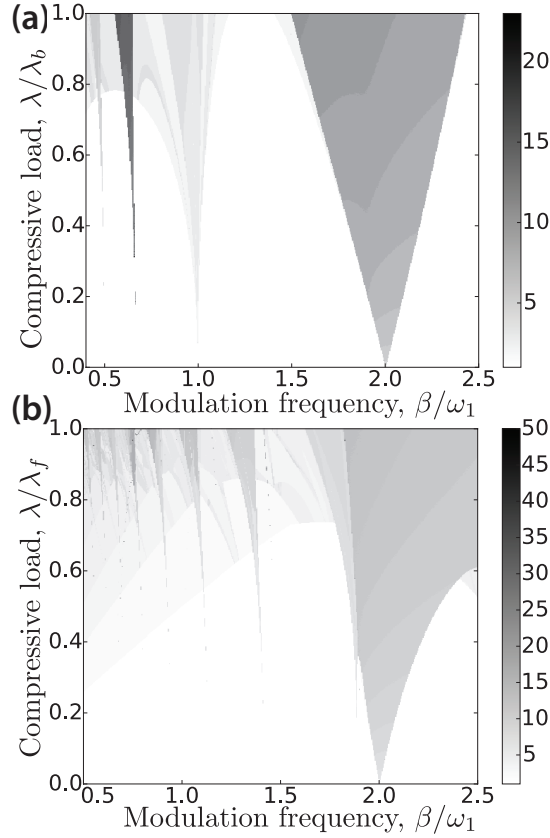


Figure 3.13: Optimal spectral truncation order map  $H_{conv}$  in the  $\beta, \lambda$  space to ensure convergence. (a) Conservative case  $\eta = 0$ . (b) Non conservative scenario  $\eta = 1$ . The stability is computed on a  $500 \times 500$  grid in the  $(\beta, \lambda)$  modulation parameter space and colors are plotted according to the closest data point.

when using the eigenvector sorting algorithm. If no sorting, the stability map would not converge and if using the eigenvalue sorting algorithm, one could need higher truncation order  $H_{conv}$ , especially for small  $\beta$  or in the non conservative case. Note finally that it appears from Fig. 3.13 that more harmonics are needed in the non conservative case than in the conservative one. This trend is however exaggerated as most of the numerical data converge for less than  $H = 25$  and only a very thin region, located around  $\beta/\omega_1 \approx 0.75$  and corresponding to a  $2T$  instability of the second FF, needs  $H = 50$ .

### 3.7 Discrete dynamical stabilization above buckling load

This goal of this section is to compute the Floquet forms of the Ziegler column under a harmonically-varying compressive load whose average amplitude is above buckling load. This case, driven by curiosity and mostly of mathematical interest, will allow us to show the robustness of our computation method in the frequency domain. Indeed, in such a LTP system, the naturally diverging Ziegler column can still be linearly dynamically stabilized but the stable regions become ultra thin in the modulation parameter space  $(\beta, \lambda)$ . Also, the neutrally stable almost-periodic FFs require a lot of harmonics in the computations.

This extreme sensitivity on modulation parameters as well as this particular harmonic dependence is not only well captured by the classic time-domain approach but also by the Hill matrix eigenvector sorting algorithm that we just show.

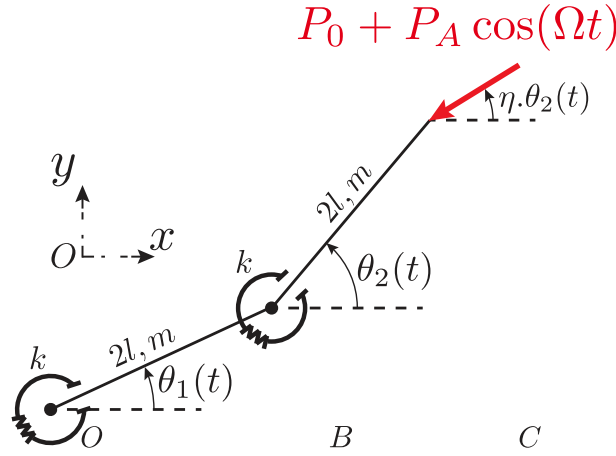


Figure 3.14: The Ziegler column from 3.1 is now statically diverging. The harmonically-varying compressive load is now decomposed in a static ( $P_0$ ) and dynamic ( $P_A \cos(\Omega t)$ ) component. The static compression is above critical buckling load ( $P_0 > P_{cr}$ ). The critical load is either the buckling or flutter load whether we consider the conservative ( $\eta = 0$ ) or non-conservative ( $\eta = 1$ ) scenario.

The test case under study is the periodically modulated Ziegler column that is statically diverging (see fig.3.14). In this scenario, the harmonically-varying axial load is  $P_0 + P_A \cos \Omega t$  where its average load is above the critical buckling load  $P_{cr}$  (or  $P_{cr}$  is the critical fluttering load if we consider the case of a following periodic force). What makes this domain interesting is that the introduction of a periodicity can dynamically stabilize the statically diverging system in certain cases of modulation. This is well known in literature notably in the case of an upside-down pendulum on a vibrating base, the so-called Kapitza pendulum [45]. However, in the case of Kapitza, the period of modulation is much shorter than the diverging time. In our case, we will focus on large period of modulation and we will see that dynamical stabilization is still possible but in a discrete fashion in the modulation parameter space.

We recall that our linear analysis of LTP system is only valid near its periodic stationary state. Therefore to quantitatively analyse the actual motion of the Ziegler column in instability regions of the modulation parameter space, a nonlinear analysis must be done as in section 2.2.1.

### 3.7.1 Conservative case

In figures 3.15 and 3.16 the stability chart and growth rates of the two FFs of the Ziegler column with a static compression of 2% over critical load ( $P_0 = 1.02P_{crit}$ ) are displayed in the case of a horizontal force throughout deformation (the so-called conservative scenario with  $\eta = 0$  in Fig.3.14). Those plots show that the instability regions change when varying the modulation amplitude  $\lambda$  and frequency  $\beta$ . When the instability region changes between unstable  $T$  and  $2T$  Floquet forms, there is a very thin region where the system is

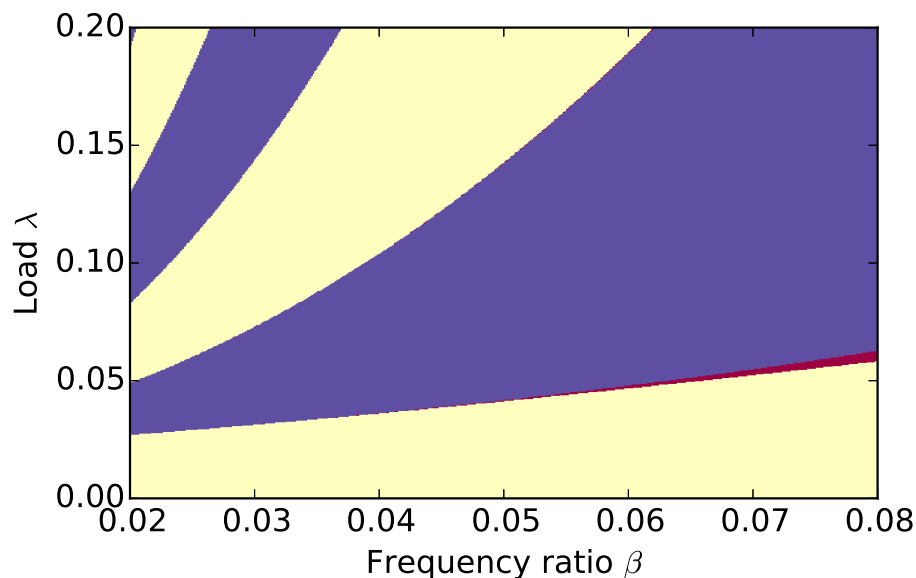


Figure 3.15: Stability zones of the conservative fundamentally unstable case with a static compression of 2% over critical load ( $P_0 = 1.02P_{crit}$ ) in the modulation parameter space  $(\beta, \lambda)$ . The dimensionless load is shown on the y-axis ( $\lambda = P_A/P_{crit}$ ). The stability zones are marked in different colors where red is stable, yellow depicts  $T$ -instability, purple indicates  $2T$ -instability regions. Between each change of  $T$  to  $2T$  instability regions and vice versa, a stability zone can be observed. The stability is computed on a  $250 \times 250$  grid in the  $(\beta, \lambda)$  modulation parameter space and colors are plotted according to the closest data point.

stable. This stability region can be seen by the drop in growth rate illustrated in Fig.3.16. This proves that for a structure in periodic state that would statically diverges, linear stability can still be found, even at small modulation frequency. The width of the stability regions decrease as the frequency decreases. Another information from Fig.3.16 shows the growth rate is at a maximum at the centre of the instability regions. A maximum growth rate indicates the transfer of energy between the axial periodic force and the transverse free vibratory response is the most efficient. The Floquet exponent computed with linear periodic analysis can be a starting point for a nonlinear investigation of the system. An application for maximum response amplitude and transfer energy is for example flutter-type energy harvesters [81].

Note that the stability calculations have been verified at high frequency to compute at which frequency-amplitude threshold the system becomes stable. Derivations of averaged equations of motion are found in appendix C. At low frequency the transverse vibratory response reconstructed by Floquet forms has been validated by direct time-integration. These verifications are useful as it shows the robustness of FF computation using Hill's method with eigenvector sorting.

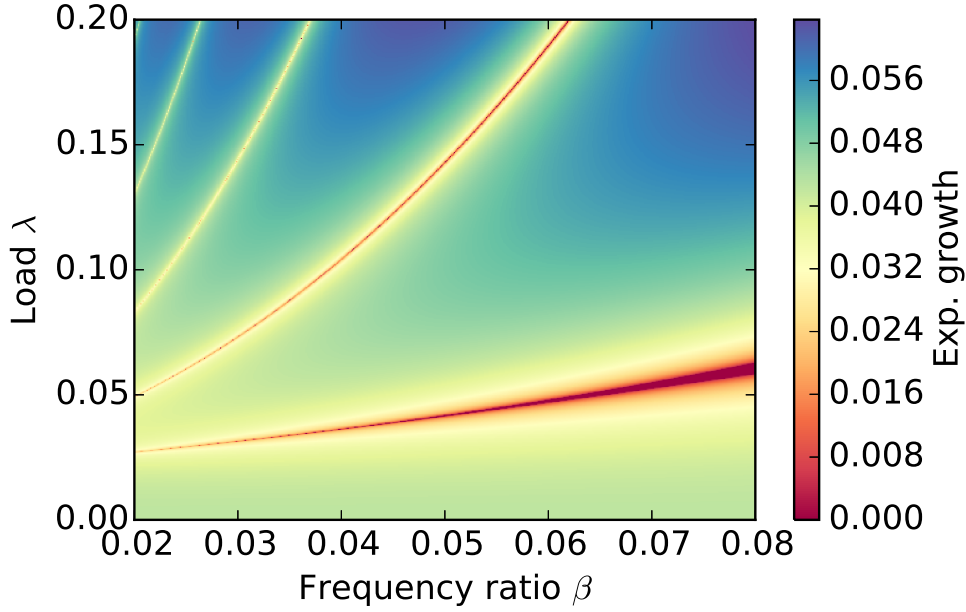


Figure 3.16: Evolution of FFs growthrate of the conservative case with a static compression of 2% over critical load ( $P_0 = 1.02P_{crit}$ ) in the modulation parameter space  $(\beta, \lambda)$ . The dimensionless load is shown on the left hand side ( $\lambda = P_A/P_{crit}$ ). The growth rate decreases to zero at changes in stability zones between  $T$  and  $2T$ . The stability is computed on a  $250 \times 250$  grid in the  $(\beta, \lambda)$  modulation parameter space and colors are plotted according to the closest data point.

### 3.7.2 Finding stability zones

To get deeper physical insights in the stability regions, we zoom on the Floquet exponent of the computed Floquet forms close to the stability zones. In Fig.3.17, the real and imaginary parts of the Floquet exponents are shown for a fixed modulation frequency  $\beta$  and varying modulation amplitude  $\lambda$ . The Floquet exponent of the two FFs are plotted as blue and green dots. On each figure, 500 Floquet exponents are shown that are linearly distributed on a given  $\lambda$  interval. On the left hand side,  $\lambda = [0, 0.20]$ . The right hand side is a zoom where  $\lambda = [0.0335, 0.0345]$ . Instability regions in  $\lambda$  corresponds to  $\Re(s_1) > 0$  and they occur because for this conservative system, a frequency lock-in occurs between FF1 and its complex conjugate ( $\Im(s_1) = \Im(\bar{s}_1)$ ) on figures 3.17(a) (instability regions correspond to arrays of vertical dots where the frequency spectrum of the Floquet forms is locked-in). The system becomes stable again when FF1 unlocks ( $\Im(s_1) \neq \Im(\bar{s}_1)$ ). The imaginary part of the Floquet exponents in fig.3.17(a) show where unlock occur between instability zones very clearly because we see jumps. Fig.3.17(b) shows how the real part, or growth rate, of the first Floquet form shown in blue, decreases in those jumps region. The frequency un-locking of the first FF can not be directly observed from 3.17(a),(b). However we know that when the system switches between  $T$  and  $2T$  instability zones the FF-frequencies must unlock. This means that in between the instability zones, there is a stability zone. Although it is too small to observe directly. Fig.3.17(c),(d) zoom in on the first switch of instability zone where Floquet exponents are recomputed. Their real part  $\Re(s_1)$  is shown in fig.3.17(c) and can be seen to decrease to zero. The imaginary part fig.3.17(d) is seen to have a transition between 0 and 0.5 where the FF is unlocked

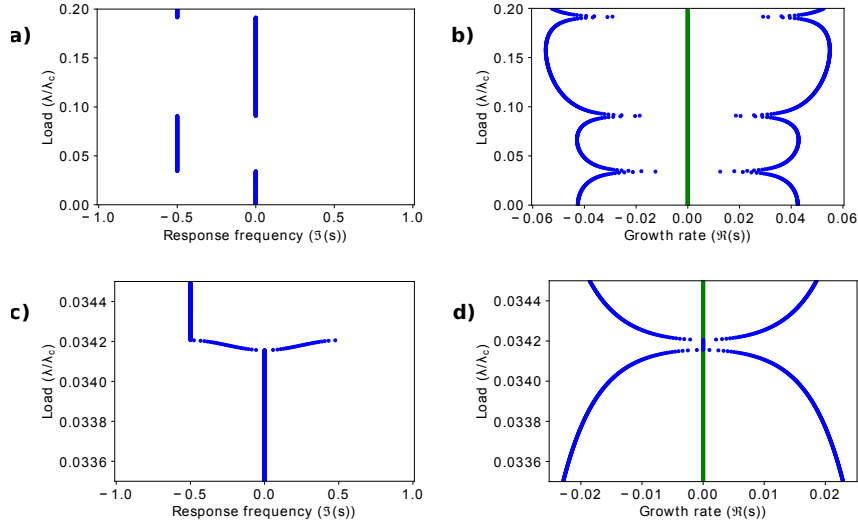


Figure 3.17: Floquet exponents ( $s_1, s_2$ ) under varying load  $\lambda$  on the vertical axis with  $\beta = 0.036$ . In each figure there are 500 linearly distributed  $\lambda$  measurement points. **a)** The fundamental frequencies relative to the modulation ( $\Im(s_1)/\beta$ ) over the interval  $\lambda = [0, 0.20]$ . The frequency is limited to  $\pm 1$  where the first fundamental Floquet exponent switches between 0 and 0.5. **b)** The growth rate ( $\Re(s_n)$ ) over the interval  $\lambda = [0, 0.20]$ . **c)** The fundamental frequencies relative to the modulation ( $\Im(s_n)/\beta$ ) over the interval  $\lambda = [0.0335, 0.0345]$ . **d)** The growth rate ( $\Re(s_n)$ ) over the interval  $\lambda = [0.0335, 0.0345]$ .

$$\Im(s_1) \neq \Im(\bar{s}_1).$$

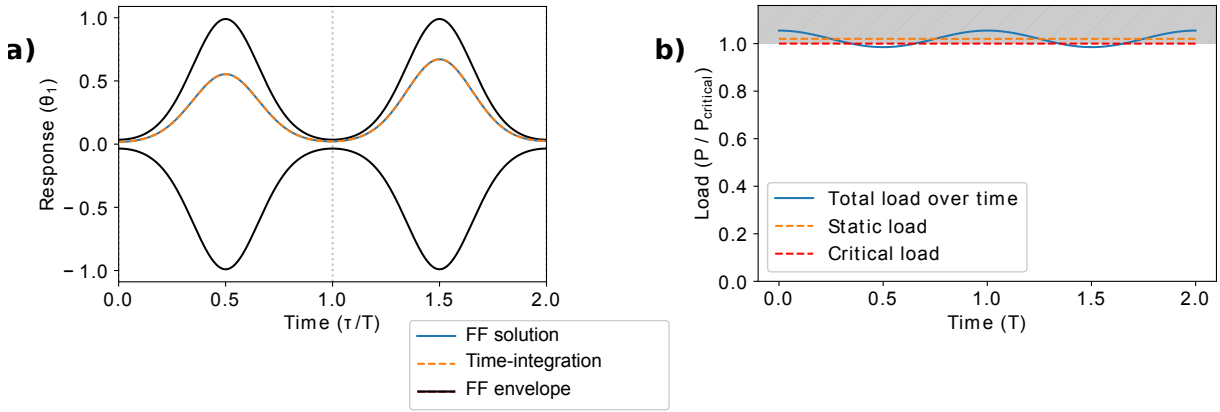


Figure 3.18: Properties of the first stability zone at  $\beta = 0.036$  and load  $\lambda = 0.034156$ . **a)** Angular displacement  $\theta_1(t)$  of the first FF computed in the frequency domain (blue) and validated by direct time-integration with initial conditions to remain on first FF (orange). The FF-envelope (black) shows the limits predicted by the FF solution. **b)** The compression applied over time. The total load (blue) is composed of the static load (orange) and a periodic load  $P_{periodic} = \lambda P_{cr} \cos \beta \tau$ . The grey area shows where the load is above the critical buckling load  $P_{cr}$  (red).

### 3.7.3 Stability Zone Characteristics

The vibratory response and compressive load of the first neutrally stable Floquet form in the first stability zone is shown in Fig.3.18 over two periods. In Fig.3.18(a) the angular dis-

placement  $\theta_1$  of the first Floquet form is shown and compared to a direct time-integration of the equations of motion with particular initial conditions to stay on the first FF.

Besides verifying the response, the envelope of  $\theta_1$  is computed using the absolute value of the first Floquet form over time

$$\mathbf{v}(t) = |\mathbf{p}_1|(t), \quad (3.30)$$

where  $\mathbf{v}(t)$  is the envelope of the vibratory response in the state space. The periodic envelope itself has one belly at  $t = T/2$  and one node at  $\tau = 0$  and  $\tau = T$ . This shows an elegant way of determining limits of the vibratory response in a time-periodic system. The corresponding harmonically-varying axial load is illustrated in Fig.3.18(b) where we see it has a small dynamic component. Its amplitude is  $\lambda P_{cr} = 0.034156 P_{cr}$ , which is relatively small compared to static load  $P_0 = 1.02 P_{cr}$ . It is also interesting to observe the phase between the modulation load and the transverse vibratory response of the Ziegler column.

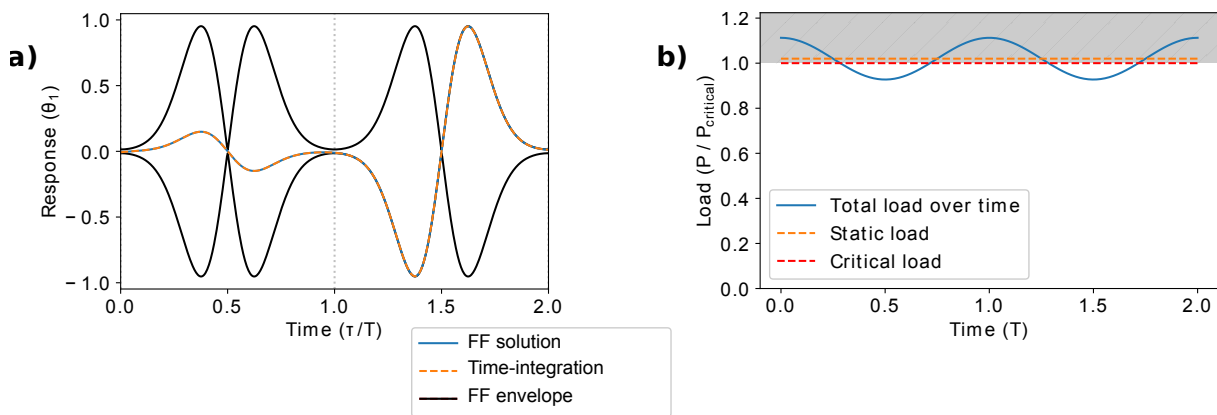


Figure 3.19: Properties of the second stability zone at  $\beta = 0.036$  and load  $\lambda = 0.090811$ . a) Angular displacement  $\theta_1(t)$  of the first FF computed in the frequency domain (blue) and validated by direct time-integration with initial conditions to remain on first FF (orange). The FF-envelope (black) shows the limits predicted by the FF solution. b) The compression applied over time. The total load (blue) is composed of the static load (orange) and a periodic load  $P_{periodic} = \lambda P_{cr} \cos \beta \tau$ . The grey area shows where the load is above the critical buckling load  $P_{cr}$  (red).

Fig.3.19 shows the angular displacement of  $\theta_1(t)$  of the first Floquet form in the second instability regions as well as the periodic axial force applied relative to the critical buckling load  $P(t)/P_{cr}$ . This second instability zone occurs at a higher load  $\lambda = 0.090811$  than the first stability region. In both regions, the first Floquet form are neutrally stable but qualitatively different. Notably, the envelope in the second stability region shows two bellies and two nodes (at  $t = 0, t = T/2$ ), instead of one belly and one node as was the case in Fig.3.18(a). The compressive load applied is visualized in Fig.3.19(b). The dynamic force amplitude is now approximately 9% of the critical load.

In fig.3.20(a) the time response and envelope of a first FF in the third stability zone have been computed and validated. This third stability region is obtained by fixing the modulation frequency at  $\beta = 0.036$  and the corresponding oscillatory load at  $\lambda = 0.191417$ . This time, we can clearly see three bellies and three nodes in the envelope.

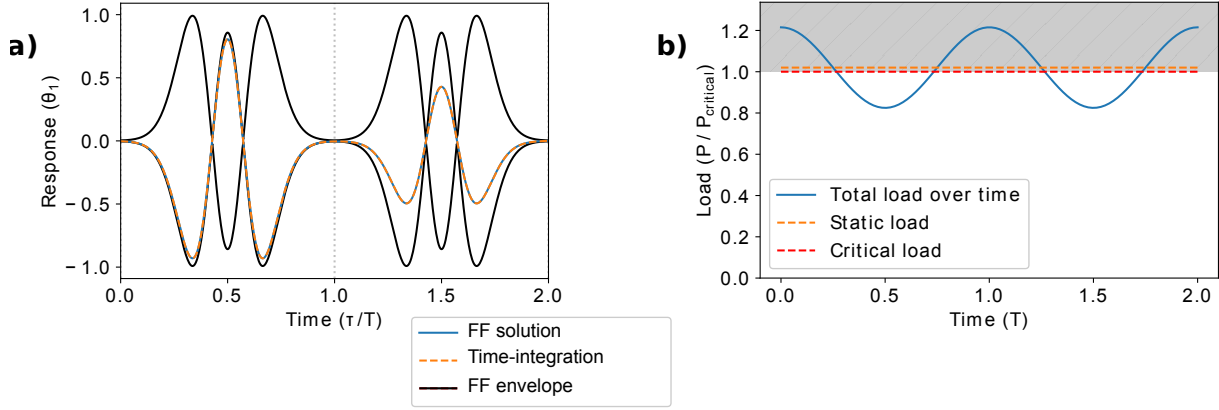


Figure 3.20: Properties of the third stability zone at  $\beta = 0.036$  and load  $\lambda = 0.191417$ . a) Angular displacement  $\theta_1(t)$  of the first FF computed in the frequency domain (blue) and validated by direct time-integration with initial conditions to remain on first FF (orange). The FF-envelope (black) shows the limits predicted by the FF solution. b) The compression applied over time. The total load (blue) is composed of the static load (orange) and a periodic load  $P_{periodic} = \lambda P_{cr} \cos \beta \tau$ . The grey area shows where the load is above the critical buckling load  $P_{cr}$  (red).

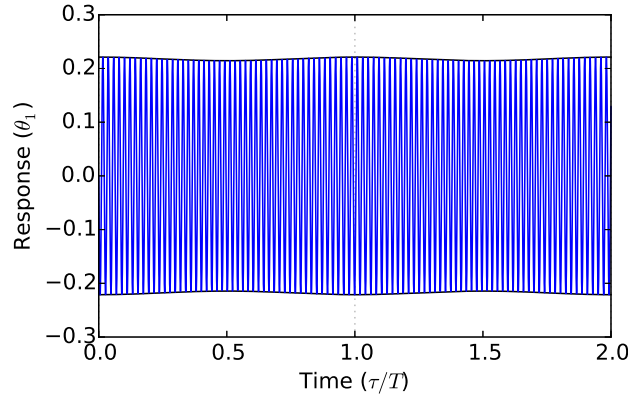


Figure 3.21: Second Floquet form in the third stability zone at  $\beta = 0.036$  and load  $\lambda = 0.191417$ . The second Floquet form is not statically diverging because the average applied load  $P_0$  is below the second buckling mode).

The response of a second FF in the third stability zone is shown in fig.3.21. Because we are in a conservative system (the axial load remains horizontal throughout the motion and does not couple the modes) FF2 is uncoupled from FF1. Moreover, the second FF is not statically diverging like the first FF because the static compressive load  $P_0$  is way below the second buckling mode. Also, the envelope is modulated very slowly compared to the response because the fundamental frequency of the second FF ( $\Im(s_2)$ ) is about 50 times higher than the compression frequency  $\beta$ . This shows that FF2 is very little affected by the modulations and is very close to a classic harmonic eigenmode.

In fig.3.22 the Fourier series of the two FFs in the third stability zone are shown. Fourier series are easy to observe because we can decompose our Floquet form  $\mathbf{y}_n(t) = \sum_{h=-H}^H \mathbf{p}_n^h e^{(s_n + i\beta h)t}$  and look at the contribution of the vibratory response per harmonic. On the vertical axis the norm  $|\mathbf{p}_n^h|$  is shown. While on the horizontal axis the response

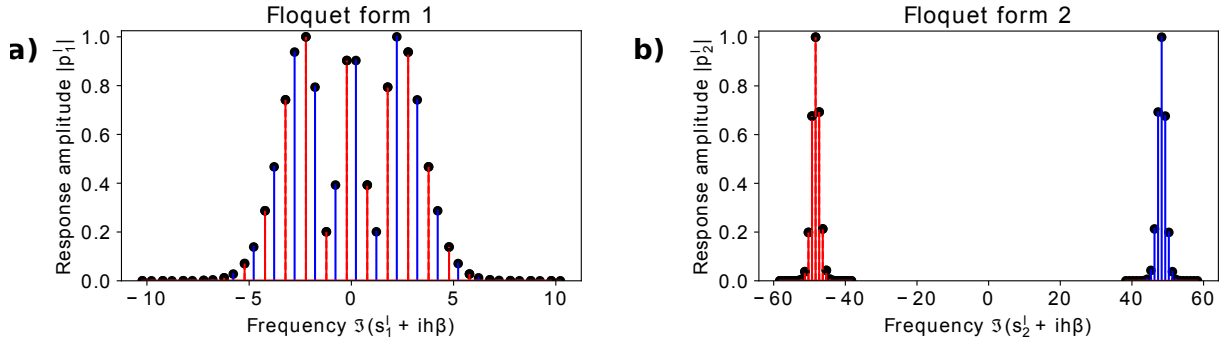


Figure 3.22: The FF-amplitudes in the 3rd stability domain. On the vertical axis are the norms per frequency  $|\mathbf{p}_n^h|$  normalized with the largest norm. On the horizontal axis the frequency normalised  $\Im s_n + ih\beta/\beta$  a) FF1 (blue) and its complex conjugate (red) b) FF2 (blue) and its complex conjugate (red)

frequency normalised with the excitation frequency is shown  $\Im(s_n + ih\beta)/\beta$ . Fig.3.22(a) shows the frequency spectrum of FF1 and its conjugate. Fig.3.22(b) shows the frequency spectrum of FF2 and its conjugate.

We see that in this conservative case, the frequency spectrum of FF1 and FF2 is totally uncoupled, since on very different frequency scale (this will not be the case for non-conservative case).  $T$  and  $2T$  instabilities are explained by the frequency locking of FF1 with its own complex conjugate on multiple harmonics of  $\Im(s_1^l) = 0$  or  $\Im(s_1^l) = \beta/2$ , respectively. We see here that the studied case is neutrally stable because there is no lock-in between a Floquet form and its conjugate. For secondary Hopf bifurcations FF1 has to lock into FF2. This is not happening in conservative cases. To see secondary Hopf bifurcations we need to focus our attention to the nonconservative case.

### 3.7.4 Nonconservative case

We now focus on the non-conservative case where the time-varying axial load is known following the tip of the Ziegler column ( $\eta = 1$ ). This time, the average of the periodic load is above the critical fluttering load. Unlike the conservative case, it is more difficult to find regions where the Ziegler column is dynamically stable instability zones, but stability regions can still be found. By still being able to compute stability under these circumstances, the robustness of Hill matrix eigenvector sorting is demonstrated.

In figure 3.23, we see the maximum growth rate of the two Floquet forms of the transverse free vibratory response of the naturally fluttering Ziegler column in periodic elastic state. The growth rate is almost everywhere positive which means the straight Ziegler column is almost always dynamically unstable and an almost-periodic motion should almost always take place. However, dynamical stabilization can be found because the growth rate drops to zero in thin stability stripes of  $(\beta, \lambda)$ . This shows that even between almost-periodic instabilities, there must be stability zones as well (because the various instability regions still correspond to various sub-harmonics lock-in of Floquet forms).

By zooming in as explained in section 3.7.2 we can study the neutrally stable Floquet

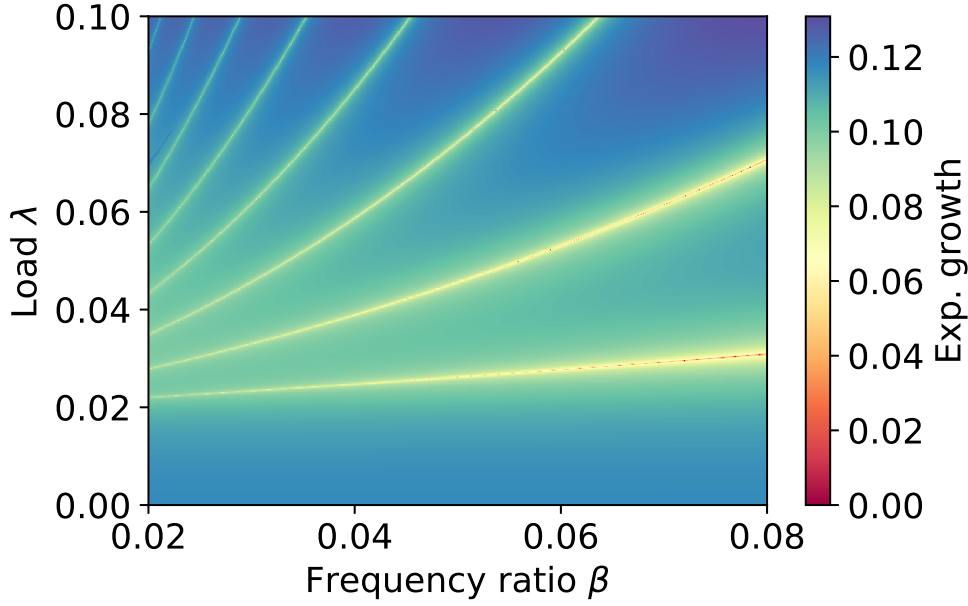


Figure 3.23: The growthrate for the nonconservative case in the modulation parameter space  $(\beta, \lambda)$ . On the vertical axis, the load is made dimensionless by dividing it over the critical fluttering load ( $\lambda = P_A/P_{cr}$ ). Stability zones are observed as very thin stripes with zero growth rate. The static load is 2% above the critical fluttering load  $P_0 = 1.02P_{cr}$ . The stability is computed on a  $250 \times 250$  grid in the  $(\beta, \lambda)$  modulation parameter space and colors are plotted according to the closest data point.

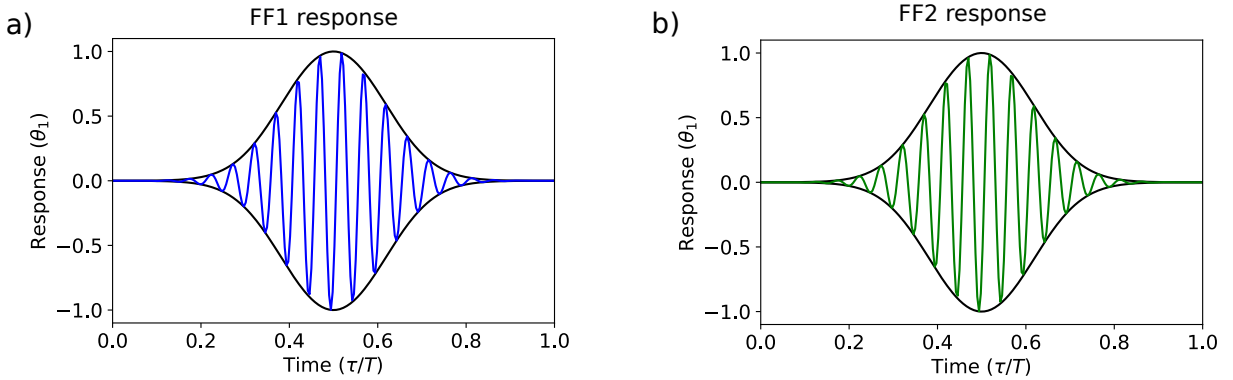


Figure 3.24: Floquet forms of nonconservative case  $\eta = 1$  in the first stability zone with frequency  $\beta = 0.036$ , dynamic load factor  $\lambda = 0.02425145358$  and static load factor  $a = 1.02$  are plotted over 1 period  $T$ . a) Response  $\theta_1(t)$  of FF1 and its envelope. b) Response  $\theta_1(t)$  of FF2 and its envelope.

forms corresponding to modulation parameters  $(\beta, \lambda)$  located in the aforementioned stability regions. In figure 3.24 the response of a first and second FF in the first stability zone are shown. The modulation parameters  $(\lambda, \beta)$  are obtained like in section 3.7.2 by finding a region where both growth rate of the FFs are zero. The big difference with the neutrally stable FFs obtained in the conservative scenario is the coupling between FFs (see figures 3.20, 3.21 and 3.21 for comparison). Here, the response and envelopes are nearly identical.

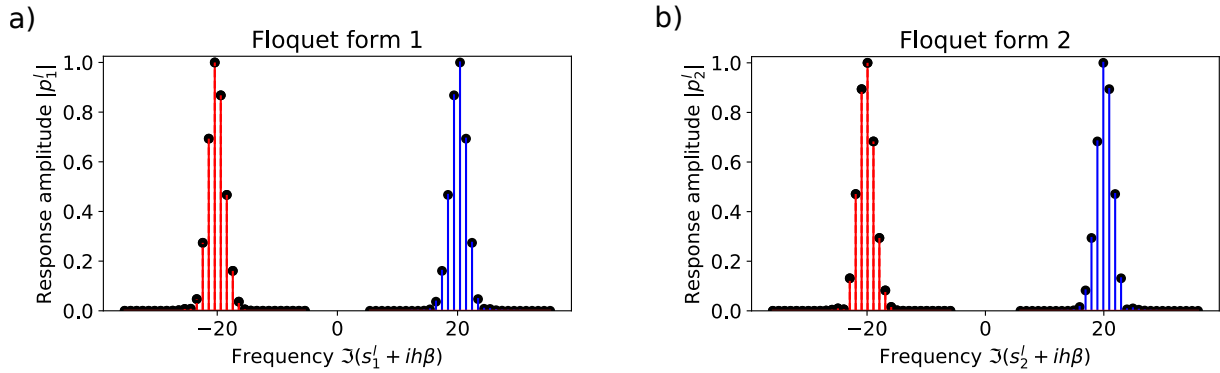


Figure 3.25: FF spectral amplitudes in the first nonconservative stability domain. On the vertical axis the norms per frequency are plotted  $|\mathbf{p}_n^h|$ . On the horizontal axis are the normalized frequencies  $\Im s_n + ih\beta/\beta$  a) FF1 (blue) and its complex conjugate (red), b) FF2 (blue) and its complex conjugate (red).

Figure 3.25 illustrates through the frequency spectrum of each FF  $|\mathbf{p}_n^h|$ , how similar FF1 and FF2 are (the spectrum of each modes are almost locked-in). This is again not surprising because almost-periodic instabilities emerge because of the frequency lock-in of two FFs. This is different from the conservative case where FF1 was locking-in with its own complex conjugate (see fig.3.22).

### 3.8 Conclusions

In this chapter Floquet form computation has been discussed and methods in the frequency domain have been compared. The potential of FFs have been explored by demonstrating the robustness of stability analysis via fundamental Floquet exponents and dynamic properties of FF-response.

When comparing frequency domain methods, we have seen that sorting the Hill spectrum is necessary to obtain accurate results. It turns out the eigenvector sorting algorithm requires the least number of harmonics because it computes the fundamental FFs. Eigenvalue sorting in the primitive cell is very efficient in case of steady state or flip bifurcations but for Neimark-Sacker bifurcation, eigenvalue sorting can require a large number of harmonics to converge. This is due to the Hill spectrum being far from the primitive cell. When converged fundamental FFs are computed, they can be used to analyze the LTP system free vibratory response. By decomposing the response into FFs and analyzing these individually, the principal motions of the system are revealed. Furthermore, the envelope of the almost-periodic response can be computed using the norm of the periodic eigenvector and FF-amplitude.

By numerically analyzing the free transverse vibration of a straight Ziegler column in periodic elastic state, we have been able to show the robustness of stability computations through the fundamental FFs. Whether the axial periodic applied load leads to conservative or non-conservative problems, wether to determine steady-state, flip or Neimark-Sacker bifurcations, the vibratory response reconstructed by FFs and direct time

---

integration showed always good agreement. Even when the dynamical stabilization was extremely reduced in the modulation parameter space because the average of the applied periodic load was above critical buckling or fluttering threshold, our frequency domain computation were still robust.

In the next chapter, we will see how to use fundamental FFs to reduce LTP systems of large dimension on an orthonormal basis of FFs where the presented stability analysis could be then conducted at low computational costs.



# Time-periodic modal analysis

---

Modal analysis consists of decomposing a small vibrational motion into its natural modes of oscillation in order to gain physical insights in the dynamics of a structure. In classic modal analysis, the vibrational response is linearly decomposed on a basis of harmonic eigenmodes. An essential theoretical feature of this method is that, upon projection of the linear equations of motion on a truncated basis of eigenmodes, the original set of ordinary differential equations (ODEs) can be properly approximated by a set of ODEs of smaller dimension. Of course, a smaller number of equations leads to faster time-integration and shorter CPU times.

In the particular case of the perturbation of a structure in constant equilibrium state, classic harmonic eigenmodes form an orthonormal basis of the linear vibrations. Thus if the discrete dynamical system is governed by ODEs with time-independent coefficients, the projection on eigenmodes can result in a set of uncoupled ODEs that greatly simplifies the physics underlying the structural vibration. In case of a vibrational response of a structure in periodic elastic state, time-periodic ODEs can be projected on harmonic eigenmodes but the new reduced set of time-periodic ODEs will remain coupled because of the time-periodic coefficients. Classic harmonic eigenmodes constitute a proper orthonormal basis in space but not in time, and such a projection is incomplete.

In this chapter we will show that the almost-periodic Floquet forms, that we computed in the frequency domain in chapter 3, are the generalization of the classic harmonic eigenmodes. In fact, Floquet forms constitute a true orthonormal basis for the linear vibrations of a structure in periodic elastic state, meaning it is possible to project a set of time-periodic ODEs on their Floquet forms to obtain a reduced set of uncoupled ODEs with constant coefficients. In that sense, Floquet forms simplify the system not only in space but also in time since the original time-periodic stiffness will be replaced by a diagonal stiffness matrix whose entries are related to the Floquet exponents.

Like for classic modal analysis, in the following we will make the distinction between free and forced vibrations, i.e. autonomous and non-autonomous systems or homogeneous and non-homogenous linear ODEs with time-periodic coefficients. When the structure is in free vibration, the oscillatory response is induced by the initial conditions. In that case, FFs transform the original set of time-periodic ODEs in uncoupled ODEs with constant coefficients that can be analytically solved. Thus, once Floquet forms are computed, no time-integration is needed to solve a free vibration problem involving structures in time-periodic elastic states. In forced vibration, we will focus on the stationary response induced by an external excitation. Upon projection of the external force, the latter is multiplied by a periodic term in the case of time-periodic system. As a consequence, the

projection of a forced vibration problem with constant forces will lead to a set of ODEs with constant coefficients subjected to periodic forces and harmonic forces will lead to almost-periodic forces in the orthonormal basis of Floquet forms.

## 4.1 Modal-Floquet Transformation

The fundamental case under study we choose is the periodically prestressed 2D beam of section 2.2, subjected to external forces. Fig.4.1 shows again the finite element discretization of the beam under lateral loading. Recall the beam is subjected to periodic prestresses  $\sigma_g(t)$  that are responsible of its time-periodic elastic state. We have shown

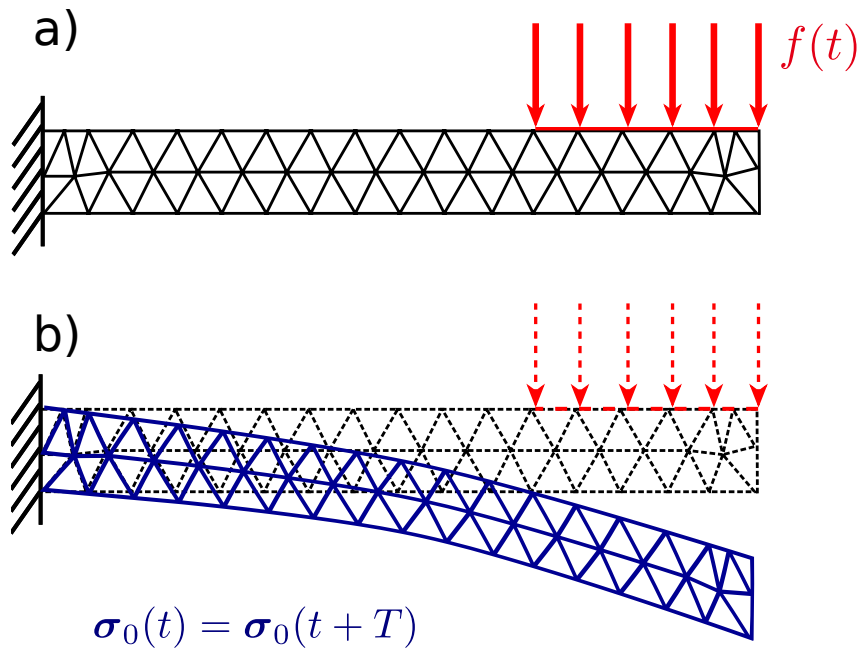


Figure 4.1: Finite element model of 2D beam under compression (a) the beam at initial configuration with time dependent geometric stiffness ( $\sigma_g(t)$ ), density ( $\rho$ ), Young's modulus ( $E$ ) and length and height ( $l, h$ ). A line force ( $f(t)$ ) is applied on the beam, between  $0.75l$  and  $l$ . (b) the current configuration changes over time.

in section 2.2.2 that the periodic prestresses are taken into account in the equations of motion through a harmonically time varying stiffness. After discretization by the Finite Element Method we obtain the  $N$ -dimensional equation:

$$\mathbf{M}\ddot{\mathbf{x}}(t) + (\lambda\mathbf{K}_c \cos(\beta t) + \mathbf{K}_0) \mathbf{x}(t) = \mathbf{F}(t), \quad (4.1)$$

where  $\mathbf{K}_0$  and  $\mathbf{K}_c$  are the stiffness and critical geometric stiffness matrix, respectively, and  $\mathbf{M}$  is the mass matrix. The critical geometric stiffness matrix is scaled by a factor  $\lambda$  and is harmonically varying with a fundamental frequency  $\beta$ . The vector  $\mathbf{F}(t)$  is the vector of external forces and  $\mathbf{x}(t)$  represents the vector of degrees of freedom in the physical space. The assembly of these matrices and vectors is done using the finite element software

FEniCS [71]. The equation of motion (4.1) is easily rewritten in state space:

$$\begin{bmatrix} \mathbf{0} & \mathbf{M} \\ \mathbf{I} & \mathbf{0} \end{bmatrix} \begin{pmatrix} \dot{\mathbf{x}}(t) \\ \dot{\mathbf{z}}(t) \end{pmatrix} = \begin{bmatrix} (-\lambda \mathbf{K}_c \cos(\beta t) - \mathbf{K}_0) & \mathbf{0} \\ \mathbf{0} & \mathbf{I} \end{bmatrix} \begin{pmatrix} \mathbf{x}(t) \\ \mathbf{z}(t) \end{pmatrix} + \begin{pmatrix} \mathbf{F}(t) \\ \mathbf{0} \end{pmatrix}, \quad (4.2)$$

which is a  $2N$ -dimensional set of Ordinary Differential Equations (ODEs) where we have introduced  $\dot{\mathbf{x}}(t) = \mathbf{z}(t)$ .

The goal in this chapter will be to project, on its basis of Floquet Forms, the discretized system (4.2) associated with the free and forced transverse vibrations of the beam in periodic elastic states. Without loss of generality, the following methods and results could be applied to other slender structures in periodic elastic states whose equation of motion are governed by a set of  $N$  numbers of Ordinary Differential Equations (ODEs) with periodic coefficients. The linear system (4.2) can be analyzed by direct integration over time but the CPU time could be excessive and no further insights will be gain from the computations. Or the system could be projected on a reduced basis of harmonic modes like in section 2.4. This would result in faster CPU time but in a coupled set of equations meaning the basis is not completely orthonormal in the space-time space. The last method that we will develop here is to project equation (4.2) on a fully orthonormal basis of Floquet Forms in order to obtain a reduced set of uncoupled ODEs with time-independent coefficients. We will compare those three methods and show they lead to the same results, albeit with a difference in time computation and physical understanding.

Two main approaches could be taken when projecting the system (4.2) on the basis of its Floquet Forms. One could directly compute the Floquet forms of (4.2) that is of an arbitrarily large dimension. But in the frequency domain, the dimension of Hill's matrix introduced in chapter 3 could become very large, if not unmanageable, with already a few harmonics. In the following, the large number of degrees of freedom are managed by first projecting the equation of motion on classic harmonic eigenmodes. This leaves a reduced set of coupled equations with time periodic coefficients which can, in turn, be projected on its orthonormal basis of Floquet forms in order to obtain a set of uncoupled time-invariant ODEs. The two projection methods lead to the same results but solving an extra large eigenvalue problem that we then sort and truncate will require a lot more computational effort than solving one classic eigenvalue problem that we truncate followed by finding the Floquet Forms of a Hill matrix of reasonable size.

Recall the modal transformation of section 2.4 where the vibratory response  $\mathbf{x}(t)$  of equation (4.2) is decomposed into a series of modes

$$\mathbf{x}(t) = \mathbf{X}\mathbf{T}(t). \quad (4.3)$$

The matrix  $\mathbf{X}$  of dimension  $N \times n$  contains in columns the shape of the  $n$  first modal eigenvectors we chose to keep on the basis while  $\mathbf{T}(t)$  is an  $n$ -dimensional vector representing the modal amplitudes which are time dependent. By projecting on a small number of modes, as shown in section 2.4, the equations of motion are reduced to a  $n$ -dimensional set of ODEs in the form:

$$\ddot{\mathbf{T}} + \left( \omega_0^2 + \lambda \hat{\mathbf{K}}_c \cos(\beta t) \right) \mathbf{T} = \mathbf{X}^T \mathbf{F}(t), \quad (4.4)$$

in the physical space which can be expanded in the form of a  $2n$ -dimensional set of ODEs

$$\begin{bmatrix} \mathbf{0} & \mathbf{I} \\ \mathbf{I} & \mathbf{0} \end{bmatrix} \begin{pmatrix} \dot{\mathbf{T}}(t) \\ \dot{\mathbf{V}}(t) \end{pmatrix} = \begin{bmatrix} (-\lambda \hat{\mathbf{K}}_c \cos(\beta t) - \boldsymbol{\omega}_0^2) & \mathbf{0} \\ \mathbf{0} & \mathbf{I} \end{bmatrix} \begin{pmatrix} \mathbf{T}(t) \\ \mathbf{V}(t) \end{pmatrix} + \begin{pmatrix} \mathbf{X}^T F(t) \\ \mathbf{0} \end{pmatrix}, \quad (4.5)$$

in the state space where we have introduced the  $2n$ -dimensional vector of state variables. Thanks to modal projection, the projected stiffness matrix  $\boldsymbol{\omega}_0^2$  is diagonal but the particularity of time-periodic systems is that the modal periodic stiffness matrix  $\hat{\mathbf{K}}_c$  is a full matrix because the eigenmodes were computed with the mass matrix  $\mathbf{M}$  and material stiffness  $\mathbf{K}_0$  only, in equation (4.5) (see section 2.4 for more precision). Therefore the equations of motion are reduced but coupled, which shows the matrix of eigenvectors  $\mathbf{X}$  was not a complete orthonormal basis. At that point, one could always integrate equation (4.4) over time to compute the modal amplitude  $\mathbf{T}(t)$  and physical vibratory response  $\mathbf{x}(t)$  through equation (4.3).

But an alternative solution exists that consists in applying a Floquet transformation on the modal amplitudes  $\mathbf{T}(t)$ . In the state space, this transformation applies on  $\mathbf{Y}(t) = \{\mathbf{T}(t), \mathbf{V}(t)\}^T$  and reads

$$\mathbf{Y}(t) = \mathbf{p}(t)\mathbf{q}(t) = \begin{bmatrix} \mathbf{w}(t) \\ \dot{\mathbf{w}}(t) \end{bmatrix} \begin{pmatrix} \mathbf{r}(t) \\ \dot{\mathbf{r}}(t) \end{pmatrix}, \quad (4.6)$$

where  $\mathbf{p}(t)$  is the  $2n \times 2m$  matrix which contains the periodic eigenvectors in columns and  $\mathbf{q}(t)$  is the  $2m$ -dimensional vector regrouping the Floquet Form amplitudes as described in section 2.3.1. The  $n \times 2m$  matrices  $\mathbf{w}(t)$  and  $\dot{\mathbf{w}}(t)$  are the periodic eigenfunctions of the Floquet Forms in the physical space when the  $m$ -dimensional vectors  $\mathbf{r}(t)$  and  $\dot{\mathbf{r}}(t)$  are the Floquet forms amplitudes and their time derivatives. Equation (4.6) is a transformation from modal to Floquet coordinates where  $m$  is the number of physical Floquet Forms that we keep in the basis, with  $m \leq n \leq N$ . This Floquet transformation is applied to decouple and eventually reduce the equations of motion as we will see in section 4.2. After the modal and Floquet transformations, the physical oscillatory response of the discretized structure of fig.4.1 is described by the mode shape, Floquet eigenfunction and amplitude:

$$\mathbf{x}(t) = \mathbf{X}\mathbf{w}(t)\mathbf{r}(t). \quad (4.7)$$

The decomposition (4.7) is crucial since it allows to reconstruct the physical response  $\mathbf{x}(t)$  once the Floquet amplitudes have been computed as will be shown in the following.

Computing Floquet forms becomes tedious for large degrees of freedom systems since the time-periodic modes require an extra dimension to be computed: the harmonics used to decompose the system in the frequency domain. The number of harmonics  $H$  used increases the size of the eigenvalue problem to be solved with  $2H + 1$ . The fewer the degrees of freedom in the original system, the easier it is to compute the Floquet forms. Thus, a compromise has to be made between classic modal analysis, which leaves a small but coupled system of size  $2n$  in the state space, and Floquet form computation which is a problem of size  $2m$  that fully decouples this system.

Generalized eigensolver algorithms require a computational effort in the order of the number of entries  $l$  squared  $O(l^2)$  or cubed  $O(l^3)$  [82]. Therefore solving two relatively

small, successive eigenproblems, i.e. to obtain the matrix  $\mathbf{X}$  and the periodic eigenfunctions  $\mathbf{w}(t)$  through the Hill matrix, is cheaper than solving one big Hill matrix at once. The introduction of a pre-modal transformation is advantageous because the Hill eigenproblem takes less computational effort and there are less spurious Floquet forms to sort through.

## 4.2 Free vibration

In dynamic analysis we often want to find the free vibrating response of a structure. Without excitation, many important properties such as stability and principal motions are revealed.

### 4.2.1 Floquet form computation and visualisation

Before projecting on Floquet Forms, one needs to compute them. This numerical process has been fully expressed in chapter 3 where it has been applied to the Ziegler column. The computation of Floquet Forms is performed on the homogenous part of the time-periodic equation of motion which, in our case, is the reduced set of modal equations in the state space (4.5), in the typical form

$$\mathbf{J}_B \dot{\mathbf{y}}(t) = \mathbf{J}_A(t) \mathbf{y}(t), \quad (4.8)$$

with

$$\mathbf{J}_B = \begin{bmatrix} \mathbf{0} & \mathbf{I} \\ \mathbf{I} & \mathbf{0} \end{bmatrix} \quad \text{and} \quad \mathbf{J}_A(t) = \begin{bmatrix} (-\lambda \hat{\mathbf{K}}_c \cos(\beta t) - \omega_0^2) & \mathbf{0} \\ \mathbf{0} & \mathbf{I} \end{bmatrix}.$$

Computing the Floquet Forms  $\mathbf{y}_m(t) = \mathbf{p}_m(t) e^{s_m t}$  from the Hill matrix of equation (4.8) is similar to doing it on equation  $\dot{\mathbf{y}}(t) = \mathbf{J}(t) \mathbf{y}(t)$  of chapter 3 albeit with a few differences which are explained in appendix B.

As usual, for a given number of retained harmonics  $H$ , solving the spectrum of the square  $2n(2H + 1)$ -dimensional Hill matrix gives us  $2n$  FFs of which of which  $2m$  are retained. The Floquet exponents  $s_m$  associated with their periodic eigenvectors  $\mathbf{p}_m(t)$  which are decomposed in the frequency domain following  $\mathbf{p}_m(t) = \mathbf{p}_m^0 + \sum_{h=1}^H \mathbf{p}_{mc}^h \cos(h\beta t) + \mathbf{p}_{ms}^h \sin(h\beta t)$ . This real Fourier decomposition results in time independent vectors  $\mathbf{p}_m^0$ ,  $\mathbf{p}_{mc}^h$  and  $\mathbf{p}_{ms}^h$  that are the deformed shapes of the  $m^{\text{th}}$  Floquet Form on each harmonic.

To give an example of Floquet Forms in the case of our cantilever beam discretized by finite elements, we computed the three first Floquet Forms of the homogeneous part of the finite element system (4.2) with  $N = 1380$  degrees of freedom and  $H = 40$  for a low-frequency case (as it was shown in section 3.4.3, this case is interesting because by slowly modulating the system, many frequencies become significant in the Floquet Forms). Because it would be too costly to compute the spectrum of the  $2N(2H + 1)$  square Hill matrix in state space, the time-periodic system (4.2) is projected on a basis

of  $n = 32$  classic harmonic eigenmodes in the physical space ( $2n = 64$  modes in the state space) leading to a reduced time-periodic set of equations in the form (4.8). The system's periodicity is chosen 2,5% of the natural frequency  $\omega_1 = 14.46$  rad/s so that  $\beta = 0.025\omega_1$ . The scaling factor of the critical geometric stiffness is chosen to be  $\lambda = 0.25$  which corresponds to one fourth of the buckling load. Recall also that to obtain (4.8), the physical equations of motion were projected on classic modes, before being projected on Floquet Forms. Therefore the physical  $N$ -dimensional displacement is computed as in (4.7) by  $\mathbf{x}(t) = \mathbf{X}\mathbf{w}(t)\mathbf{r}(t)$ .

In Fig.4.2 an overview of the first Floquet Form eigenfunction  $\mathbf{p}_1(t) = \mathbf{p}^0 + \sum_{h=1}^{40} \mathbf{p}_c^h \cos(h\beta t) + \mathbf{p}_s^h \sin(h\beta t)$  is plotted. The amplitudes shown are the norms  $|\mathbf{p}^h|$  normalized by the maximum norm  $|\mathbf{p}_s^3|$ . The amplitudes show what frequencies play the most important role. Up until the eighth harmonic there are amplitude norms more than 1% of the maximum norm  $|\mathbf{p}_s^3|$ . The norms decrease with the increasing harmonics and above the twentieth harmonic, the harmonic components do not have significant amplitudes and are within machine precision  $10^{-14}$ .

The different amplitudes are reflected in the shapes per harmonic. The FF-shapes are plotted up to the third harmonic, since all shapes up to the twentieth harmonic are similar. Each shape is similar to the first bending mode of a beam. In fact, the spatial shapes of the Floquet Forms are rarely (see remark at the end of this subsection) different from the classic shapes of the harmonic eigenmodes because the fundamental frequency of the Floquet form, or Floquet exponent, is really closed to the first harmonic frequency obtained by classic modal analysis. It is interesting to note that computing the first Floquet Form (and the others) from the pre-projected equation (4.5) or doing it directly on the physical equations (4.2) lead to the same results. But again, the pre-projection method spares a lot of computation time.

Fig. 4.3 illustrates the second Floquet Form. There are many significant low frequency amplitudes. The distribution of amplitudes is different than in case of FF1, but again after the eighth harmonic the amplitudes decrease exponentially, which suggest a correct convergence of the computed fundamental Floquet Forms. After the twentieth harmonic there is no more significant amplitude. The shapes of the Floquet Form are similar to the second bending mode with the third sine component  $\mathbf{p}_s^3$  being again the maximum.

Fig.4.4 shows an overview of the third Floquet Form. The amplitudes figure shows the constant component is the largest one and that with increasing harmonics, the amplitudes decay rapidly. This time, the Floquet Form is an axial vibrational mode whose shape is very close to the classic axial mode shown in section 2.4.

A possibly interesting feature of the shown Floquet Forms is that for higher modes and higher harmonics, it seems that the shapes of periodic eigenfunctions  $\mathbf{p}_m(t)$  are no longer similar at different frequencies. For example, the constant component of fig.4.4 corresponds to an axial elongation whereas the components  $\mathbf{p}_c^1$ ,  $\mathbf{p}_c^3$  and  $\mathbf{p}_s^2$  resemble three node bending instead of an axial mode. How valid is the hypothesis that these odd shapes are due to physics and not to a numerical artifact? These odd shapes have small amplitudes in the order of  $10^{-4}$  to  $10^{-6}$  relative to the maximum amplitude. However the shapes of the first and second Floquet Forms (apart from  $\mathbf{p}_c^3$ ) remain similar even when

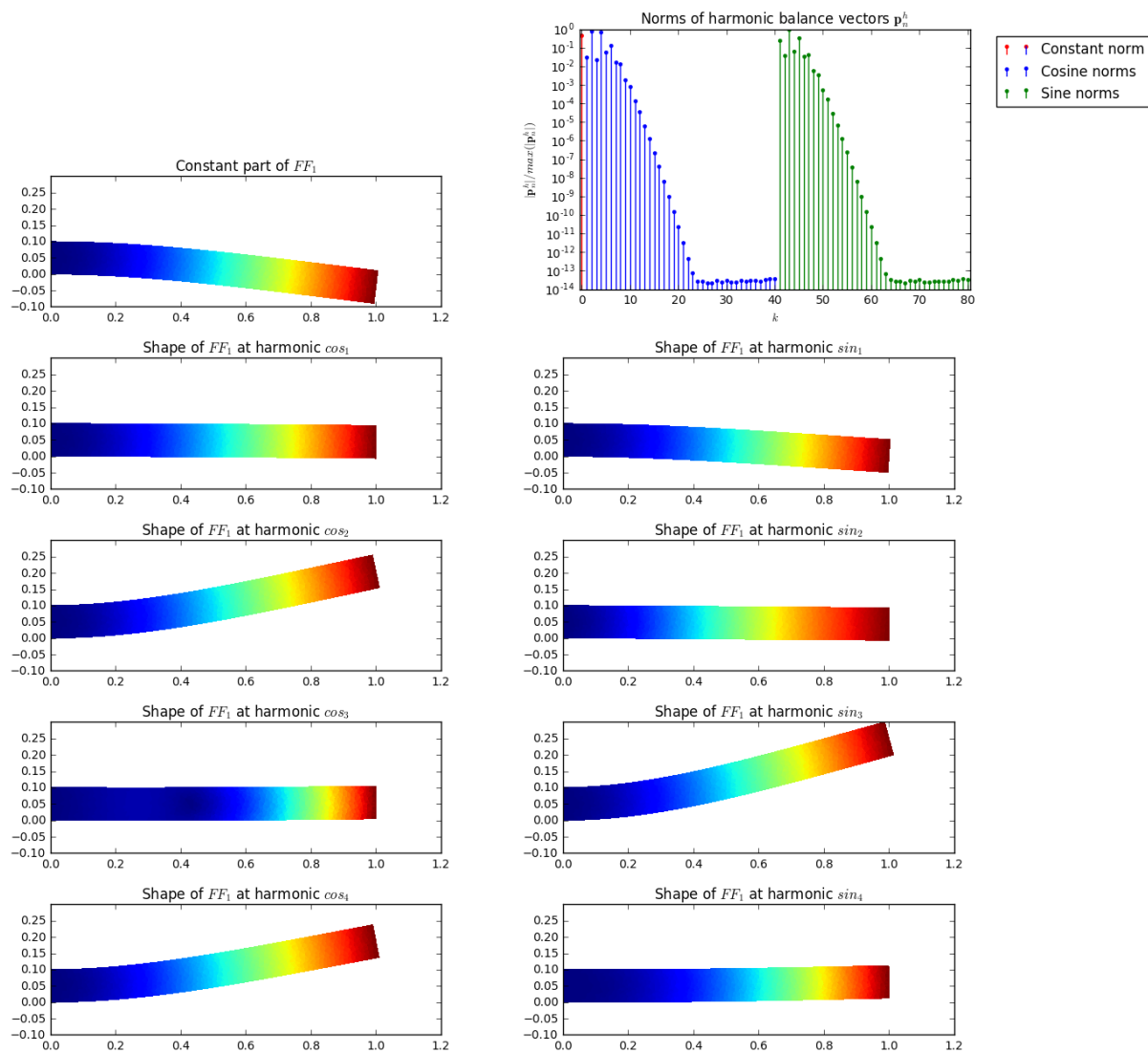


Figure 4.2: Overview of first linearly independent Floquet form shapes per harmonic for  $\lambda = 0.25$  and  $\beta = 0.025\omega_1$ . The computed Floquet exponent for this mode is  $s_1 = 0 + i17.6$ , i.e. a fundamental frequency of 17.6 rad/s. The amplitudes shown are  $\mathbf{p}_1(t) = \mathbf{p}^0 + \sum_{h=1}^{40} \mathbf{p}_c^h \cos(h\beta t) + \mathbf{p}_s^h \sin(h\beta t)$ . In the amplitude figure the constant norm  $|\mathbf{p}^0|$  is plotted in red, the cosine amplitudes  $|\mathbf{p}_c^h|$  are plotted in blue and the sine amplitudes  $|\mathbf{p}_s^h|$  are plotted in green. The constant  $\mathbf{p}^0$ , cosine  $\mathbf{p}_c^h$  and sine  $\mathbf{p}_s^h$  deformation shapes are plotted up to the fourth harmonic. These shapes are normalized relative to the largest norm in the system  $|\mathbf{p}_s^3|$ .

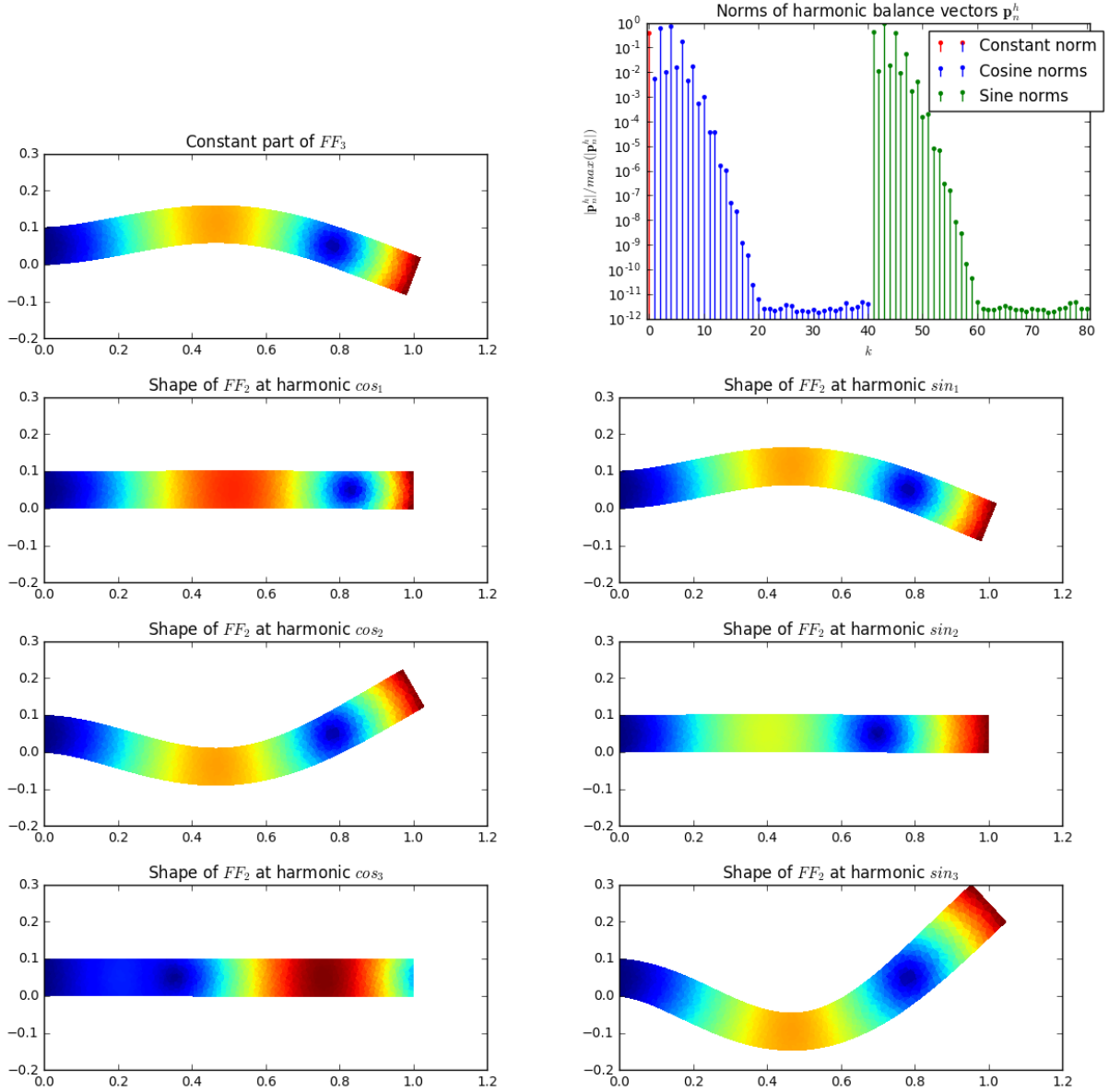


Figure 4.3: Overview of second Floquet form per harmonic for  $\lambda = 0.25$  and  $\beta = 0.025\omega_1$ . The computed Floquet exponent for this mode is  $s_2 = 0 + i105.66$ , i.e. a fundamental frequency of 105.66 rad/s. The amplitudes shown are  $\mathbf{p}_2(t) = \mathbf{p}^0 + \sum_{h=1}^{40} \mathbf{p}_c^h \cos(h\beta t) + \mathbf{p}_s^h \sin(h\beta t)$ . In the amplitude plot the constant norm  $|\mathbf{p}^0|$  is plotted in red, the cosine amplitudes  $|\mathbf{p}_c^h|$  are plotted in blue and the sine amplitudes  $|\mathbf{p}_s^h|$  are plotted in green. The constant  $\mathbf{p}^0$ , cosine  $\mathbf{p}_c^h$  and sine  $\mathbf{p}_s^h$  deformation shape are plotted up to the third harmonic. These shapes are normalized relative to the largest norm in the system  $|\mathbf{p}_s^3|$ .

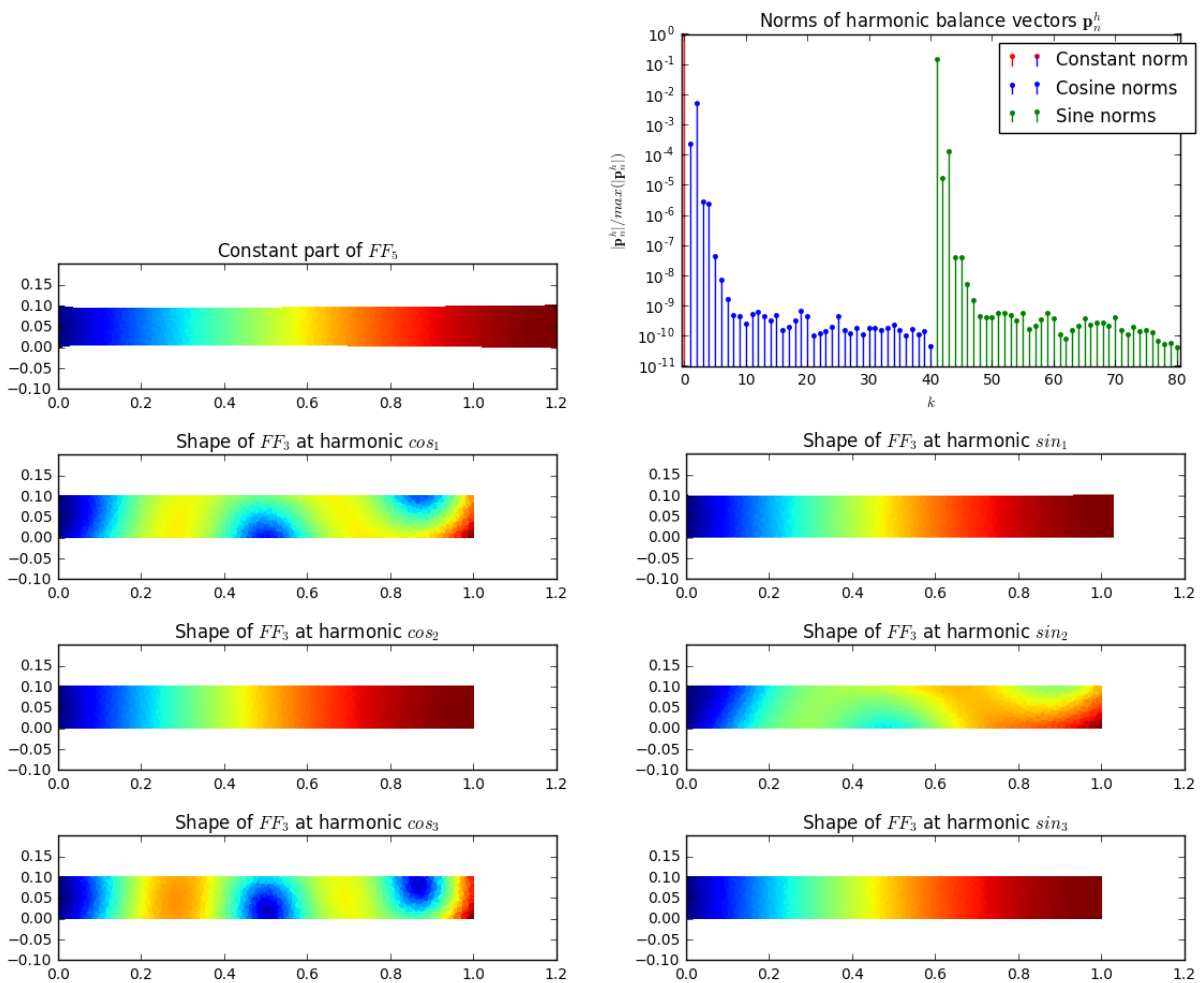


Figure 4.4: Overview of the third Floquet form shapes per harmonic for the parameters  $\lambda = 0.25$  and  $\beta = 0.025\omega_1$ . The computed Floquet exponent for this mode is  $s_3 = 0 + i270.99$ , i.e. a fundamental frequency of 270.99 rad/s. In the amplitude figure the constant norm  $|\mathbf{p}^0|$  is plotted in red, the cosine amplitudes  $|\mathbf{p}_c^h|$  are plotted in blue and the sine amplitudes  $|\mathbf{p}_s^h|$  are plotted in green.

the norms drop to  $10^{-10}$ . Furthermore increasing or decreasing the size of the Hill matrix did not change the results.

## 4.2.2 Projection on Floquet Forms

Time-periodic equations of motion can be transformed to time-independent equations by projecting them on Floquet forms. To project the reduced  $2n$ -dimensional time-periodic system shown in equation (4.5), the state vector  $\mathbf{y}(t)$  (we drop the capital letter in the following because we could do the Floquet Form expansion directly on the physical state vector  $\mathbf{y}(t)$  of (4.5)) is expanded in the Floquet forms  $\mathbf{y}(t) = \mathbf{p}(t)\mathbf{q}(t)$ . To transform the state derivative, the chain rule is used since both the amplitude of the Floquet Form,  $\mathbf{q}(t)$ , and its eigenfunction,  $\mathbf{p}(t)$ , are time dependent:

$$\dot{\mathbf{y}}(t) = \dot{\mathbf{p}}(t)\mathbf{q}(t) + \mathbf{p}(t)\dot{\mathbf{q}}(t). \quad (4.9)$$

Replacing expression (4.9) in the homogeneous part of the state space equation (4.5) that is given in (4.8), one gets the expression:

$$\mathbf{p}^T(t)\mathbf{J}_B\mathbf{p}(t)\dot{\mathbf{q}}(t) - \mathbf{p}^T(t)[\mathbf{J}_A(t)\mathbf{p}(t) - \mathbf{J}_B\dot{\mathbf{p}}(t)]\mathbf{q}(t) = 0. \quad (4.10)$$

Premultiplying equation (4.10) by  $(\mathbf{p}^T(t)\mathbf{J}_B\mathbf{p}(t))^{-1}$  gives

$$\dot{\mathbf{q}}(t) = (\mathbf{p}^T(t)\mathbf{J}_B\mathbf{p}(t))^{-1}\mathbf{p}^T(t)[\mathbf{J}_A(t)\mathbf{p}(t) - \mathbf{J}_B\dot{\mathbf{p}}(t)]\mathbf{q}(t). \quad (4.11)$$

The equation (4.11) has several time dependent coefficients which are periodic but it turns out this expression will greatly simplify. It is known from chapter 3 that the amplitude of a time-periodic homogeneous problem writes  $\mathbf{q}(t) = \mathbf{q}_0 e^{\mathbb{S}t}$  where the matrix  $\mathbb{S}$  is a diagonal matrix containing the Floquet exponents. The derivative of this solution is easily found:  $\dot{\mathbf{q}}(t) = \mathbb{S}\mathbf{q}_0 e^{\mathbb{S}t} = \mathbb{S}\mathbf{q}(t)$ . Using this homogeneous solution in (4.11) we obtain the following result:

$$\mathbb{S}\mathbf{q}(t) = (\mathbf{J}_B\mathbf{p}(t))^+ [\mathbf{J}_A(t)\mathbf{p}(t) - \mathbf{J}_B\dot{\mathbf{p}}(t)]\mathbf{q}(t), \quad (4.12)$$

where we use the fact that  $\mathbf{p}^T(t)^{-1}\mathbf{p}^T(t) = \mathbf{I}$  and where  $(\ )^+$  denotes the Moore-Penrose pseudo inverse. By removing the amplitude of the Floquet Form,  $\mathbf{q}(t)$ , from the left and right hand sides of the equation (4.12), we arrive at a new expression for the matrix of Floquet exponents (4.13):

$$\mathbb{S} = (\mathbf{J}_B\mathbf{p}(t))^+ [\mathbf{J}_A(t)\mathbf{p}(t) - \mathbf{J}_B\dot{\mathbf{p}}(t)]. \quad (4.13)$$

The matrix  $\mathbb{S}$  on the left hand side of (4.13) is a constant, diagonal matrix with Floquet exponents for entries. The time-periodic matrix functions on the right hand side of (4.13) therefore have to result in a constant, diagonal Floquet exponent matrix as well. Figure 4.5 shows the time evolution of the entries of the matrix obtained by time integration of  $(\mathbf{J}_B\mathbf{p}(t))^+ [\mathbf{J}_A(t)\mathbf{p}(t) - \mathbf{J}_B\dot{\mathbf{p}}(t)]$  (blue line) as compared to the Floquet exponents of the first ten Floquet exponents (in red dotted lines) of the linear equation of motion in state

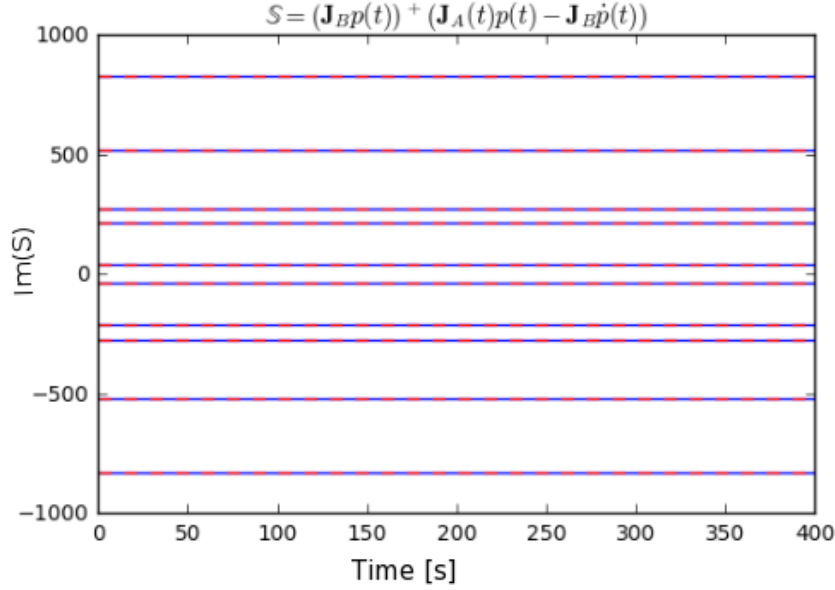


Figure 4.5: Imaginary part of the first ten entries of matrix  $(\mathbf{J}_B \mathbf{p}(t))^+ [\mathbf{J}_A(t) \mathbf{p}(t) - \mathbf{J}_B \dot{\mathbf{p}}(t)]$  (in blue lines) and first ten Floquet exponents ( $\Im(\mathbf{s}_m)$ ) in red dotted lines.

space (4.8). The values are constant and perfectly coincide. This is a numerical proof that the homogeneous time periodic ODE (4.8) can be rewritten as an ODE with constant coefficients. A mathematical demonstration of this can be found in the very interesting paper of Calico et al. [39]. When projected on Floquet Forms, a coupled set of time-periodic equations can become uncoupled and eventually reduced. Floquet Forms are a complete orthonormal basis in space and time and greatly simplify the physics underlying the free vibrations of a structures in periodic state.

In summary, when projecting the solution  $\mathbf{y}(t)$  on a basis of Floquet Forms,  $\mathbf{y}(t) = \mathbf{p}(t)\mathbf{q}(t)$ , the reduced time-periodic equation in the state space,  $\mathbf{J}_B \dot{\mathbf{y}}(t) = \mathbf{J}_A(t)\mathbf{y}(t)$ , already given in (4.8) can be recast in the form of a time-independent uncoupled equation:

$$\dot{\mathbf{q}}(t) - \mathbb{S}\mathbf{q}(t) = \mathbf{0}, \quad (4.14)$$

where the diagonal Floquet exponent matrix  $\mathbb{S}$  is known as it is the Floquet exponents computed in the previous subsection. The solutions of equation (4.14) are straightforward and read  $\mathbf{q}_h(t) = \mathbf{q}_0 e^{\mathbb{S}t}$  where  $\mathbf{q}_0$  is the Floquet Form amplitude given by the initial conditions for the free vibration of the beam. This means that Floquet forms solve the free vibration problem algebraically. Instead of integrating the equations of motion over time. The reponse  $\mathbf{y}(t)$  is simply reconstructed when knowing the Floquet Forms eigenfunctions by the relation  $\mathbf{y}(t) = \mathbf{p}(t)\mathbf{q}_0 e^{\mathbb{S}t}$ . Note that equation (4.14) of original size  $2n$  could be further reduced by keeping only  $2m < 2n$  Floquet Forms in the free vibrational solution.

### 4.2.3 Numerical application

In this section we treat the free vibrational problem of the beam of Fig. 4.1 discretized by finite elements in the Fenics Software. The number of possible displacements is  $N = 36$  for the physical displacement since there are 18 nodes with  $x$  and  $y$  displacements in

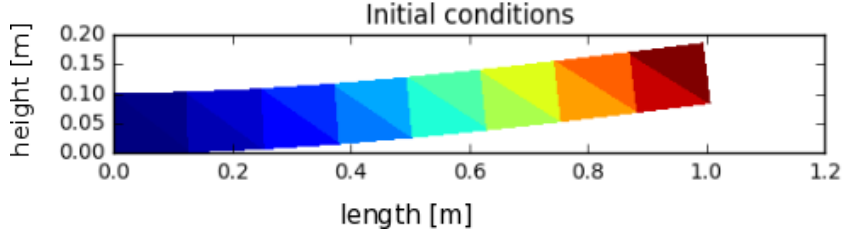


Figure 4.6: The initial conditions of the case analyzed with  $N = 32$  degrees-of-freedom. The beam is bent upwards and released as shown in the deformed configuration. The free vibratory response will be computed by either Floquet forms reconstruction or classic direct time integration in the full physical basis.

2D. Two nodes on the left hand side are clamped. Therefore there are  $N = 32$  degrees of freedom in the interior domain which do not have an imposed displacement (see Appendix ?? for more information). In state space there are  $2N = 64$  state variables, namely the displacements and velocities. Furthermore we take 5 harmonics into account in the Hill matrix so that the shape of the full Hill matrix is  $704 \times 704$ . The size of the mesh is kept small because we will project the free vibration on Floquet Forms that are computed directly from the homogeneous part of the equation of motion (4.2) in the state space, that is not projected a priori on a classic modal basis.

Fig.4.6 shows the initial conditions of the beam that we consider. There is no force applied, only an initial displacement. For a free vibration case, there is no excitation, the response is only caused by initial disturbances. Such a system is modeled with the homogeneous part of the equation of motion (4.2). This equation can be solved by direct numerical integration or by the Floquet Form projection explained in the previous subsection where only one eigenvalue problem has to be solved. Note that with projection, there is only one eigenvalue problem to solve, the other operations are just multiplications for reconstruction of the physical response following  $\mathbf{x}(t) = \mathbf{w}(t)\mathbf{r}(t)$  as expressed in (4.7), whatever the initial conditions, albeit for time integration, each different initial condition requires a numerical integration in time.

Fig.4.7 shows the response of the tip of the periodically pre-stressed free-vibrating beam over time. The displacement and velocity in vertical direction are shown with increasing number of Floquet forms. The response, computed by integrating the equations of motion over time in red are compared to the solution obtained by algebraic reconstruction on a basis of Floquet forms shown in blue. First of all, when using only 2 Floquet forms, both the displacement (Fig.4.7 a) and velocity (Fig.4.7 b) are not close to the reference solution: the solution is not converged enough, more Floquet forms are needed since they do not form a proper orthogonal basis for the free vibratory response. When using 6 Floquet forms, the displacement seems converged (Fig.4.7 c), however the velocity misses a lot of small peaks (Fig.4.7 d). The general trends are captured well when using 6 Floquet forms, however there are high-frequency oscillations that are not well approximated. Finally, by using 32 Floquet forms, which is half of the total number of Floquet Forms that is  $2N = 64$ , both the displacement (Fig.4.7 e) and velocity (Fig.4.7 f) seem converged.

Comparing the solutions in Fig.4.7, we see that accuracy increases by increasing the

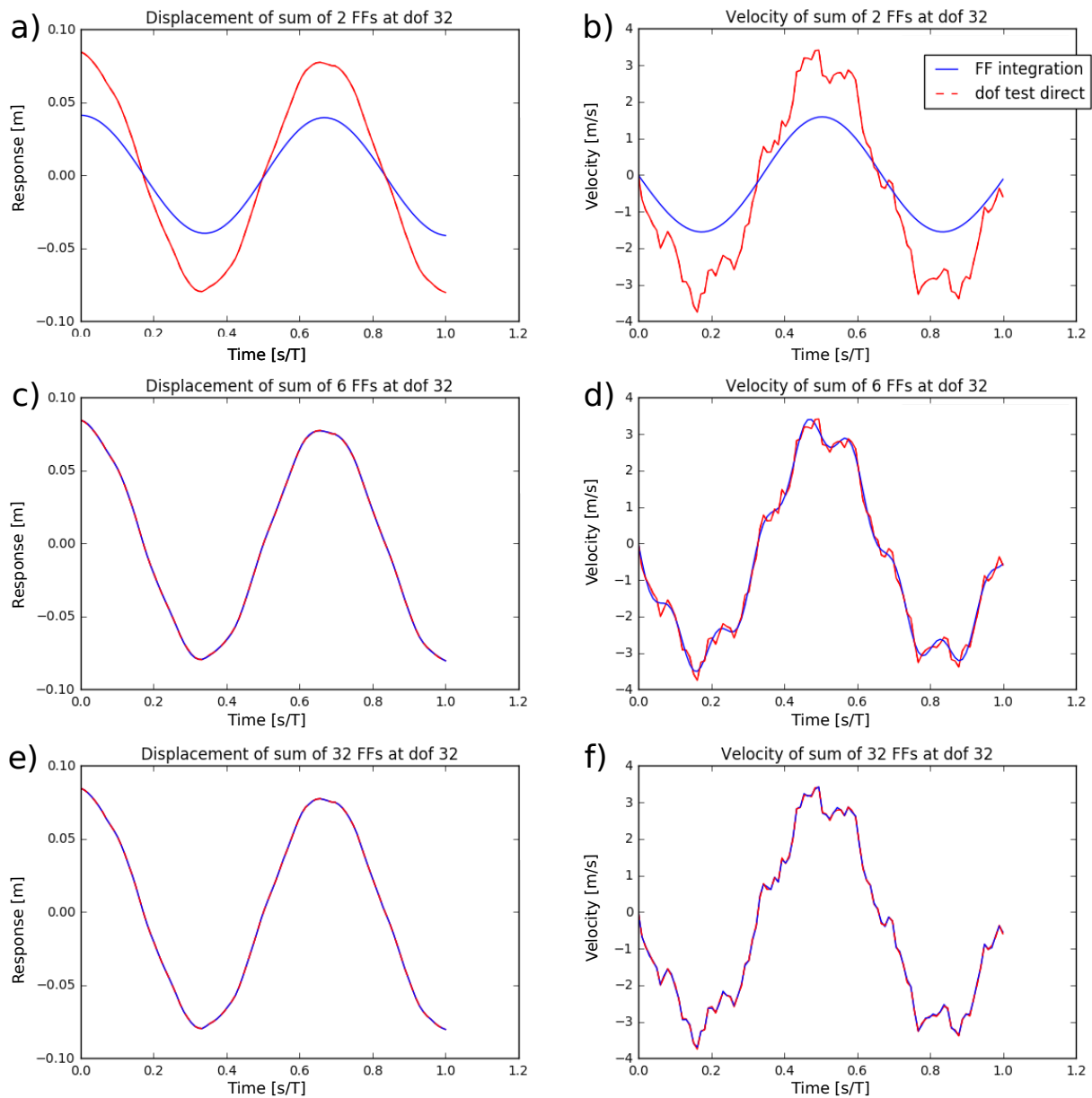


Figure 4.7: Response reconstruction with increasing number of Floquet forms for the modulation parameters  $\lambda = 0.25$  and  $\beta = 0.025\omega_1$  and a harmonic truncation number  $H = 5$ . The response shown is the vertical displacement and velocity of a node at the beam tip. The FF-reconstruction is the sum of all FF contributions over time  $\mathbf{y}(t) = \sum_{m=1}^M \mathbf{p}_m(t)q_m(t)$ . The FF-reconstruction is shown in blue, the direct computation of the response is in red for reference. a) Displacement using 2 FFs. b) Velocity using 2 FFs. c) Displacement using 6 FFs. d) Velocity using 6 FFs. e) Displacement using 32 FFs. f) Velocity using 32 FFs.

number of Floquet forms. High frequency content in the free vibrational response is better approximated with increasing number of Floquet forms. To validate quantitatively this modal convergence, a more objective measure for the error between the direct-integration and the Floquet forms reconstruction is used that is shown in Fig.4.8. The error is taken as the difference between the directly integrated solution ( $\mathbf{y}_d(t)$ ) and the Floquet computations ( $\mathbf{y}_{FF}(t)$ ). To be more precise, the Euclidian norm of the difference between the Floquet form response and direct response is computed at the end of one period:  $|\mathbf{y}_{FF}(T) - \mathbf{y}_d(T)|/|\mathbf{y}_d(T)|$ . This norm is normalized by the direct response. We see from Fig.4.8 that is plotted in log-log, that the convergence is almost quadratic, showing that projecting a free vibratory response of a structure in periodic state on the basis of its Floquet Form is efficient.

Moreover, in figure 4.9 the CPU time is shown as a function of the number of Floquet forms we kept in the basis. The CPU time has been normalized by the time required for direct integration. We see that reconstructing the free vibration with Floquet forms takes much less time than using direct time integration. The more the number of Floquet forms in the basis, the longer the CPU time (the CPU time evolves with a power 0.63 which is relatively small as compared to time integration) but even with the full basis of Floquet forms, i.e.  $2m = 64$ , the CPU time is hundredth time smaller than performing a direct time integration. Of course the reason is that, apart from the original hill eigenvalue problem to solve, the Floquet modal solution is an exact algebraic formulation that does not even require time integration. Floquet forms projection could therefore be used as a modal reduction technique for large set of discrete time-periodic ODEs that could emerge in engineering.

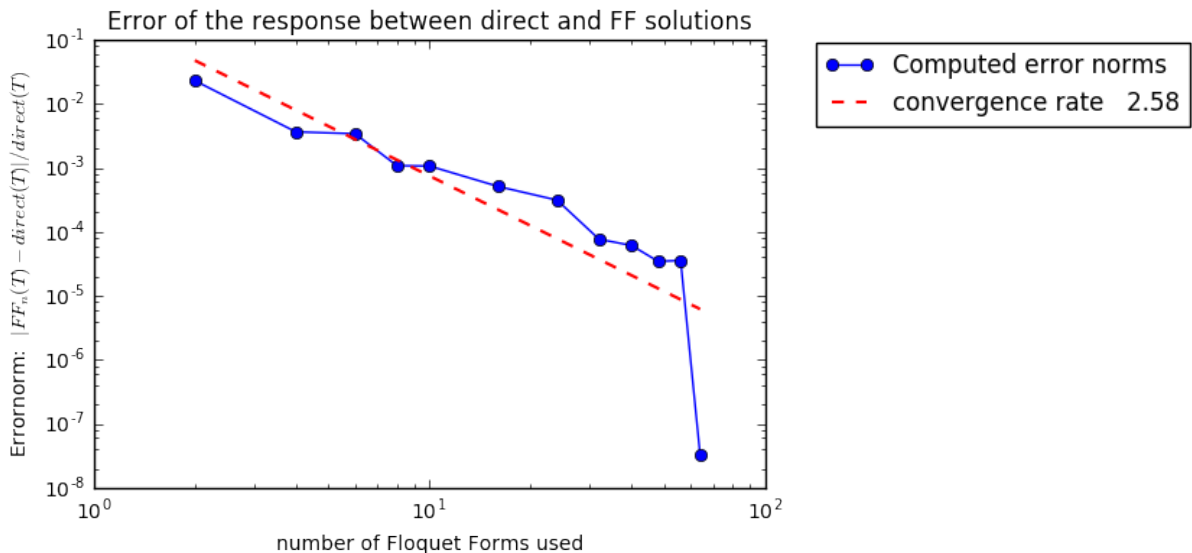


Figure 4.8: Convergence of the physical response error norm. The error norm is defined as  $|\mathbf{y}_{FFn}(T) - \mathbf{y}_d(T)|/|\mathbf{y}_d(T)|$ . Where the total displacement after one period by FFs and direct computation are noted as  $\mathbf{y}_{FFn}(T)$  and  $\mathbf{y}_d(T)$  respectively. The error norm is computed by integrating the equations of motion projected on Floquet forms (blue). The case investigated is the free-vibrating beam with 16 nodes in the interior domain (18 in total).

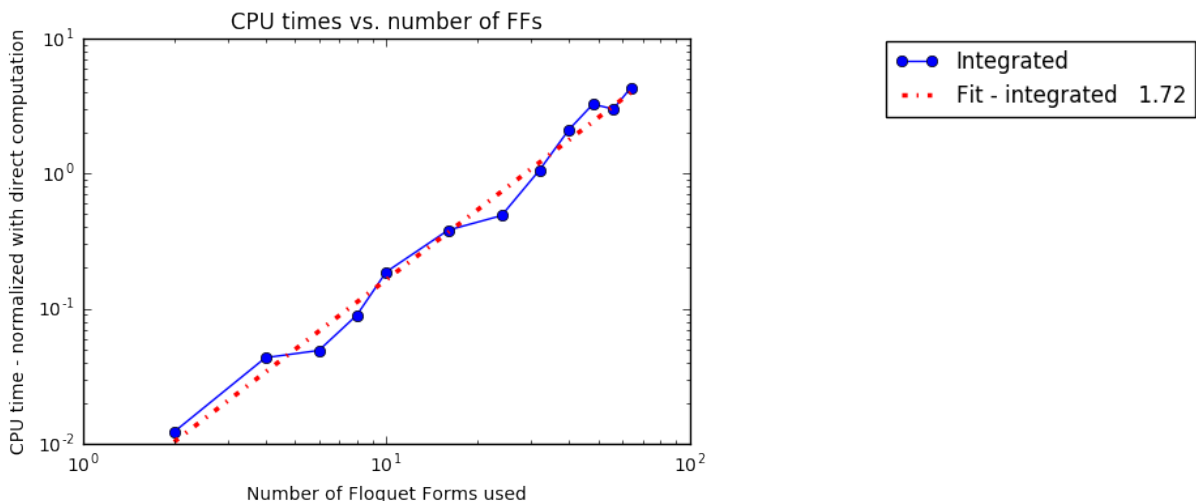


Figure 4.9: CPU time as a function of the number of Floquet forms used. The CPU time is measured by using either the exact homogeneous solution (blue) or by integrating the equations of motion projected on Floquet forms (green). The CPU time has been normalised by the time required for direct integration. The case investigated is the homogeneous beam.

## 4.3 Forced vibrations of time-periodic systems

### 4.3.1 Projecting the force vector

In section 4.2, the homogeneous time-periodic equations of motion were reformulated in a set of reduced time-independent uncoupled equation by projection on an orthogonal basis of Floquet forms. However, the analyzed equations were for a system vibrating freely. In case of excitation on the system, the response in steady state is of interest. The particular solution of the non-autonomous equations of motion given in (4.1) in the physical space and (4.2) in state space, this is what corresponds mathematically to the steady state response. This solution will be computed by projecting those equations, as well as the force term on the Floquet forms. The particular solutions reveal what vibrations to expect in response to excitation. Therefore, physical insights in the forced vibrations is a necessity for analysis of the system in operating conditions. With the stationary response patterns known, a structural engineer can evaluate whether time-periodic vibratory systems fulfill requirements.

If forcing is taken into account, not only the homogeneous part of the equation of motion is projected as in (4.10) but the applied force  $\mathbf{p}^T(t)\mathbf{F}(t)$  also is pre-multiplied by the quantity  $(\mathbf{p}^T(t)\mathbf{J}_B\mathbf{p}(t))^{-1} = \mathbf{Q}(t)$ . The latter formulation is used because only a  $2m$  by  $2m$  system needs to be inverted, instead of the larger  $2n \times 2m$  Moore-Penrose inverse  $(\mathbf{J}_B\mathbf{p}(t))^+$  which was used in section 4.2.2. Taking into account external forcing, the  $2m$  dimensional uncoupled homogeneous equation (4.14) takes the general form

$$\dot{\mathbf{q}}(t) - \mathbb{S}\mathbf{q}(t) = \mathbf{Q}(t)\mathbf{p}^T(t)\mathbf{F}(t). \quad (4.15)$$

Note that equation (4.15) has a time-dependency on the right hand side whereas the left hand side is time independent and uncoupled. This equation is used to compute the

Floquet forms particular modal amplitude  $\mathbf{q}(t)$  in the following.

To compute the particular solution we need to understand the right hand side of the equation of motion (4.15). When there is an excitation applied, the right hand side determines the stationary response. On the long term, the system's response is determined by its stationary response since in most practical cases, the transient response due to initial conditions dampens out. On the right hand side of equation (4.15), we have a force vector  $\mathbf{F}(t)$  that is pre-multiplied with a time periodic term. To illustrate with an example: if there is a constant force vector applying on the cantilever beam in a time-periodic elastic state, then this vector is pre-multiplied with a periodic term on the right-hand side of equation (4.15) once projected on the basis of Floquet forms, i.e. the resulting vector is time-periodic. Therefore the steady state response to this constant force will be time periodic. That a constant force entails a periodic response is an increase in complexity that sets of linear ODEs with constant coefficients do not have.

It is interesting to note that both  $\mathbf{Q}(t) = \left(\mathbf{p}^T(t)\mathbf{J}_B\mathbf{p}(t)\right)^{-1}$  and  $\mathbf{p}^T(t)$  are  $T$ -periodic functions where  $T$  is the period of the elastic state (with fundamental frequency  $\beta = 2\pi/T$ ) so that multiplying both quantities give a periodic quantity as well.  $\mathbf{Q}(t)$  is a row vector matrix of size  $2m \times 2m$ , where each row corresponds to a specific Floquet form of size  $2m$ .  $\mathbf{p}^T(t)$  is a rectangular matrix of size  $2m \times 2n$  or  $2m \times 2N$  depending if the vector of external forces is expressed in the reduced classic modal state space  $2n$  or physical state space  $2N$ . Since the  $2m$ -dimensional equation of motion (4.15) is uncoupled on the left hand side, the value of  $\hat{\mathbf{F}}(t) = \mathbf{Q}(t)\mathbf{p}^T(t)\mathbf{F}(t)$  determines the Floquet form amplitude of the particular solution  $\mathbf{q}(t)$ . In engineering terms, the steady state of the system  $\mathbf{q}(t)$  is determined by the projected force.

The difficulty of computing  $\mathbf{Q}(t)$  is finding the inverse of the eigenfunction  $\mathbf{p}^{-1}(t)$ . There is no simple transformation from the periodic eigenfunction  $\mathbf{p}(t) = \sum_h \mathbf{p}^h e^{ih\beta t}$  to its inverse. One could integrate the inverse eigenfunction over time and apply Fourier analysis to compute the inverse eigenfunction in the frequency domain. Another, more elegant solution might be to use the technique described by Calico [39]. They describe how the inverse eigenvectors of the STM can be computed over time by directly computing solutions to the adjoint eigenproblem.

### 4.3.2 Example of a harmonic external force

The particular solution due to a harmonic external force,  $\mathbf{F}(t) = \mathbf{F}_A \sin \Omega t$ , is investigated. For this scenario, the number of degrees of freedom are  $N = 360$  in the physical space but the system is reduced on a classic basis of 32 physical harmonic eigenmodes (64 eigenmodes in the state space). In equation (4.15) of dimension  $2m$  where  $2m$  is the number of retained Floquet forms,  $\mathbf{F}(t)$  is therefore of size  $2n = 64$ . According to the previous subsection, when projected, the harmonic force  $\hat{\mathbf{F}}(t)$  becomes almost-periodic for structures in time-periodic elastic states and the particular solution is therefore almost-periodic. The particular response is computed either by integrating the eventually reduced and uncoupled equation (4.15) that has been projected on  $2m$  Floquet forms. The obtained results are validated by direct integration of the time-periodic modal equations of

motion shown in equation (4.5). We will see that with an increasing number of Floquet forms in the basis, the computed particular response will be more accurate.

The limitation though, comparing to the computation of the free vibrations on Floquet forms, is that there is not an exact solution easily available since there is no algebraic formulation of eigenvector inverse  $\mathbf{p}^{-1}(t)$ . For the moment, we still need to numerically integrate equation (4.15) since we have no closed form solution of the inverse of  $\mathbf{p}^{-1}(t)$ , notably in the frequency domain. This is a computationally costly operation that we would like to solve but finding the Fourier series of an inverse periodic function for which we know its Fourier series is still, we believe, an open problem.

The equation of motion of the system under periodic excitation is

$$\dot{\mathbf{q}} - \mathbb{S}\mathbf{q} = \mathbf{Q}(t)\mathbf{p}^T(t)\mathbf{F}_A \sin \Omega t. \quad (4.16)$$

The almost-periodic Right Hand Side (RHS) of (4.16) with modulation frequency  $\beta = 1.5\omega_1$ , elastic modulation amplitude  $\lambda = 0.5$ , excitation frequency  $\Omega = 2.9\omega_1$  and amplitude  $\mathbf{F}_A = 500$  N. The envelopes are found with the amplitude and projections  $\mathbf{Q}(t)\mathbf{p}^T(t)\mathbf{F}_A$ .

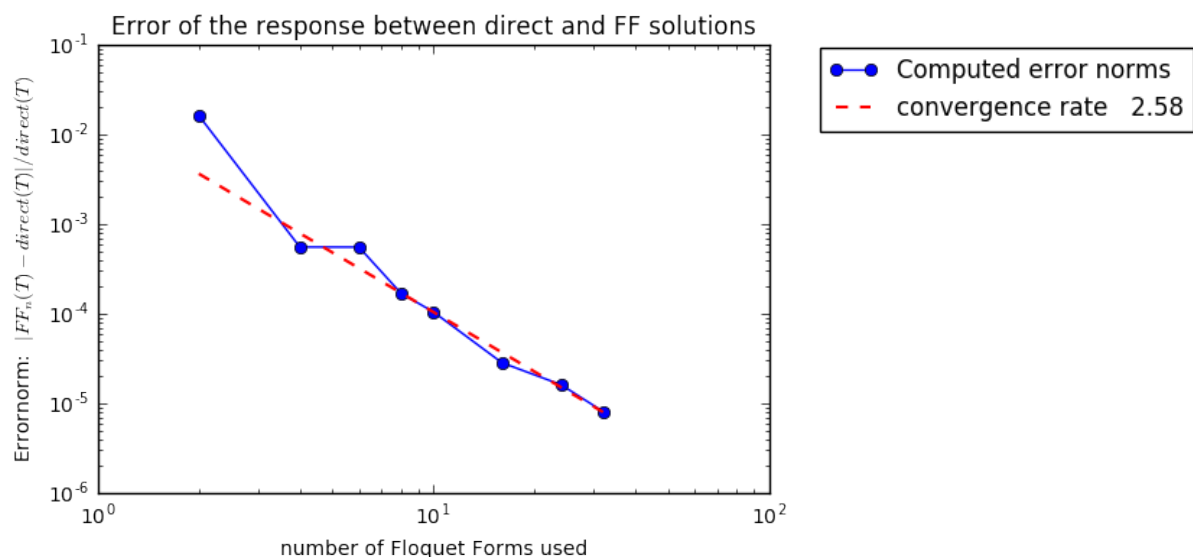


Figure 4.10: Convergence of the physical response error norm of a forced periodic beam under periodic prestress. The errornorm is defined as  $|\mathbf{y}_{FFn}(T) - \mathbf{y}_d(T)|/|\mathbf{y}_d(T)|$  where the total displacement after one period obtained by Floquet forms reconstruction and direct computation are noted as  $\mathbf{y}_{FFn}(T)$  and  $\mathbf{y}_d(T)$ , respectively. The errornorm is computed by integrating the equations of motion projected on Floquet forms. The case investigated is the forced beam under a sinusoidal load with excitation frequency  $\Omega = 2.9\omega_1$  and amplitude  $\mathbf{F}_A = 500$  N. The periodic prestress of the beam has the parameters frequency  $\beta = 0.025\omega_1$  and amplitude  $\lambda = 0.25$ .

In Fig.4.10 the errornorm is plotted as a function of number of Floquet forms that are kept in the orthonormal basis. The L2 norm between numerical time integration of the equation projected on Floquet forms and the original modal equation,  $|\mathbf{y}_{FFn}(T) - \mathbf{y}_d(T)|/|\mathbf{y}_d(T)|$ , is computed and plotted with errornorm on the y-axis and number of Floquet forms on the x-axis For this problem the system converges well. A logarithmic

fit line is plotted in red. The slope of this line is 2,58 which indicates the exponential convergence rate. The convergence in itself shows that FF-integration can be used for forced problems. The error decreases with increasing number of FFs. However this comes at the cost of an increased computational effort which will be investigated next.

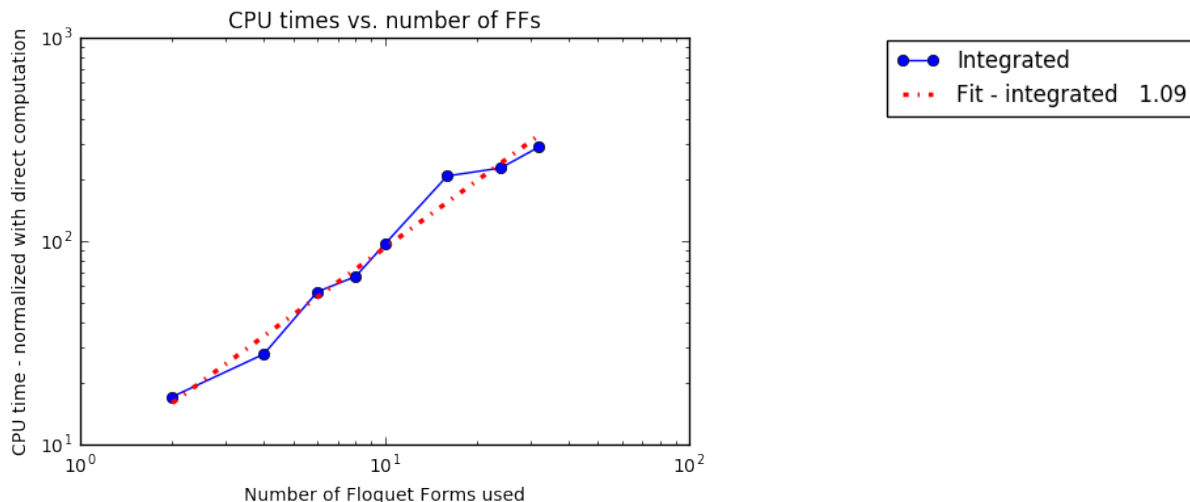


Figure 4.11: CPU time as a function of the number of Floquet forms used for the forced beam under a sinusoidal external load. The CPU time is measured when integrating the equations of motion projected on  $2m$  Floquet forms (4.15). The CPU time has been normalized by the time required for direct integration of the original  $2n = 64$ -dimensional equation.

In Fig.4.11 the computational time is plotted as a function of the number of Floquet Forms used on a logarithmic scale. The calculation time on the y-axis is normalized to the time needed for a direct integration of the original modal equation of motion. On the x-axis the number of Floquet forms are shown. As expected, the computational costs increase with increasing number of Floquet Forms in an almost linear fashion as illustrated by the power law with coefficient 1.09. Unfortunately, calculation time is higher than direct time integration because computing the projection matrix  $\mathbf{Q}(t)$  is costly since it requires an inversion at each time step. Floquet forms are shown to converge and therefore have a physical sense. Computing the stationary response takes more computational effort than direct integration. In the future these computations will be optimized if a more efficient method to project the force applied is found. If an algebraic formulation of the inverse of the periodic eigenfunction  $\mathbf{p}^{-1}(t)$  is found as Calico would suggest [39], computation time of the particular solution will be much lower than in Fig.4.11. Also, there is no need to invert  $\mathbf{Q}(t)$  on the full time domain since  $\mathbf{Q}(t)$  is periodic. Note also that an advantage of computation on Floquet forms is that  $\mathbf{Q}(t)$  is only dependent of the analyzed state, not on the external forces applied on this state. Thus, if  $\mathbf{Q}(t)$  has been computed for one modulated state, one can vary the external forces on it and there will be no need to recompute the inverse of  $\mathbf{Q}(t)$ , meaning the time integration would be much faster.

### 4.3.3 Frequency Response Spectrum

In this section the frequency response spectrum of the forced vibration of the time-periodic system is analyzed. This subsection is a follow up of section 2.4 and Fig.2.12 where the time-periodic system was projected on classic modes to compute the response in the frequency domain. Now that we have seen how to compute the stationary response using Floquet forms, another way to verify the projection method is to compare the particular responses obtained by projection and direct time integration of the modal equations in the frequency domain.

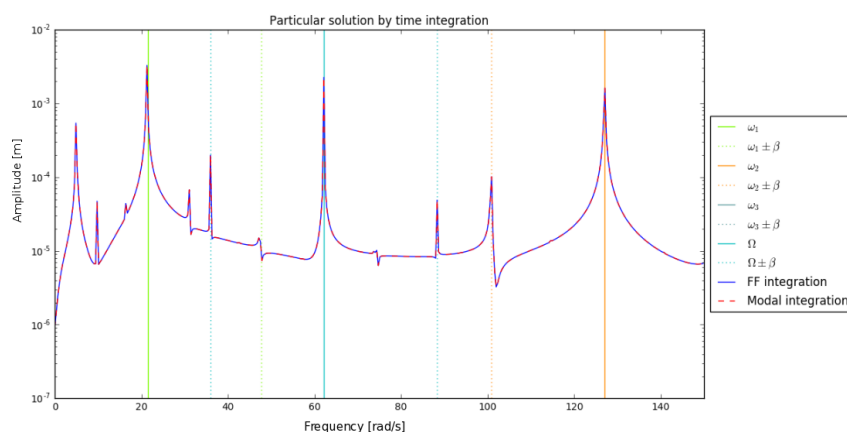


Figure 4.12: Fourier transform of the stationary response of the periodically prestressed beam under the harmonic external load. The Fourier transform has been made on 75 prestress periods and the number of retained Floquet forms is  $2m = 10$ . The computation are done either by integrating the equations projected on its FFs (blue) or by directly integrating the original modal equations (red). The natural frequencies are noted with  $\omega_i$ , with  $i = 1, 2, 3$ . The first subharmonics are shifted with  $\beta$  from natural and excitation frequencies and marked with dotted lines.

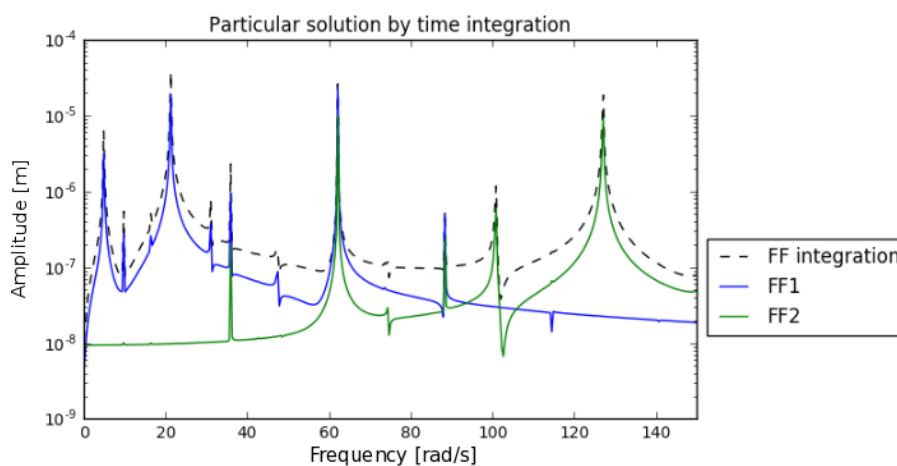


Figure 4.13: Fourier transform for the periodically prestressed beam under a harmonic external load decomposed per Floquet form. The first FF (blue) and second FF (green) are shown. For comparison, the frequency response spectrum of the total response is shown in black dotted lines.

In fig.4.12, the frequency response spectrum is computed using time-integration on a basis of Floquet forms. This is compared to integration performed on a basis of classic

harmonic eigenmodes (see fig.2.12). The results are in close agreement and show the effects of harmonic excitation on structures in time-periodic elastic state. Not only the natural frequencies, but also their subharmonics  $s_m \pm \beta$  are excited. When multiplying the periodic eigenfunctions  $\mathbf{p}(t) = \sum_h \mathbf{p}^h e^{ih\beta t}$  with a Floquet amplitude that has a specific frequency  $q(t) = q_0 e^{i\omega_j t}$ , this results in a almost-periodic response  $\mathbf{p}(t)q(t) = q_0 \sum_h \mathbf{p}^h e^{i(\omega_j + h\beta)t}$ . The exponential  $e^{i(\omega_j + h\beta)t}$  causes the linear forced vibrations to have sub-frequencies.

In fig.4.13, the stationary response contributions per Floquet forms are shown in the frequency domain. It is interesting to note that both Floquet forms respond on excitation frequency  $\Omega$  and its sub-harmonics  $\Omega \pm \beta$ . Apart from those resonating frequencies, the Floquet forms are uncoupled, i.e. the blue and green peaks are not mixed. This is very different from Fig.2.12 of section 2.4 where we were looking at the contributions of the forced vibration on each classic harmonic eigenmodes: the various sub-harmonics of the frequency response on each normal mode were mixed.

## 4.4 Conclusions

In this chapter, Floquet forms have been used to project the equations of motion with many degrees of freedom, in a similar fashion as classic modal analysis. By exhibiting convergence in the free and forced vibrating cases, the FF-projection is shown to be a generalization of modal analysis of time-periodic systems. Like classic harmonic eigenmodes of structures in equilibrium states, Floquet Forms allow to orthogonally decompose, in space but also in time, the oscillations of a structure in periodic state.

We have shown that an issue with the computation of FFs for large degrees of freedom systems lies in the size of the Hill matrix eigenvalue problem. For each harmonic, the Hill matrix increases by twice the number of degrees of freedom. To reduce the Hill eigenproblem, the equations of motion are projected on classic modes, which leaves a strongly reduced system and a smaller Hill matrix. Consequently, there are fewer series of linearly dependent eigensolutions to sort through, in order to find the proper fundamental Floquet forms.

Projecting the free-vibrating problem leads to uncoupled equations of motion with constant coefficients which are solved algebraically once knowing the Floquet exponents and their associated periodic eigenfunctions. The free vibratory response converges to the actual solution with a relatively small number of Floquet forms. This results in a much faster computation than a direct integration on the original set of time-periodic equations. In case of forced vibration, the excitation is projected on a time-periodic FF-basis. The uncoupled equations of motion are integrated over time to compute the amplitude per Floquet form. This case is converging with increasing number of FFs as well and we showed that the stationary response is properly decomposed on each Floquet form. However, the computations are relatively slow because the right hand side of the projected equations requires an inversion of the FF-basis. This is a point to improve since finding the inverse FFs should be possible analytically according to literature.

# Conclusions

---

Modal analysis itself is a well established method using eigensolutions of the equations of motion to compute modes. Classic harmonic modes are however limited to LTI systems, but we have shown the proper orthogonal basis for time-periodic systems is formed with Floquet forms. These have been computed efficiently and robustly and applied on time-periodic systems and are used effectively for modal reduction and stability analysis, as shown in this thesis.

The methods to compute Floquet forms are limited by different factors. The time domain approach requires a non-trivial time-integration of the equations of motion which is relatively costly in terms of computational power. Furthermore the periodic eigenvector is computed in the time domain without direct knowledge of its frequency content. The frequency domain approach has the difficulty that the Hill eigenspectrum is polluted by linearly dependent eigenpairs. Although this has been treated effectively by eigenvector sorting to compute the most converged FF.

Treating the Hill spectrum is necessary to obtain accurate results, especially near stability boundaries. When comparing frequency domain methods, eigenvector sorting provides the most efficient way to compute Floquet forms. Eigenvalue sorting in the primitive cell is very efficient in case of steady state or flip bifurcations. However in case of Neimark-Sacker bifurcation, eigenvalue sorting requires a large number of harmonics to converge. This is due to the Hill spectrum being far from the primitive cell. Eigenvector sorting requires the fewest number of harmonics and provides the most converged FFs.

When converged FFs are computed, they can be used to analyze the transverse vibratory response of a structure in periodic state. By decomposing the response into FFs and analyzing these individually, the principal motions of the system are revealed. Furthermore, the envelope of the response is computed using the periodic eigenvector and FF-amplitude.

The free-vibrating periodic Ziegler column in periodic state shows the robustness of stability computations. Both conservative and nonconservative cases are analyzed. Using various methods the FFs have been verified for giving the correct stability and response. FF stability analysis is verified in the fundamentally stable domain with Floquet multipliers obtained by time-domain methods. In the fundamentally unstable domain the stability threshold of averaging verifies FF computations at high frequency. Verification of the response computed by FFs and direct time integration show good agreement.

An issue in computing FFs of large degree of freedom systems is the Hill matrix

eigenvalue problem. For each harmonic the Hill matrix increases with twice the number of degrees of freedom. To simplify the Hill eigenproblem the equations of motion are projected on classic modes, which leaves a strongly reduced system and a smaller Hill matrix. Furthermore there are fewer series of linearly dependent eigensolutions to sort through to obtain FFs.

The free-vibrating problem leads to constant coefficients in the FF-equations of motion which are solved algebraically by Floquet exponents. The response with increasing number of FFs in the basis converges to the one computed by direct time-integration. Using a reduced basis of FFs results in a much faster computation than directly integrating the coupled time-periodic equation of motion.

In case of forced vibration, the excitation is projected on a time-periodic FF-basis. The uncoupled equations of motion are integrated over time to compute the amplitude per FF. This case is converging with increasing number of FFs in the basis as well. The response is decomposed per FF. The computations are relatively slow because the right hand side requires an inversion of FF-basis. This is a point to improve since finding the inverse FFs should be possible analytically according to literature.

# Appendices



# Equation of motion of the Ziegler column

With the help of Newton's second law applied on the two rotating rigid bars parameterized by  $\theta_1(t)$  and  $\theta_2(t)$ , it is possible to establish the nonlinear equation of motion of the Ziegler column described in Fig. 2.1(c). By equating the quantity of acceleration  $\mathcal{A}_{bar1}$  and  $\mathcal{A}_{bar2}$  on one side, to the sum of the external moments  $\mathcal{M}_{bar1}$  and  $\mathcal{M}_{bar2}$ , on the bar 1 and 2, respectively, on the other side, we obtain a system of two nonlinear Ordinary Differential Equations:

$$\begin{aligned}\mathcal{A}_{bar1} &= \frac{d}{dt} \left( \frac{\partial \mathcal{T}}{\partial \dot{\theta}_1} \right) - \frac{\partial \mathcal{T}}{\partial \theta_1} = \mathcal{M}_1^k + \mathcal{M}_1^c + \mathcal{M}_1^P, \\ \mathcal{A}_{bar2} &= \frac{d}{dt} \left( \frac{\partial \mathcal{T}}{\partial \dot{\theta}_2} \right) - \frac{\partial \mathcal{T}}{\partial \theta_2} = \mathcal{M}_2^k + \mathcal{M}_2^c + \mathcal{M}_2^P.\end{aligned}\tag{A.1}$$

In Eq.(A.1),  $\mathcal{T}(\theta_1, \theta_2, \dot{\theta}_1, \dot{\theta}_2)$  is the kinetic energy of the system of two rotating rigid bars reading

$$\mathcal{T} = \frac{8}{3}ml^2\dot{\theta}_1^2 + \frac{2}{3}ml^2\dot{\theta}_2^2 + 2ml^2\dot{\theta}_1\dot{\theta}_2 \cos(\theta_1 - \theta_2).\tag{A.2}$$

The moments  $\mathcal{M}_1^k$  and  $\mathcal{M}_1^k$  represent the restoring elastic moments due to the rotational springs and read, in bar 1 and 2, respectively:

$$\mathcal{M}_1^k = k\theta_1 + k(\theta_1 - \theta_2) \text{ and } \mathcal{M}_2^k = k(\theta_2 - \theta_1).\tag{A.3}$$

The moments  $\mathcal{M}_1^P$  and  $\mathcal{M}_2^P$  are due to the end external harmonic force  $F(t)$  and read, in bar 1 and 2, respectively:

$$\begin{aligned}\mathcal{M}_1^P &= 2lA \cos(\Omega t) [-\cos(\theta_1) \sin(\eta\theta_2) + \sin(\theta_1) \cos(\eta\theta_2)], \\ \mathcal{M}_2^P &= 2lA \cos(\Omega t) [-\cos(\theta_2) \sin(\eta\theta_2) + \sin(\theta_2) \cos(\eta\theta_2)].\end{aligned}\tag{A.4}$$

If  $\eta = 0$  (in the case of a force remaining horizontal upon deformation of the structure), the moments  $\mathcal{M}_1^P$  and  $\mathcal{M}_2^P$  can be derived from the gradient of a potential energy, and the system is said to be conservative, or periodically conservative as the value of the moments are periodically varying with time. If  $\eta = 1$  (in the case of moments depending on the position of the structure in space), the previous property is not true and the system is non-conservative. Replacing Eqs.(A.2)-(A.4) into Eq.(A.1), one obtains the nonlinear system of equation of motions of the two-degrees-of-freedom as expressed in Eq.(2.13).



# Hill matrix implementation

---

In this appendix the generalized formulation for the Hill matrix in the real domain is derived and its implementation is shown.

The generalized formulation is derived because this leads to more efficient eigenvalue problem solving. Generalized equations of motion in state space are written in the canonical form (B.1)

$$\mathbf{J}_B \dot{\mathbf{y}}(t) = \mathbf{J}_A(t) \mathbf{y}(t). \quad (\text{B.1})$$

For applications in FEM the Jacobian matrices  $\mathbf{J}_A(t)$  and  $\mathbf{J}_B$  are sparse. The Hill matrices derived in chapter 3 are both based on the nongeneralized state space formulation  $\dot{\mathbf{y}}(t) = \mathbf{J}(t) \mathbf{y}(t)$ . This formulation can be found from generalized matrices since  $\mathbf{J}(t) = \mathbf{J}_B^{-1} \mathbf{J}_A(t)$ . However this requires inverting sparse matrix  $\mathbf{J}_B$ . Inversion of a sparse matrix for eigenproblems has two major drawbacks. First of all, the inversion itself is computationally expensive. Second of all by inverting a sparse matrix, in general it loses its sparseness. Finding eigenvalues of full matrices is much more computationally expensive. Therefore inverting matrices is to be avoided. In this appendix not the derivation of the real Hill matrix and its numerical implementation in Python is shown. The code is limited to using packages NumPy and SciPy [76].

## B.1 Floquet transform

The response vector  $\mathbf{y}(t)$  from (B.1) is decomposed into  $N$  linearly independent Floquet forms (FFs):

$$\mathbf{y} = \sum_n \mathbf{p}_n(t) q_n(t), \quad \text{with: } \mathbf{p}_n(t) = \mathbf{p}(t + T). \quad (\text{B.2})$$

The eigenvector  $\mathbf{p}_n(t)$  is periodic and each FF has an amplitude  $q_n(t)$ .

When neglecting excitation the equations of motion (B.1), we get homogeneous linear ODE for which the solution  $\mathbf{q}(t) = e^{s_n t}$  can be imposed. For the derivative this results in:

$$\dot{\mathbf{y}}_n = \dot{\mathbf{p}}_n(t) q_n(t) + \mathbf{p}_n(t) \dot{q}_n(t) = (\dot{\mathbf{p}}(t) + s_n \mathbf{p}(t)) e^{s_n t}. \quad (\text{B.3})$$

## B.2 Fourier transform

By applying a Fourier transform on periodic functions the system equations are transformed to the frequency domain. The periodic components are the eigenfunction  $\mathbf{p}(t)$ , its derivative  $\dot{\mathbf{p}}(t)$  and the periodic Jacobian  $\mathbf{J}(t)$ .

The Fourier transform of the Floquet eigenfunction in the real domain results in (B.4):

$$\mathbf{p}_n(t) = \frac{\mathbf{a}_0}{2} + \sum_{j=1}^H (\mathbf{a}_j \cos j\beta t + \mathbf{b}_j \sin j\beta t), \quad (\text{B.4})$$

where the superscript  $h$  is an index that denotes the harmonic used. Coefficients  $a_j$  and  $b_j$  belong to the cosine and sine terms of the eigenfunction respectively. Its derivative is simply found by taking the derivative of the Fourier series (B.5):

$$\dot{\mathbf{p}}_n(t) = \sum_{j=1}^H (j\beta \mathbf{b}_j \cos j\beta t - j\beta \mathbf{a}_j \sin j\beta t). \quad (\text{B.5})$$

The Fourier transform of the Jacobian is shown (B.6):

$$\mathbf{J}_A(t) = \frac{\mathbf{A}_0^c}{2} + \sum_{h=1}^H (\mathbf{A}_c^h \cos h\beta t + \mathbf{A}_s^h \sin h\beta t), \quad (\text{B.6})$$

where the coefficients  $A_{c,s}$  represent cosine and sine terms respectively.

## B.3 Harmonic Balance

The state space equation is rewritten to balance formulation (B.7):

$$\mathbf{J}_B \dot{\mathbf{y}}_n(t) = \mathbf{J}_A(t) \mathbf{y}_n(t) \iff \mathbf{J}_A(t) \mathbf{y}_n(t) - \mathbf{J}_B \dot{\mathbf{y}}_n(t) = \mathbf{0}. \quad (\text{B.7})$$

Because the balance in total is equal to zero, each harmonic must balance out to zero as well. Meaning that for each cosine term  $\cos j\beta t$  or sine term  $\sin j\beta t$  its coefficients must equal to zero. To find these coefficients the Fourier transformed terms (B.4), (B.5) and (B.6) need to be substituted in the balance equation (B.7).

To compute the first term of the balance equation  $\mathbf{J}_A(t) \mathbf{y}_n(t)$ , both periodic functions  $\mathbf{J}_A(t)$  and  $\mathbf{p}_n(t)$  are replaced by two Fourier series (B.8):

$$\mathbf{J}_A(t) \mathbf{y}_n(t) = \left( \frac{1}{2} \mathbf{A}_0^c + \sum_{h=1}^{\infty} (\mathbf{A}_h^c \cos(h\beta t) + \mathbf{A}_h^s \sin(h\beta t)) \right) \left( \frac{\mathbf{a}_0}{2} + \sum_{j=1}^{\infty} (\mathbf{a}_j \cos(j\beta t) + \mathbf{b}_j \sin(j\beta t)) \right) e^{s_n t}. \quad (\text{B.8})$$

This equation (B.8) contains cosine and sine products. These must be written to Using the trigonometric product-to-sum identities:

$$\begin{aligned}\cos \alpha \cos \beta &= \frac{1}{2} [\cos(\alpha + \beta) + \cos(\alpha - \beta)], \\ \sin \alpha \sin \beta &= \frac{1}{2} [\cos(\alpha - \beta) - \cos(\alpha + \beta)], \\ \sin \alpha \cos \beta &= \frac{1}{2} [\sin(\alpha + \beta) + \sin(\alpha - \beta)], \\ \cos \alpha \sin \beta &= \frac{1}{2} [\sin(\alpha + \beta) - \sin(\alpha - \beta)],\end{aligned}$$

which leads to the following expression for  $\mathbf{J}_A(t)\mathbf{y}_n(t)$ :

$$\begin{aligned}\mathbf{J}_A(t)\mathbf{y}_n(t) &= \left( \frac{1}{2}\mathbf{A}_0^c \left( \frac{\mathbf{a}_0}{2} + \sum_{j=1}^{\infty} \mathbf{a}_j \cos j\beta\tau + \mathbf{b}_j \sin j\beta\tau \right) \right. \\ &+ \sum_{h=1}^{\infty} \mathbf{A}_h^c \left[ \frac{\mathbf{a}_0}{2} \cos h\beta\tau + \sum_{j=1}^{\infty} \frac{\mathbf{a}_j}{2} (\cos(h+j)\beta\tau + \cos(h-j)\beta\tau) \right. \\ &\quad \left. \left. + \frac{\mathbf{b}_j}{2} (\sin(h+j)\beta\tau - \sin(h-j)\beta\tau) \right] \right. \quad (\text{B.9})\end{aligned}$$

$$\begin{aligned}&+ \sum_{h=1}^{\infty} \mathbf{A}_h^s \left[ \frac{\mathbf{a}_0}{2} \sin h\beta\tau + \sum_{j=1}^{\infty} \frac{\mathbf{a}_j}{2} (\sin(h+j)\beta\tau + \sin(h-j)\beta\tau) \right. \\ &\quad \left. \left. + \frac{\mathbf{b}_j}{2} (-\cos(h+j)\beta\tau + \cos(h-j)\beta\tau) \right] \right) e^{s_n t}. \quad (\text{B.10})\end{aligned}$$

$$\begin{aligned}&+ \frac{\mathbf{b}_j}{2} (-\cos(h+j)\beta\tau + \cos(h-j)\beta\tau) \left. \right) e^{s_n t}. \quad (\text{B.11})\end{aligned}$$

This term is cumbersome, especially compared to the complex domain harmonic balance from section 3.3.1. Important to note is the role of difference frequencies frequencies  $h+j$  and  $h-j$ . These lead to off-diagonal terms in the Hill matrix.

The second term in the harmonic balance  $\mathbf{J}_B\dot{\mathbf{y}}_n(t)$  is found (B.12):

$$\mathbf{J}_B\dot{\mathbf{y}}_n(t) = \mathbf{B} \left( \frac{\mathbf{a}_0}{2} + \sum_{j=1}^H ((s_n \mathbf{a}_j + j\beta \mathbf{b}_j) \cos j\beta t + (s_n \mathbf{b}_j - j\beta \mathbf{a}_j) \sin j\beta t) \right) e^{s_n t}. \quad (\text{B.12})$$

To stay consistent with the notation of the coefficients of  $\mathbf{J}_A(t)$ , the matrix  $\mathbf{J}_B$  in the frequency domain is written as  $\mathbf{B}$ .

Writing the harmonic balance (B.1) in totality becomes very cumbersome with terms (B.8) and (B.12). Therefore the system is rewritten into Hill matrices.

## B.4 Hill matrices

The harmonic balance in the real frequency domain leads to a block matrix with Hankel and Toeplitz matrices. In matrix form the harmonic balance is rewritten:  $(\mathbb{H}_A \boldsymbol{\phi} - s_n \mathbb{H}_B \boldsymbol{\phi}) e^{s_n t} = \mathbf{0}$

The eigenvector terms are decomposed into  $\phi = [\mathbf{a}_0/2, \mathbf{a}_1, \dots, \mathbf{a}_H, \mathbf{b}_1, \dots, \mathbf{b}_H]^T$ .

The matrix  $\mathbb{H}_B$  is found by separating the Floquet exponent  $s_n$  terms from the frequency term  $j\beta$  in (B.12). This leads to the blockdiagonal matrix (B.13):

$$\mathbb{H}_B = \begin{bmatrix} \mathbf{B} & & \mathbf{0} \\ & \ddots & \\ \mathbf{0} & & \mathbf{B} \end{bmatrix}. \quad (\text{B.13})$$

The matrix  $\mathbb{H}_A$  is found similar to the direct Hill matrix from section 3.3.1. Therefore the formulation becomes (B.14):

$$\mathbb{H}_A = \begin{bmatrix} \frac{1}{2}\mathbf{A}_c^0 & \frac{1}{2}\mathbf{A}_c & \frac{1}{2}\mathbf{A}_s \\ \mathbf{A}_c^T & \begin{bmatrix} \mathbf{K}_c + \mathbf{T}_c \end{bmatrix} & \begin{bmatrix} \mathbf{K}_s - \mathbf{T}_s \end{bmatrix} \\ \mathbf{A}_s^T & \begin{bmatrix} \mathbf{K}_s + \mathbf{T}_s \end{bmatrix} & \begin{bmatrix} \mathbf{T}_c - \mathbf{K}_c \end{bmatrix} \end{bmatrix}, \quad (\text{B.14})$$

where

$$\mathbf{A}_c = \{\mathbf{A}_c^1 \mathbf{A}_c^2 \dots \mathbf{A}_c^H\} \quad \text{and} \quad \mathbf{A}_s = \{\mathbf{A}_s^1 \mathbf{A}_s^2 \dots \mathbf{A}_s^H\}$$

are  $(N \times HN)$ -dimensional block vectors ( $\mathbf{A}_c^T$  and  $\mathbf{A}_s^T$  are the transpose of the above block vectors, not of the full matrices  $\mathbf{A}_c$  and  $\mathbf{A}_s$  meaning one has to be careful to not transpose the matrices  $\mathbf{A}_c^h$  and  $\mathbf{A}_s^h$  in the process but simply ordering them in a column block vector),

$$\mathbf{K}_{c,s} = \frac{1}{2} \begin{bmatrix} \mathbf{A}_{c,s}^2 & \mathbf{A}_{c,s}^3 & \mathbf{A}_{c,s}^4 & \dots & \mathbf{A}_{c,s}^{H+1} \\ \mathbf{A}_{c,s}^3 & \mathbf{A}_{c,s}^4 & \mathbf{A}_{c,s}^5 & \dots & \mathbf{A}_{c,s}^{H+2} \\ \mathbf{A}_{c,s}^4 & \mathbf{A}_{c,s}^5 & \mathbf{A}_{c,s}^6 & \dots & \mathbf{A}_{c,s}^{H+3} \\ \vdots & \vdots & \vdots & \ddots & \vdots \\ \mathbf{A}_{c,s}^{H+1} & \mathbf{A}_{c,s}^{H+2} & \mathbf{A}_{c,s}^{H+3} & \dots & \mathbf{A}_{c,s}^{2H} \end{bmatrix},$$

are  $(NH \times NH)$ -dimensional block matrices with harmonic contributions of the Jacobian either on cosine or sine, and where

$$\mathbf{T}_c = \frac{1}{2} \begin{bmatrix} \mathbf{A}_c^0 & \mathbf{A}_c^1 & \mathbf{A}_c^2 & \dots & \mathbf{A}_c^{H-1} \\ \mathbf{A}_c^1 & \mathbf{A}_c^0 & \mathbf{A}_c^1 & \dots & \mathbf{A}_c^{H-2} \\ \mathbf{A}_c^2 & \mathbf{A}_c^1 & \mathbf{A}_c^0 & \dots & \mathbf{A}_c^{H-3} \\ \vdots & \vdots & \vdots & \ddots & \vdots \\ \mathbf{A}_c^{H-1} & \mathbf{A}_c^{H-2} & \mathbf{A}_c^{H-3} & \dots & \mathbf{A}_c^0 \end{bmatrix},$$

and

$$\mathbf{T}_s = \frac{1}{2} \begin{bmatrix} 2\beta\mathbf{B} & -\mathbf{A}_s^1 & -\mathbf{A}_s^2 & \dots & -\mathbf{A}_s^{H-1} \\ \mathbf{A}_s^1 & 4\beta\mathbf{B} & -\mathbf{A}_s^1 & \dots & -\mathbf{A}_s^{H-2} \\ \mathbf{A}_s^2 & \mathbf{A}_s^1 & 6\beta\mathbf{B} & \dots & -\mathbf{A}_s^{H-3} \\ \vdots & \vdots & \vdots & \ddots & \vdots \\ \mathbf{A}_s^{H-1} & \mathbf{A}_s^{H-2} & \mathbf{A}_s^{H-3} & \dots & 2H\beta\mathbf{B} \end{bmatrix},$$

are  $(NH \times NH)$ -dimensional block matrices. Although seemingly complicated if compared to the general complex Hill matrix that is the sum of a complex block diagonal matrix and a real Toeplitz block matrix, the general real Hill matrix is relatively easy to numerically implement. Indeed, it is composed of  $\mathbf{K}_c$  and  $\mathbf{K}_s$  which are Hankel block matrices,  $\mathbf{T}_c$

that is a Toeplitz matrix and  $\mathbf{T}_s$  that is the sum of a real block diagonal matrix and a Toeplitz matrix. Applying the eigenvector sorting algorithm on the real Hill matrix  $\mathbf{H}^H$  of Eq.(3.25) allows to compute the  $N$  fundamental FFs of a system in a general periodic state.

## B.5 Numerical implementation

The numerical implementation of these matrix constructions is given in Python as an example for users. The NumPy and SciPy packages are used. The jacobian matrices  $\mathbf{J}_A(t)$  and  $\mathbf{J}_B$  are implemented as sparse matrices in SciPy. The decomposed jacobian  $\mathbf{J}_A(t) = \mathbf{A}_0/2 + \sum_h \mathbf{A}_c \cos(h\beta t) + \mathbf{A}_s \sin(h\beta t)$  and  $\mathbf{J}_B = \mathbf{B}$  are used to set up Hill's matrix in the real domain.

The function to compute the real Hill matrices  $\mathbb{H}_{A,B}$  are based on  $\mathbf{A}_{c,s}^h$  and  $\mathbf{B}$ , number of harmonics  $H$ , frequency  $\beta$  and number of degrees of freedom  $N$ :

---

```
def Hill_real_A_B(cosine_mats, sine_mats, Hmax, freq, Ndim, B_mat):
    """ Create Hill matrix in the real domain          [J0/2  Jc  Js]
    with the following form:                          |Jc'/2 A1  B1|
                                                    [Js'/2 B2  A2] """
    # Construct submatrices
    A1 = (Toeplitz_sparse(cosine_mats[:Hmax]) +
          Hankel_sparse(cosine_mats[2:Hmax+2], cosine_mats[Hmax+1:]))/2
    A2 = (Toeplitz_sparse(cosine_mats[:Hmax]) -
          Hankel_sparse(cosine_mats[2:Hmax+2], cosine_mats[Hmax+1:]))/2

    BM = freq*sparse.kron(sparse.diags(np.arange(1,Hmax+1)), B_mat)
    B1 = (Toeplitz_sparse(sine_mats[:Hmax], - np.asarray(sine_mats[:Hmax]))/2 +
          Hankel_sparse(sine_mats[2:Hmax+2], sine_mats[Hmax+1:]))/2 - BM
    B2 = (Toeplitz_sparse(-np.asarray(sine_mats[:Hmax]), sine_mats[:Hmax])/2 +
          Hankel_sparse(sine_mats[2:Hmax+2], sine_mats[Hmax+1:]))/2 + BM

    # Construct columns
    col1 = []
    col1.append(sparse.csr_matrix(cosine_mats[0]/2))
    col1.extend(cosine_mats[1:Hmax+1])
    col1.extend(sine_mats[1:Hmax+1])
    for i in range(len(col1)):
        col1[i] = sparse.coo_matrix(col1[i])
        col1 = sparse.vstack(col1)

    cos_row = []
    cos_row.extend(cosine_mats[1:Hmax+1])
    for i in range(len(cos_row)):
        cos_row[i] = sparse.coo_matrix(cos_row[i])
        cos_row = sparse.hstack(cos_row)/2

    sin_row = []
```

---

```

sin_row.extend(sine_mats[1:Hmax+1])
for i in range(len(sin_row)):
    sin_row[i] = sparse.coo_matrix(sin_row[i])
    sin_row = sparse.hstack(sin_row)/2

col2 = sparse.bmat([[cos_row], [A1], [B2]])
col3 = sparse.bmat([[sin_row], [B1], [A2]])
return (sparse.hstack((col1, col2, col3), format="csr"),
        sparse.kron(np.eye(2*Hmax+1), B_mat, format="csr"))

```

---

The construction of  $\mathbb{H}_A$  (B.14) requires the computation of sparse block Hankel and Toeplitz matrices. Care is taken that the first column is the vertical block column of:  $[\mathbf{A}_0/2, \mathbf{A}_c^1, \dots, \mathbf{A}_c^h, \mathbf{A}_s^1, \dots, \mathbf{A}_s^H]$ .

The matrices returned are purely real numbers and have no imaginary numbers. This is useful for applications where eigensolvers are not compatible with complex values.

The real Hill matrix requires block Toeplitz and Hankel matrices, for which there is not a sparse block implementation in Scipy. Therefore these algorithms are shown to compute sparse Toeplitz and Hankel matrices.

---

```

from scipy import sparse
import numpy as np

def Toeplitz_sparse(rows, cols=None):
    """
    Get Toeplitz matrix of a set of real square matrices based on the first row
    and the first column.

    """
    if cols is None:
        cols = rows

    vals = []
    vals.extend(rows[-1:0:-1])
    vals.extend(cols[:])
    vals.extend([None])

    a, b = np.ogrid[0:len(rows), len(cols) - 1:-1:-1]
    indx = a + b
    return sparse.bmat(np.asarray(vals)[indx], format='csr')

def Hankel_sparse(rows, cols=None):
    """
    Get Hankel matrix of a set of real square matrices based on the first column
    and the last row.

    """
    if cols is None:

```

---

```
cols = rows

vals = []
vals.extend(rows[-1:0:-1])
vals.extend(cols[:])
vals.extend([None])

a, b = np.ogrid[0:len(rows), 0:len(cols)]
indx = a + b
return sparse.bmat(np.asarray(vals)[indx], format='csr')
```

---



# High Frequency Averaging of the statically diverging Ziegler Column in periodic elastic state

The goal of this appendix is to compare linear stability based on averaging method to the one obtained by the computation of FFs in the frequency domain. The use of averaging method for LTP systems is well known [46, 26]. Averaging is a perturbation method that separates the equations of motion into a periodic fast timescale and a slow part. The averaged response of the fast part is taken into account, hence the name averaging. From averaging, an expression is found for the high frequency stability threshold. This is expressed for the conservative case in the load amplitude:

$$\lambda_a = \frac{\beta}{40} \sqrt{-1989 + 3424P_0 + 3\sqrt{434669 - 271744P_0}}. \quad (\text{C.1})$$

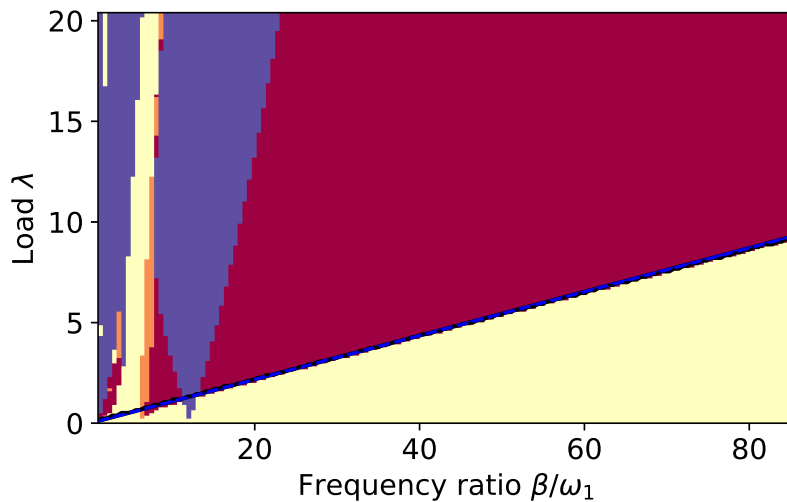


Figure C.1: Comparing the stability found through averaging (black line) with stability calculations using Floquet forms. The red zone is stable, yellow is  $T$ -unstable, purple is  $2T$ -unstable and orange is almost-periodically unstable regions. For high frequencies both methods give similar results. This is to be expected since averaging is valid for high frequencies. The calculation is done on a  $150 \times 150$  grid, the colors are displayed using a nearest neighbour interpolation.

In Fig.C.1 the stability domain over large range of frequency is compared to averaging (black line). At high frequency the stability boundary computed by averaging and FF-stability is in good agreement. The FF computation is therefore verified at high frequency

by averaging. The definition of high frequency is when the system frequency  $\beta$  is much higher than the natural frequency  $\omega_1$  so that:  $\beta \gg \omega_1$ . The stability boundary of averaging is in agreement if  $\beta > 15\omega_1$ . Both methods are first order perturbative methods, therefore the results have the same underlying LTP equations.

## C.1 Averaged equations of motion

Step 1 is to separate the non-linear EoM into two parts, a "static" or slow-time excitation  $\mathbf{f}(\dot{\boldsymbol{\theta}}, \boldsymbol{\theta})$  and a periodic or fast-time excitation  $\mathbf{q}(\boldsymbol{\theta})$  (C.2):

$$\ddot{\boldsymbol{\theta}} = \mathbf{f}(\dot{\boldsymbol{\theta}}, \boldsymbol{\theta}) + \Omega \mathbf{q}(\boldsymbol{\theta}) \quad (\text{C.2})$$

The Ziegler column in the fundamentally unstable regime from section 3.7 is used. Which has the equations of motion:  $\mathbf{M}\ddot{\boldsymbol{\theta}}(\tau) + \mathbf{K}\dot{\boldsymbol{\theta}}(\tau) + (\mathbf{P}_0 + \mathbf{P}_A \cos(\beta\tau))\boldsymbol{\theta}(\tau) = 0$ . With mass matrix  $\mathbf{M}$ , constant stiffness matrix  $\mathbf{K}$  and a static  $\mathbf{P}_0$  and periodic  $\mathbf{P}_A$  compressive stress matrices.

The matrices have the following values:

$$\mathbf{M} = \begin{bmatrix} 1 & \frac{3}{8} \\ \frac{3}{2} & 1 \end{bmatrix}, \quad \mathbf{K} = \begin{bmatrix} \frac{3}{8} & -\frac{3}{16} \\ -\frac{3}{4} & \frac{3}{4} \end{bmatrix}, \quad \mathbf{P}_{0,A} = P_{0,A} \begin{bmatrix} -1 & \eta \\ 0 & 4\eta - 4 \end{bmatrix} \quad (\text{C.3})$$

Where  $\tau$  is the dimensionless time based on the base natural frequency of the system  $\tau = \omega_0 t$ , with the radial frequency  $\omega_0 = \sqrt{\frac{k}{ml^2}}$ . Splitting up the function in a static and periodic term as in eqn.C.2 gives for the static part  $\mathbf{f}(\dot{\boldsymbol{\theta}}, \boldsymbol{\theta}) = \mathbf{f}(\boldsymbol{\theta})$ . Using the constant matrices this means the static part becomes  $\mathbf{f}(\boldsymbol{\theta}) = \mathbf{M}^{-1}(\mathbf{K} + \mathbf{P}_0)\boldsymbol{\theta}(\tau)$ .

Inserting the matrices:  $\mathbf{f}(\boldsymbol{\theta}) = \begin{bmatrix} 1 & \frac{3}{8} \\ \frac{3}{2} & 1 \end{bmatrix}^{-1} \left( \begin{bmatrix} \frac{3}{8} & -\frac{3}{16} \\ -\frac{3}{4} & \frac{3}{4} \end{bmatrix} + \frac{3l}{8k} P_0 \begin{bmatrix} -1 & \eta \\ 0 & 4\eta - 4 \end{bmatrix} \right) \boldsymbol{\theta}(\tau)$   
this results in:

$$\mathbf{f}(\boldsymbol{\theta}) = \left( \begin{bmatrix} \frac{3}{2} & -\frac{15}{14} \\ -3 & \frac{33}{14} \end{bmatrix} + \frac{3lP_0}{7k} \begin{bmatrix} -2 & 3 - \eta \\ 3 & 5\eta - 8 \end{bmatrix} \right) \boldsymbol{\theta}(\tau) \quad (\text{C.4})$$

For the fast time function:

$$\beta \mathbf{q}(\boldsymbol{\theta}) = \mathbf{M}^{-1} \mathbf{P}_A \cos(\beta\tau) \quad (\text{C.5})$$

$$\beta \mathbf{q}(\boldsymbol{\theta}) = \begin{bmatrix} 1 & \frac{3}{8} \\ \frac{3}{2} & 1 \end{bmatrix}^{-1} \left( \frac{3l}{8k} (P_A \cos(\beta\tau)) \begin{bmatrix} -1 & \eta \\ 0 & 4\eta - 4 \end{bmatrix} \right) \boldsymbol{\theta}(\tau) \quad (\text{C.6})$$

$$\beta \mathbf{q}(\boldsymbol{\theta}) = \frac{3lP_A}{7k} \begin{bmatrix} -2 & 3 - \eta \\ 3 & 5\eta - 8 \end{bmatrix} \cos(\beta\tau) \boldsymbol{\theta}(\tau) \quad (\text{C.7})$$

So that:

$$\mathbf{q}(\boldsymbol{\theta}(\tau)) = \frac{3lP_A}{7k\beta} \begin{bmatrix} -2 & 3 - \eta \\ 3 & 5\eta - 8 \end{bmatrix} \cos(\beta\tau)\boldsymbol{\theta}(\tau) \quad (\text{C.8})$$

The next step is to separate the system into a "slow"  $\mathbf{x}(T_0) = \{x_1(T_0), x_2(T_0)\}^T$  and a "fast" part  $\boldsymbol{\psi}(T_0) = \{x_1(T_1), x_2(T_1)\}^T$ . This is only valid if  $\Omega \gg \omega_n$  or  $\beta \gg \omega_n/\omega_0$ . The assumed solution is written in the form:

$$\boldsymbol{\theta}(T_0, T_1) = \mathbf{x}(T_0) + \epsilon\boldsymbol{\psi}(T_1) \quad (\text{C.9})$$

Where  $\epsilon = 1/\beta$  and at high-frequency it is assumed that  $\epsilon \ll 1$  and where  $T_1 = \beta\tau = \Omega t$ .

Introducing the averaging operator where a function inside the brackets is averaged over one period so that for the fast time the function is:

$$\langle \bullet \rangle = \frac{1}{2\pi} \int_0^{2\pi} \bullet dT_1 \quad (\text{C.10})$$

For eqn.C.8 the average is zero due to the cosine:  $\langle \mathbf{q}(\boldsymbol{\theta}) \rangle = \mathbf{0}$  and by definition the fast time solution  $\langle \boldsymbol{\psi} \rangle = \mathbf{0}$ , so that it's averaged derivatives are also zero.

The solution from eqn.C.9 is inserted in eqn.C.2. The timescales of  $\mathbf{x}(T_0)$  and  $\boldsymbol{\psi}(T_1)$  are completely independent so that  $\frac{d^2}{dt^2}(\boldsymbol{\theta}(T_0, T_1))$  and  $\frac{d\boldsymbol{\psi}}{dT_1^2} = \epsilon^{-2} \frac{d\boldsymbol{\psi}}{dT_1^2}$  becomes:

$$D_0^2 \mathbf{x} + \epsilon^{-1} D_1^2 \boldsymbol{\psi} = \mathbf{f}(\mathbf{x} + \epsilon\boldsymbol{\psi}) + \epsilon^{-1} \mathbf{q}(\mathbf{x} + \epsilon\boldsymbol{\psi}) \quad (\text{C.11})$$

The notation from [26] is used for the derivative operators of slow time  $D_0 = \frac{\partial}{\partial T_0}$  and fast time  $D_1 = \frac{\partial}{\partial T_1}$ .

The next step is to apply averaging over eqn.C.11, this results in the second fast time derivative equal to zero  $\langle D_1^2 \boldsymbol{\psi} \rangle = 0$  and the slow time derivative unaffected  $D_0^2 \mathbf{x} = \langle D_0^2 \mathbf{x} \rangle$ , so that:

$$D_0^2 \mathbf{x} = \langle \mathbf{f}(\mathbf{x} + \epsilon\boldsymbol{\psi}) + \epsilon^{-1} \mathbf{q}(\mathbf{x} + \epsilon\boldsymbol{\psi}) \rangle \quad (\text{C.12})$$

Subtracting eqn.C.12 from eqn.C.11 gives the second derivative for the fast time scale:

$$D_1^2 \boldsymbol{\psi} = \epsilon \mathbf{f}(\mathbf{x} + \epsilon\boldsymbol{\psi}) + \mathbf{q}(\mathbf{x} + \epsilon\boldsymbol{\psi}) - \epsilon \langle \mathbf{f}(\mathbf{x} + \epsilon\boldsymbol{\psi}) + \epsilon^{-1} \mathbf{q}(\mathbf{x} + \epsilon\boldsymbol{\psi}) \rangle \quad (\text{C.13})$$

Important to note here that the average of the second time derivative is zero  $\langle D_1^2 \boldsymbol{\psi} \rangle = 0$ , for the derivative itself there exists some value of  $\tau$  where it is not zero  $D_1^2 \boldsymbol{\psi}(\tau) \neq 0$ .

Applying a first order Taylor approximation on eqn.C.12 so that:

$$\mathbf{a}(\mathbf{x} + \epsilon\boldsymbol{\psi}) \approx \mathbf{a}(\mathbf{x}) + \epsilon\boldsymbol{\psi} \cdot \partial \mathbf{a}(\mathbf{x}) / \partial \mathbf{x} + O(\epsilon^2) \quad (\text{C.14})$$

This results in the equation and applying this on (C.12) and (C.13) results in the expression:

$$D_0^2 \mathbf{x} = \langle \mathbf{f}(\mathbf{x}) + \epsilon \boldsymbol{\psi} \frac{\partial \mathbf{f}(\mathbf{x})}{\mathbf{x}} + \epsilon^{-1} \mathbf{q}(\mathbf{x}) + \boldsymbol{\psi} \frac{\partial \mathbf{q}(\mathbf{x})}{\mathbf{x}} + O(\epsilon^2) \rangle \quad (\text{C.15})$$

$$D_1^2 \boldsymbol{\psi} = \mathbf{q}(\mathbf{x}) + \epsilon (\mathbf{f}(\mathbf{x}) + \epsilon \boldsymbol{\psi} \frac{\partial \mathbf{f}(\mathbf{x})}{\mathbf{x}} + \boldsymbol{\psi} \frac{\partial \mathbf{q}(\mathbf{x})}{\mathbf{x}} - \langle \mathbf{f}(\mathbf{x}) + \epsilon \boldsymbol{\psi} \frac{\partial \mathbf{f}(\mathbf{x})}{\mathbf{x}} + \epsilon^{-1} \mathbf{q}(\mathbf{x}) + \boldsymbol{\psi} \frac{\partial \mathbf{q}(\mathbf{x})}{\mathbf{x}} \rangle) + O(\epsilon^2) \quad (\text{C.16})$$

Ignoring all terms of  $\epsilon$  to get a zeroth order approximation and using the properties of averaging that  $\langle \mathbf{q}(\mathbf{x}) \rangle = 0$  and  $\langle \mathbf{f}(\mathbf{x}) \rangle = \mathbf{f}(\mathbf{x})$ , the equations are simplified:

$$D_0^2 \mathbf{x} = \mathbf{f}(\mathbf{x}) + \langle \boldsymbol{\psi} \frac{\partial \mathbf{q}(\mathbf{x})}{\mathbf{x}} \rangle + O(\epsilon) \quad (\text{C.17})$$

$$D_1^2 \boldsymbol{\psi} = \mathbf{q}(\mathbf{x}) + \epsilon \left( \boldsymbol{\psi} \frac{\partial \mathbf{q}(\mathbf{x})}{\mathbf{x}} - \langle \boldsymbol{\psi} \frac{\partial \mathbf{q}(\mathbf{x})}{\mathbf{x}} \rangle \right) + O(\epsilon^2) \quad (\text{C.18})$$

Using zeroth order approximations of (C.18) and inserting it in (C.8) results in  $D_1^2 \boldsymbol{\psi}(\tau) \approx \mathbf{q}(\mathbf{x}(\tau))$ . Integrating twice with respect to  $\beta\tau$  results in  $\boldsymbol{\psi} = -\mathbf{q}(\mathbf{x}(\tau))$ . This can be expressed as:

$$\boldsymbol{\psi}(\tau) = -\mathbf{M}^{-1} \mathbf{P}_A \cos(\beta\tau) \mathbf{x}(\tau) \quad (\text{C.19})$$

To solve fast time, dynamic function  $\mathbf{q}(\mathbf{x})$  from eqn.C.5 is differentiated with respect to  $\mathbf{x}$ :

$$\frac{\partial \mathbf{q}(\mathbf{x})}{\partial \mathbf{x}} = \mathbf{M}^{-1} \mathbf{P}_A \cos(\beta\tau) \quad (\text{C.20})$$

Inserting (C.19) and (C.20) in (C.17) gives:

$$\ddot{\mathbf{x}}(\tau) = \mathbf{M}^{-1} (\mathbf{K} + \mathbf{P}_0) \mathbf{x}(\tau) + \left( \mathbf{M}^{-1} \mathbf{P}_A \right)^2 \cos^2(\beta\tau) \mathbf{x}(\tau) \quad (\text{C.21})$$

Averaging with  $\langle \cos(\beta\tau)^2 \rangle = 1/2$  gives the equation of motion in slow time:

$$\ddot{\mathbf{x}} = \mathbf{M}^{-1} (\mathbf{K} + \mathbf{P}_0) \mathbf{x} + \frac{1}{2} \left( \mathbf{M}^{-1} \mathbf{P}_A \right)^2 \mathbf{x} \quad (\text{C.22})$$

Since all terms on the right hand side of (C.22) depend linearly on  $\mathbf{x}(\tau)$  it can be seen as an effective stiffness matrix  $\ddot{\mathbf{x}}(\tau) = -\mathbf{K}_{eff} \mathbf{x}(\tau)$ . When writing out this equation this results in:

$$\ddot{\mathbf{x}}(\tau) = \left( \left[ \begin{array}{cc} \frac{3}{2} & -\frac{15}{14} \\ -3 & \frac{33}{14} \end{array} \right] + \frac{3lP_0}{7k} \left[ \begin{array}{cc} -2 & 3 - \eta \\ 3 & 5\eta - 8 \end{array} \right] + \frac{1}{2} \left( \frac{3lP_A}{7k\beta} \right)^2 \left[ \begin{array}{cc} 13 - 3\eta & -5\eta^2 + 25\eta - 30 \\ 15\eta - 30 & 25\eta^2 - 83\eta + 73 \end{array} \right] \right) \mathbf{x}(\tau) \quad (\text{C.23})$$

This system is stable if the effective stiffness is a positive definite matrix. There are three variables in  $\mathbf{K}_{eff}$ : frequency  $\beta$  and the static  $P_0$  and dynamic  $P_A$  load amplitudes.

For the conservative load case  $\eta = 0$ , the dynamic load factor can be rewritten as a fraction of the static critical load  $P_A = \lambda P_{cr}$ . The critical load  $P_{cr}$  is computed by setting  $\beta = 0$ , and solving  $\det(\mathbf{K} - \mathbf{P}) = 0$  and is found to be  $P_{cr} = \frac{(3 \pm \sqrt{5})k}{4l}$  [62].

The stability boundary at high frequency is found by setting the determinant  $|\mathbf{K}_{eff}(P_0, \lambda_t, \beta)| = 0$ . Working out the expression for the determinant and solving for the threshold  $\lambda_t$  results in the following equation (C.24):

$$\lambda_t = \frac{\beta}{40} \sqrt{-1989 + 3424 \frac{8}{7} P_0 + 3 \sqrt{434669 - 271744 \frac{8}{7} P_0}}. \quad (\text{C.24})$$

## Bibliography

- [1] T. Shimanouchi, *Tables of molecular vibrational frequencies*. US Government Printing Office, 1967.
- [2] H. Irretier, “Mathematical foundations of experimental modal analysis in rotor dynamics.,” *Mechanical Systems and Signal Processing*, vol. 2, no. 13, pp. 183–191, 1999.
- [3] D. J. Ewins, *Modal testing: theory and practice*, vol. 15. Research studies press Letchworth, 1984.
- [4] M. Géradin and D. J. Rixen, *Mechanical vibrations: theory and application to structural dynamics*. John Wiley & Sons, 2014.
- [5] P. M. Morse, “Vibration and sound, 2nd,” *McGraw-Hill, New York*, vol. 487, no. 1975, p. 113, 1948.
- [6] A. Lazarus, E. De Langre, P. Manneville, P. Vincent, S. Perisanu, A. Ayari, and S. Purcell, “Statics and dynamics of a nanowire in field emission,” *International Journal of Mechanical Sciences*, vol. 52, no. 11, pp. 1396–1406, 2010.
- [7] M. P. Païdoussis, S. J. Price, and E. De Langre, *Fluid-structure interactions: cross-flow-induced instabilities*. Cambridge University Press, 2010.
- [8] A. Lazarus, O. Thomas, and J.-F. Deü, “Finite element reduced order models for nonlinear vibrations of piezoelectric layered beams with applications to nems,” *Finite Elements in Analysis and Design*, vol. 49, no. 1, pp. 35–51, 2012.
- [9] M. McEwan, J. R. Wright, J. E. Cooper, and A. Y. T. Leung, “A combined modal/finite element analysis technique for the dynamic response of a non-linear beam to harmonic excitation,” *Journal of Sound and Vibration*, vol. 243, no. 4, pp. 601–624, 2001.
- [10] S. H. Strogatz, *Nonlinear Dynamics and Chaos*. Perseus Books, 1994.
- [11] A. H. Nayfeh and D. T. Mook, *Nonlinear Oscillations*. Weinheim: Wiley, 2 ed., 2004.
- [12] C. Touzé, O. Thomas, and A. Chaigne, “Asymmetric non-linear forced vibrations of free-edge circular plates. part 1: Theory,” *Journal of Sound and Vibration*, vol. 258, no. 4, pp. 649–676, 2002.
- [13] M. Peeters, R. Vigié, G. Sérandour, G. Kerschen, and J.-C. Golinval, “Nonlinear normal modes, part ii: Toward a practical computation using numerical continuation techniques,” *Mechanical systems and signal processing*, vol. 23, no. 1, pp. 195–216, 2009.
- [14] G. Kerschen, M. Peeters, J.-C. Golinval, and A. F. Vakakis, “Nonlinear normal modes, part i: A useful framework for the structural dynamicist,” *Mechanical Systems and Signal Processing*, vol. 23, no. 1, pp. 170–194, 2009.
- [15] L. Jezequel and C.-H. Lamarque, “Analysis of non-linear dynamical systems by the normal form theory,” *Journal of sound and vibration*, vol. 149, no. 3, pp. 429–459, 1991.

- [16] G. Genta, *Dynamics of rotating systems*. Springer Science & Business Media, 2007.
- [17] C.-W. Lee, D.-J. Han, J.-H. Suh, and S.-W. Hong, “Modal analysis of periodically time-varying linear rotor systems,” *Journal of Sound and Vibration*, vol. 303, no. 3-5, pp. 553–574, 2007.
- [18] M. Allen and J. H. Ginsberg, “Floquet modal analysis to detect cracks in a rotating shaft on anisotropic supports,” *24th International Modal Analysis Conference (IMAC XXIV)*, 2006.
- [19] P. Varney and I. Green, “Comparing the floquet stability of open and breathing fatigue cracks in an overhung rotordynamic system,” *Journal of Sound and Vibration*, vol. 408, pp. 314–330, July 2017.
- [20] A. Lazarus and O. Thomas, “A harmonic-based method for computing the stability of periodic solutions of dynamical systems,” *Comptes Rendus Mécanique*, vol. 338, pp. 510–517, september 2010.
- [21] O. Thomas, A. Lazarus, and C. Touzé, “A harmonic-based method for computing the stability of periodic oscillations of non-linear structural systems,” in *ASME 2010 International Design Engineering Technical Conferences and Computers and Information in Engineering Conference*, pp. 883–892, American Society of Mechanical Engineers, 2010.
- [22] S. Karkar, B. Cochelin, and C. Vergez, “A comparative study of the harmonic balance method and the orthogonal collocation method on stiff nonlinear systems,” *Journal of Sound and Vibration*, vol. 333, no. 12, pp. 2554–2567, 2014.
- [23] G. Von Groll and D. Ewins, “The harmonic balance method with arc-length continuation in rotor/stator contact problems,” *Journal of sound and vibration*, vol. 241, no. 2, pp. 223–233, 2001.
- [24] V. V. Bolotin, *The Dynamic Stability of Elastic Systems part 1*, vol. 1. 1964.
- [25] D. J. Acheson and T. Mullin, “Upside-down pendulums,” *Nature*, vol. 366, pp. 215–216, 11 1993.
- [26] J. S. Jensen, “Non-linear dynamics of the follower-loaded double pendulum with added support-excitation,” *Journal of sound and vibration*, vol. 215, no. 1, pp. 125–142, 1998.
- [27] K. Takahashi, “Dynamic stability of cables subjected to an axial periodic load,” *Journal of Sound and Vibration*, vol. 144, no. 2, pp. 323–330, 1991.
- [28] F. Dohnal, “Damping by parametric stiffness excitation: Resonance and anti-resonance,” *Journal of Vibration and Control*, vol. 14, no. 5, pp. 669–688, 2008.
- [29] J. C. Sartorelli and W. Lacarbonara, “Parametric resonances in a base-excited double pendulum,” *Nonlinear Dynamics*, vol. 69, no. 4, pp. 1679–1692, 2012.
- [30] F. Dohnal, “Experimental studies on damping by parametric excitation using electromagnets,” *Proceedings of the Institution of Mechanical Engineers, Part C: Journal of Mechanical Engineering Science*, vol. 226, pp. 2015–2027, August 2012.

- [31] L. Pešek, P. Šulc, V. Bula, and J. Cibulka, “Parametric “anti-resonance” phenomenon as active damping tool of beam flexural vibration,” *Procedia Engineering*, vol. 144, pp. 1031–1038, 2016.
- [32] O. Thomas, F. Mathieu, W. Mansfield, C. Huang, S. Trolier-McKinstry, and L. Nicu, “Efficient parametric amplification in micro-resonators with integrated piezoelectric actuation and sensing capabilities,” *Applied Physics Letters*, vol. 102, no. 16, p. 163504, 2013.
- [33] I. Mahboob and H. Yamaguchi, “Piezoelectrically pumped parametric amplification and q enhancement in an electromechanical oscillator,” *Applied Physics Letters*, vol. 92, no. 17, p. 173109, 2008.
- [34] G. Floquet, “Sur les equations differentielles lineaires,” *Ann. ENS [2]*, vol. 12, pp. 47–88, 1883.
- [35] E. T. Whittaker and G. N. Watson, *A course of modern analysis*. Cambridge university press, 1996.
- [36] J. Guckenheimer and P. Holmes, *Nonlinear oscillations, dynamical systems, and bifurcations of vector fields*, vol. 42. Springer Science & Business Media, 2013.
- [37] R. Seydel, “New methods for calculating the stability of periodic solutions,” *Computers and mathematics with applications*, vol. 14, pp. 505–510, April 1987.
- [38] X. Wang and J. K. Hale, “On monodromy computation,” *Computer Methods in Applied Mechanics and Engineering*, vol. 190, pp. 2263–2275, January 2001.
- [39] R. A. Calico and W. E. Wiesel, “Control of time-periodic systems,” *Journal of Guidance, Control, and Dynamics*, vol. 7, no. 6, pp. 671–676, 1984.
- [40] S. Sinha and D.-H. Wu, “An efficient computational scheme for the analysis of periodic systems,” *Journal of Sound and Vibration*, vol. 151, no. 1, pp. 91–117, 1991.
- [41] S. Sinha, R. Pandiyan, and J. Bibb, “Liapunov-floquet transformation: Computation and applications to periodic systems,” *Journal of Vibration and Acoustics*, vol. 118, no. 2, pp. 209–219, 1996.
- [42] E. A. Butcher and S. Sinha, “Normal forms and the structure of resonance sets in nonlinear time-periodic systems,” *Nonlinear Dynamics*, vol. 23, no. 1, pp. 35–55, 2000.
- [43] R. Pandiyan and S. Sinha, “Analysis of time-periodic nonlinear dynamical systems undergoing bifurcations,” *Nonlinear Dynamics*, vol. 8, no. 1, pp. 21–43, 1995.
- [44] S. Sinha, E. Butcher, and A. Dávid, “Construction of dynamically equivalent time-invariant forms for time-periodic systems,” *Nonlinear Dynamics*, vol. 16, no. 3, pp. 203–221, 1998.
- [45] P. L. Kapitza, “Dynamic stability of a pendulum with an oscillating point of suspension,” *Journal of Experimental and Theoretical Physics*, vol. 21, no. 5, pp. 588–597, 1951.

- [46] J. J. Thomsen, *Vibrations and stability: advanced theory, analysis, and tools*. Springer Science & Business Media, 2013.
- [47] R. H. Rand and D. Armbruster, *Perturbation methods, bifurcation theory and computer algebra*, vol. 65. Springer Science & Business Media, 2012.
- [48] A. Fidlin, *Nonlinear Oscillations in Mechanical Engineering*. Industriestr. 3, 77815 Bühl, Germany: Springer, 2006.
- [49] G. W. Hill, “On the part of the motion of the lunar perigee which is a function of the mean motions of the sun and moon,” *Acta mathematica*, vol. 8, no. 1, pp. 1–36, 1886.
- [50] C. Curtis and B. Deconinck, “On the convergence of hill’s method,” *Mathematics of computation*, vol. 79, no. 269, pp. 169–187, 2010.
- [51] L. Peletan, S. Baguet, M. Torkhani, and G. Jacquet-Richardet, “A comparison of stability computational methods for periodic solution of nonlinear problems with application to rotordynamics,” pp. 671–682, January 2013.
- [52] H. Poincaré, “Sur les déterminants d’ordre infini,” *Bull. Soc. Math. France*, vol. 14, no. 1886, pp. 77–90, 1886.
- [53] K. Kumar and L. S. Tuckerman, “Parametric instability of the interface between two fluids,” *Journal of Fluid Mechanics*, vol. 279, pp. 49–68, 1994.
- [54] B. Deconinck and J. N. Kutz, “Computing spectra of linear operators using the floquet–fourier–hill method,” *Journal of Computational Physics*, vol. 219, no. 1, pp. 296–321, 2006.
- [55] J. Liu and K. Bertoldi, “Bloch wave approach for the analysis of sequential bifurcations in bilayer structures,” *Proc. R. Soc. A*, vol. 471, no. 2182, 2015.
- [56] T. Detroux, L. Renson, L. Masset, and G. Kerschen, “The harmonic balance method for bifurcation analysis of large-scale nonlinear mechanical systems,” *Computer Methods in Applied Mechanics and Engineering*, vol. 296, pp. 18–38, 2015.
- [57] G. Moore, “Floquet theory as a computational tool,” *SIAM journal on numerical analysis*, vol. 42, no. 6, pp. 2522–2568, 2005.
- [58] J. Zhou, T. Hagiwara, and M. Araki, “Spectral characteristics and eigenvalues computation of the harmonic state operators in continuous-time periodic systems,” *Systems and Control Letters*, vol. 53, pp. 141–155, March 2004.
- [59] A. Lazarus, B. Prabel, and D. Combescure, “A 3d finite element model for the vibration analysis of asymmetric rotating machines,” *Journal of Sound and Vibration*, vol. 329, no. 18, pp. 3780–3797, 2010.
- [60] F. Bekhoucha, S. Rechak, L. Duigou, and J.-M. Cadou, “Nonlinear forced vibrations of rotating anisotropic beams,” *Nonlinear Dynamics*, vol. 74, no. 4, pp. 1281–1296, 2013.

- [61] M. Monteil, C. Touzé, O. Thomas, and S. Benacchio, “Nonlinear forced vibrations of thin structures with tuned eigenfrequencies: the cases of 1: 2: 4 and 1: 2: 2 internal resonances,” *Nonlinear Dynamics*, vol. 75, no. 1-2, pp. 175–200, 2014.
- [62] B. Bentvelsen and A. Lazarus, “Modal and stability analysis of structures in periodic elastic states: application to the ziegler column,” *Nonlinear Dynamics*, vol. 91, no. 2, pp. 1349–1370, 2018.
- [63] M. S. Allen, M. W. Sracic, S. Chauhan, and M. H. Hansen, “Output-only modal analysis of linear time-periodic systems with application to wind turbine simulation data,” *Mechanical Systems and Signal Processing*, vol. 25, pp. 1174–1191, 2011.
- [64] W. N. France, M. Levadou, T. W. Treacle, J. R. Paulling, R. K. Michel, and C. Moore, “An investigation of head-sea parametric rolling and its influence on container lashing systems,” *Marine Technology*, vol. 40, no. 1, pp. 1–19, 2003.
- [65] A. Sharma and S. C. Sinha, “An approximate analysis of quasi-periodic systems via floquet theory,” *Journal of Computational and Nonlinear Dynamics*, vol. 13, no. 2, p. 021008, 2018.
- [66] H. Bohr, *Almost periodic functions*. Courier Dover Publications, 2018.
- [67] H. Poincaré, “Mémoire sur les courbes définies par une équation différentielle (i),” *Journal de mathématiques pures et appliquées*, vol. 7, pp. 375–422, 1881.
- [68] S. Sinha, S. Redkara, and E. A. Butcher, “Order reduction of nonlinear systems with time periodic coefficients using invariant manifolds,” *Journal of Sound and Vibration*, vol. 284, no. 1, pp. 985–1002, 2005.
- [69] M. Tommasini, O. N. Krillov, D. Misseroni, and D. Bigoni, “The destabilizing effect of external damping: Singular flutter boundary for the pflüger column with vanishing external dissipation,” *Journal of the Mechanics and Physics of Solids*, vol. 91, pp. 204–215, June 2016.
- [70] F. Dercole and S. Rinaldi, *Dynamical systems and their bifurcations*, pp. 291–325. IEEE-Wiley Press, 2011.
- [71] A. Logg, K.-A. Mardal, and G. Wells, *Automated solution of differential equations by the finite element method: The FEniCS book*, vol. 84. Springer Science & Business Media, 2012.
- [72] A. Böttcher and B. Silbermann, *Analysis of Toeplitz operators*. Springer Science & Business Media, 2013.
- [73] J. Killingbeck, “On the hill determinant method,” *Journal Physics A: Mathematics general*, pp. 2903–1906, January 1986.
- [74] J. D. Joannopoulos, S. G. Johnson, J. N. Winn, and R. D. Meade, *Photonic crystals: molding the flow of light*. Princeton university press, 2011.
- [75] E. De Langre, “Frequency lock-in is caused by coupled-mode flutter,” *Journal of fluids and structures*, vol. 22, no. 6-7, pp. 783–791, 2006.

- 
- [76] E. Jones, T. Oliphant, P. Peterson, *et al.*, “SciPy: Open source scientific tools for Python,” 2001. [accessed 20 April 2018].
- [77] V. Hernandez, J. E. Roman, and V. Vidal, “Slepc: A scalable and flexible toolkit for the solution of eigenvalue problems,” *ACM Transactions on Mathematical Software (TOMS)*, vol. 31, no. 3, pp. 351–362, 2005.
- [78] S. S. Rao and F. F. Yap, *Mechanical vibrations*, vol. 4. Prentice Hall Upper Saddle River, 2011.
- [79] P. Friedmann, C. Hammond, and T.-H. Woo, “Efficient numerical treatment of periodic systems with application to stability problems,” *International Journal for Numerical Methods in Engineering*, vol. 11, no. 7, pp. 1117 – 1136, 1977.
- [80] B. Deconinck and J. N. Kutz, “Computing spectra of linear operators using the floquet–fourier–hill method,” *Journal of Computational Physics*, vol. 219, no. 1, pp. 296–321, 2006.
- [81] J. M. McCarthy, S. Watkins, A. Deivasigamani, and S. J. John, “Fluttering energy harvesters in the wind: A review,” *Journal of Sound and Vibration*, vol. 361, pp. 355–377, 2016.
- [82] A. V. Knyazev and K. Neymeyr, “A geometric theory for preconditioned inverse iteration iii: A short and sharp convergence estimate for generalized eigenvalue problems,” *Linear Algebra and its Applications*, vol. 358, no. 1-3, pp. 95 – 114, 2003.

